Aus der

Neurologischen Universitätsklinik Tübingen
Abteilung Neurologie mit Schwerpunkt
neurovaskuläre Erkrankungen

Probing functional connectivity of cerebellar cortex with cerebral cortex utilizing TMS-EEG

Inaugural-Dissertation
zur Erlangung des Doktorgrades
der Medizin

der Medizinischen Fakultät
der Eberhard-Karls-Universität
zu Tübingen

vorgelegt von

Gaßmann, Lukas

2024

Dekan: Professor Dr. B. Pichler

1. Berichterstatter: Professor Dr. U. Ziemann
2. Berichterstatter: Professor Dr. M. Giese

Tag der Disputation: 21.10.2024

Allen, deren Wort zählt.

Table of contents

I. List of figures

II. List of tables

III. Abbreviations

CBI *cerebellar brain inhibition*

cb-N45 *cerebellar N45*

cb-P25 *cerebellar P25*

cbTMS *cerebellar transcranial magnetic stimulation*

DTC *dentato-thalamo-cortical tract*

DTI *diffusion tensor imaging*

EMG *electromyography*

ES *electrical stimulation*

FDI *first dorsal interosseus*

GMFP *Global Mean Field Potential*

ICA *independent component analysis*

MEP *motor evoked potential*

MNI *Montreal Neurological Institute and Hospital*

MRI *magnetic resonance imaging*

MSO *maximum stimulator output*

PCA *posterior cerebral artery*

RMT *resting motor threshold*

SARA *Scale for the Assessment and Rating of Ataxia*

SD *standard deviation*

SEM *standard error of the mean*

SEP *somatosensory-evoked potential*

TEPs *TMS-evoked potentials*

TFR *time-frequency response*

TMS *transcranial magnetic stimulation*

1 Introduction

1.1 Relevance

The cerebellum is a complex structure. While its involvement in coordination and motor performance are prime examples of its substantial relevance for proper functioning, it has also been observed to be involved in cognitive performance (D'Angelo, 2018).

Adequate motor performance depends on proper functioning of the cerebellum. Consequently, disorders affecting the cerebellum severely affect motor performance, leading to deficits including tremor and ataxia. Moreover, the cerebellum has been observed to be involved in several cognitive functions, including language, working memory and visuo-spatial orientation (Schmahmann, 2019). Indeed, cerebellar disorders ranging from neurodegenerative disorders to cerebellar stroke are accompanied by motor disturbances as well as cognitive deficits and personality changes (Schmahmann, 2019). Moreover, several neuropsychiatric disorders are associated with cerebellar dysfunction, further providing evidence for the implication of the cerebellum in proper cognitive functioning (Parker et al., 2014). The influence of the cerebellum over complex behavior, both motor and cognitive, is most likely the product of its extensive connectivity with cerebral cortex, as evidenced by neuroimaging studies (Dum and Strick, 2003, Stoodley and Schmahmann, 2010). Directly probing these connections in healthy volunteers can contribute to increasing our understanding of cerebellar physiology and consequently, its disorders.

Attempts have been made to probe the functional connectivity of the cerebellar cortex by delivering transcranial magnetic stimulation (TMS) to the primary motor cortex. Utilizing an electromyographic output of small hand muscles, a significant reduction in amplitude was observed when delivering TMS to the cerebellar cortex 5-7 ms before activating the hand area of the primary motor cortex – a phenomenon termed cerebellar brain inhibition (CBI) (Ugawa et al., 1995). Over the years, more sophisticated attempts have been made, with minor variations in the site of stimulation, TMS protocol, and TMS intensity (Fernandez et al., 2018).

Recently, feasibility studies were conducted to investigate an EEG output after delivering TMS directly to the cerebellar cortex, to directly probe the functional connectivity between cerebellar cortex and cerebral cortex (Fernandez et al., 2021). The advantage of an EEG output versus an electromyographic output is clear: with EEG, the whole cortical surface of the cerebrum can be topographically investigated. Moreover, the direct effects on the cerebral cortex elicited by cerebellar TMS (cbTMS) may be observed, while electromyography (EMG) of small hand muscles is limited to an indirect output through a specific part of the motor cortex as an indication of cerebellar modulation of the muscular response. Nonetheless, several challenges when delivering cbTMS-EEG have so far precluded the identification of EEG markers of cerebellar activation in the cerebral cortex. Firstly, the lack of an adequate somatosensory control condition to account for a possible overlapping in time of cbTMS-evoked EEG responses with somatosensory-evoked responses. Secondly, a control condition to account for the possible concomitant activation of the closely located occipital cortex, which may confound observed EEG responses. Thirdly, whether the direction of the induced current in the cerebellar cortex influences EEG responses.

In this exploratory work, it was aimed at identifying EEG responses specifically evoked by cerebellar activation via TMS, while accounting for the aforementioned challenges.

1.2 Cerebellar connectivity with cerebral cortex

An initial demonstration of the intimate connection between the cerebellar cortex and the contralateral cerebral cortex was crossing cerebellar diaschisis, which is characterized by a decrease in blood flow and metabolism in the cerebellar hemisphere contralateral to a cerebral lesion (D'Angelo and Casali, 2012).

Neuroanatomical observations showed connectivity between neo-cerebellar regions and the contralateral cerebral cortex, mediated by a tract traversing the dentate nucleus, the superior cerebellar peduncle, the red nucleus, and thalamic nuclei – namely, the dentato-thalamo-cortical tract (DTC) (Figure 1) (Palesi et al., 2015).

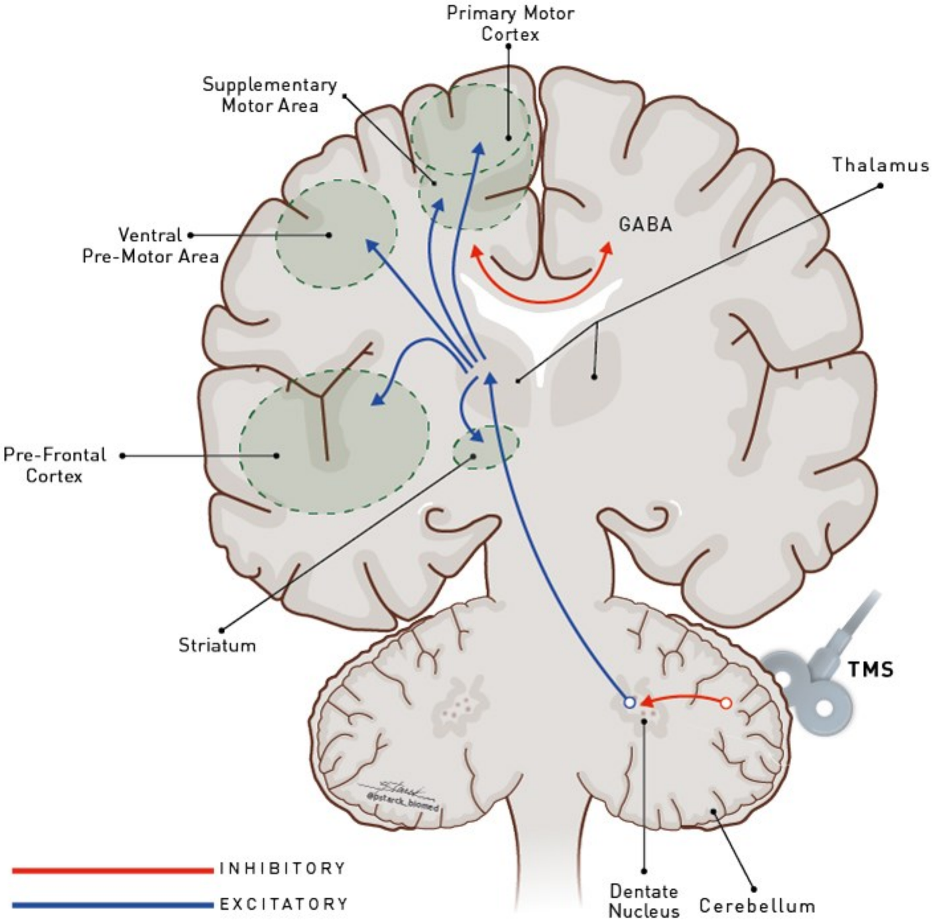

Figure 1: Schematic representation of cerebellar cortical and subcortical connections

Network model showing cerebellar connections to the contralateral cerebral cortex. Each arrow schematically represents one neuron. The dentate nucleus receives inhibitory input from Purkinje cells and modulates other brain areas, including the contralateral primary motor cortex through the dentato-thalamo-cortical tract (DTC). TMS: transcranial magnetic stimulation. GABA: gamma-aminobutyric acid. Inhibitory connections are represented by red, excitatory connections by blue arrows. **Source:** original from (Franca et al., 2020), the taken adapted version from (Cury et al., 2020), legend modified.

These pathways have since been investigated utilizing several methods. Using advanced diffusion magnetic resonance imaging (MRI) tractography, pathways which connect the cerebellum with contralateral cerebral cortex were modelled *in vivo* in volunteers (Palesi et al., 2015). About 80% of the reconstructed DTC connected corresponding areas of the cerebral and cerebellar cortex, and reconstructed streamlines predominantly passed through the superior cerebellar peduncle and the ventrolateral thalamus, connecting the cerebellar cortex of each side with contralateral associative areas of the cerebral cortex (Palesi et al., 2015). The cerebello-cerebral loops are highly segregated and form complex interconnections. Studies applying high-resolution tractography have found pronounced connectivity between the cerebellar cortex and associative areas of the cerebral cortex, especially with prefrontal and temporal areas, accounting for over 80% of afferent or efferent fiber tracts to the cerebellar cortex (Figure 2) (Palesi et al., 2015, Palesi et al., 2017).

Furthermore, neurotropic viruses were administered to non-human primates, to observe the transneuronal transport of these viruses to investigate the topographic organization of pathways connecting the cerebellar cortex with the dorsolateral prefrontal cortex and the primary motor cortex (Kelly and Strick, 2003). Through this method, when applied to cerebello-thalamo-cortical pathways, it was observed that the primary motor cortex was connected with Purkinje cells of the cerebellar cortex, mostly located in lobules IV-VI (Kelly and Strick, 2003). When applied to Brodmann area 46, it was observed that this area is predominantly connected with Purkinje cells in Crus II of the ansiform lobule (Kelly and Strick, 2003). Thus, both the primary motor cortex and area 46 were observed to be connected with the cerebellar cortex (Kelly and Strick, 2003).

In conclusion, the lateral regions of each cerebellar hemisphere constitute the cerebro-cerebellum, which shows predominant connectivity with the contralateral cerebral cortex (D'Angelo, 2018). Most efferent projections of the cerebellum pass through the dentate nucleus and the ventrolateral thalamic nuclei to the cerebral cortex (D'Angelo and Casali, 2012). The most predominant efferent projections are parietal and prefrontal loops (D'Angelo and Casali, 2012).

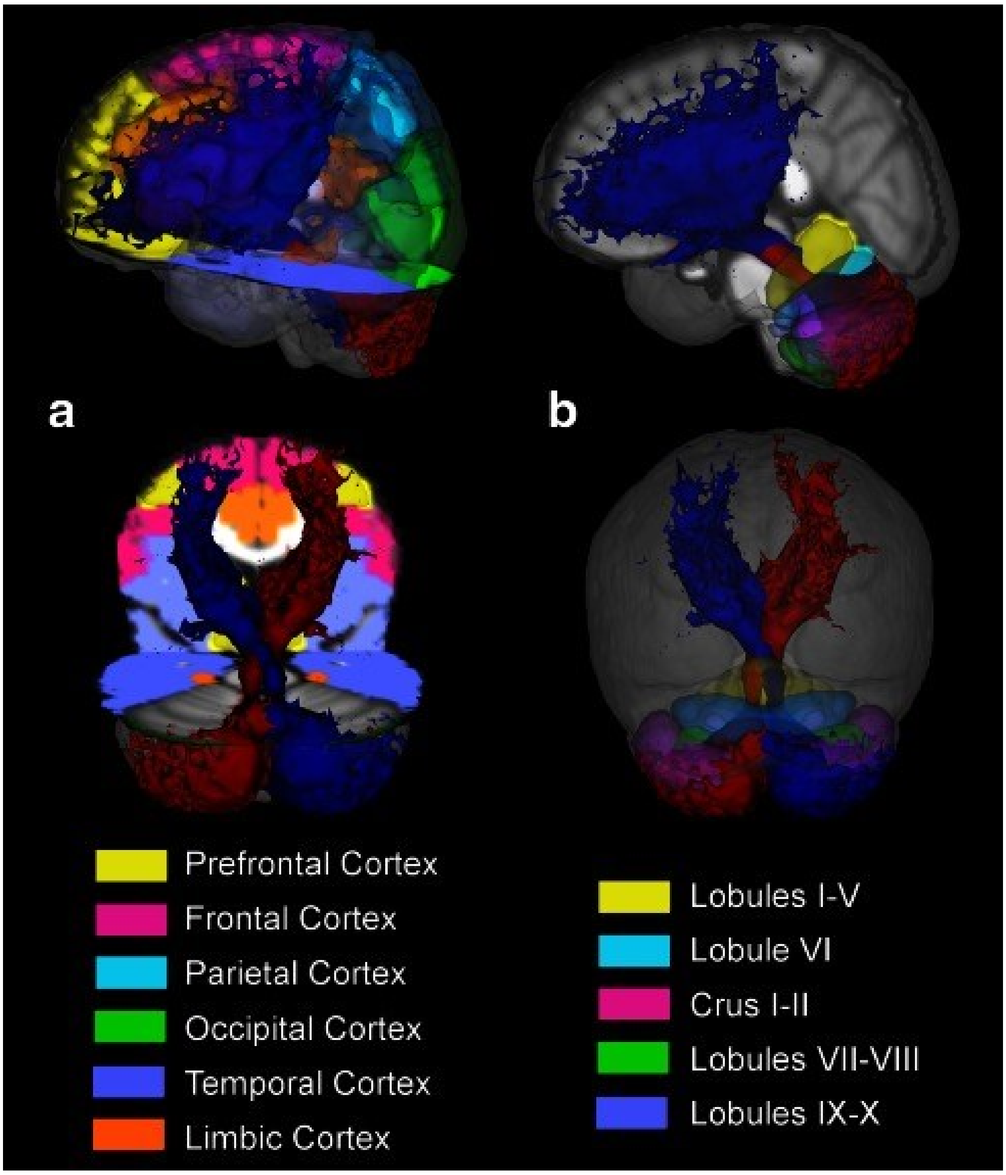

Figure 2: Reconstruction of the connectivity between cerebellar cortex and cerebral cortex utilizing high-resolution tractography

Depicted is a tridimensional view of the average cerebello-thalamo-cortical pathway across subjects (n=15) in Montreal Neurological Institute (MNI) space, which is a common brain atlas. Cerebral **(a)** and cerebellar **(b)** atlases are overlaid to assist visualization of cerebellar connections. **a** Distribution of left (red) and right (blue) tracts in the cerebral cortex: the reconstructed tracts reach the prefrontal (yellow), frontal (fuchsia) and temporal (violet) cortices with greater density of streamlines. **b** Streamlines distribution in the cerebellar cortex: the lateral Crus I–II (fuchsia) and the lateral lobules VIIb/VIII (green) are showing the greatest density of tracts. **Source:** taken from (Palesi et al., 2015), figure and legend modified.

1.3 Cerebellar brain inhibition

The first study to probe cerebellar function with TMS applied a double-coil TMS-EMG procedure, observing a significant reduction in motor evoked potential (MEP) amplitude when delivering TMS to the cerebellar cortex in a specific time-window (5-7 ms) before delivering TMS to the primary motor cortex – a phenomenon termed CBI (Figure 3) (Ugawa et al., 1995).

MEPs were derived from the first dorsal interosseus (FDI) muscle contralateral to the primary motor cortex being stimulated. CbTMS was applied to the cerebellar hemisphere contralateral to the primary motor cortex, as the efferent connections of the cerebellum predominantly cross to the contralateral cerebral hemisphere through the DTC (see 1.2). Furthermore, the best site of stimulation to elicit CBI on the group level was investigated, showing a significant difference in or absence of CBI when delivering cbTMS to different sites of stimulation (Ugawa et al., 1995). Lastly, the effects of changing directionality of the electric field being applied by TMS were investigated - CBI was observed only when an upward induced current was applied to the cerebellar cortex, but CBI was absent when delivering TMS with a downward induced current (Ugawa et al., 1995).

Since then, CBI could be reproduced in a multitude of studies and was utilized to probe cerebellar connectivity to the cerebral cortex (Fernandez et al., 2018).

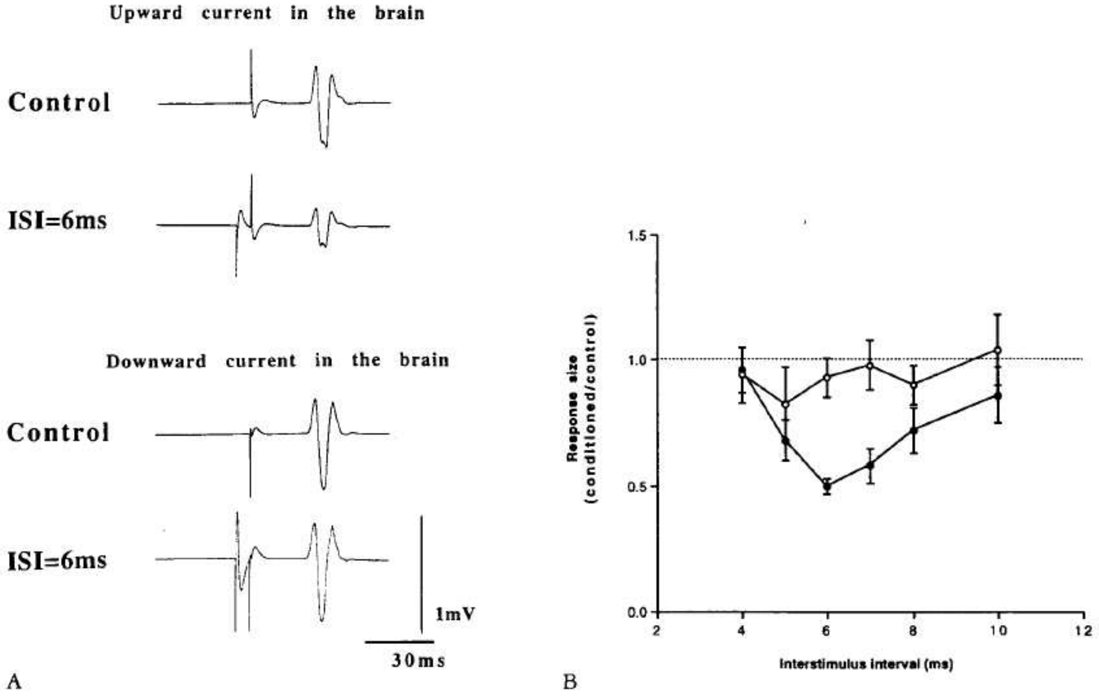

Figure 3: Cerebellar brain inhibition: phenomenon, current directionality, interstimulus interval

Depicted are the results of electromyography (EMG) of the right first dorsal interosseus (FDI) muscle. **A.** Depicts the motor evoked potentials (MEP) in the FDI elicited by transcranial magnetic stimulation (TMS). Shown are pairs of average EMG responses of one subject: control single-pulse TMS to the primary motor cortex (M1) and conditioned paired-pulse TMS to the cerebellar cortex followed by M1 (interstimulus interval (ISI) of 6 ms). The control TMS to M1 was set to produce a MEP amplitude of about 0.8 mV, and the TMS intensity of the conditioning cerebellar TMS (cbTMS) was set to -5%. Top row: When applying an upward induced current in the cerebellar cortex, the conditioning cbTMS reduced the size of the MEP response elicited by TMS to M1. Bottom row: When a downward induced current was applied, the conditioning cbTMS had no effect on the size of MEP elicited by TMS to M1. **B.** Comparison of the time course of suppression between upward (closed circles) and downward (open circles) induced current in the cerebellar cortex. Values are averages (± standard error) of 4 subjects. Significant suppression was seen at ISI of 5, 6, and 7 ms for the upward induced current ($p<0.05$ for 5 ms, $p<0.001$ for 6 ms, and $p<0.02$ for 7 ms), but there was no significant suppression for the downward induced current. The mean amount of suppression at intervals of 6 and 7 ms was larger when an upward rather than downward induced current was applied to the cerebellar cortex ($p<0.01$ for 6 ms, and $p<0.02$ for 7 ms). **Source:** taken from (Ugawa et al., 1995), legend modified.

1.4 TMS-evoked potentials in EEG

TMS elicits TMS-evoked potentials (TEPs) in EEG. A combination of TMS with EEG can serve the purpose of locating the neuronal activity evoked by TMS to evaluate connectivity patterns between different brain regions (Ilmoniemi et al., 1999), for example between cerebellar cortex and cerebral cortex.

The CBI protocol involving TMS-EMG has been utilized to probe cerebellar connectivity to the primary motor cortex by measuring a suppression of the MEP amplitude in hand muscles when cerebellar activation preceded TMS to primary motor cortex (Ugawa et al., 1995). Consequently, CBI is limited to an indirect measurement of the effects of cbTMS on primary motor cortex excitability. Furthermore, CBI relies on the measurement of the amplitude of MEPs and an observed difference in amplitude, however, the amplitude of MEPs is influenced depending on uncontrolled dynamic changes in excitability at the location and time of TMS, thus showing high variability (Schilberg et al., 2021, Rocchi et al., 2022).

In contrast, TMS in combination with EEG can enable the direct observation of cerebellar efferent connectivity. When delivering TMS to a cortical target, neuronal activation has been observed to spread to connected regions (Ilmoniemi et al., 1997). Moreover, TEPs in EEG have generally been observed to be well reproducible (Komssi et al., 2004, Lioumis et al., 2009). A TEP usually is a sequence of negative and positive peaks observed post-TMS, with a distinct latency and spatial distribution (Ilmoniemi et al., 1997). Per convention, peaks within the TEP are labelled by their amplitude and latency.

1.5 Somatosensory-evoked potentials

A somatosensory-evoked potential (SEP) is a brain response elicited by somatosensory stimuli. The delivery of TMS involves somatosensory stimuli to the scalp, from muscle movements and direct sensory-neuron stimulation (Ilmoniemi and Kicic, 2010).

When applying a sham stimulation that deliberately did not involve the induction of a current in the cortex, a negative deflection peaking at 100 ms post-TMS in fronto-central electrodes (N100) was observed (Gordon et al., 2021). Furthermore, unspecific EEG responses to multisensory input have consistently been observed to overlap in time with TEPs beyond 60-70 ms post-TMS (Gordon et al., 2021, Conde et al., 2019, Ahn and Frohlich, 2021, Biabani et al., 2019). The problem of overlapping sensory responses when stimulating the cerebellar cortex was specifically emphasized in a recent study on the feasibility of cbTMS-EEG (Fernandez et al., 2021). Consequently, when the goal is to identify EEG responses specifically evoked by cbTMS, an adequate control condition is necessary.

Notably, to this day the nature of the interaction between SEPs and TEPs remains open to active debate – they may merely overlap in time (Gordon et al., 2021, Conde et al., 2019, Ahn and Frohlich, 2021, Biabani et al., 2019) or influence one another in more complex ways (Rocchi et al., 2021). Hence, caution is advised when attributing EEG responses beyond 60-70 ms post-cbTMS specifically to cbTMS, even when a proper control condition was delivered, as the nature of the interaction between SEPs and TEPs has not yet been conclusively investigated.

Nonetheless, a thorough comparison between an adequate control condition delivering comparable multisensory input and a condition involving activation of the cerebellar cortex can provide valuable information to probe EEG responses to cbTMS even beyond 60-70 ms post TMS.

1.5.1 SHAM-MS procedure & saturation approach

To identify TEPs evoked by cbTMS, a control condition to account for a possible overlap in time between SEPs and TEPs was necessary (see 1.5). Since cbTMS involves muscle twitches and requires high TMS intensities (Fernandez et al., 2021), it was aimed at developing a control condition specifically suited for the challenges imposed by cbTMS. This approach was inspired by a recent paper, investigating a saturation approach of SEPs (Gordon et al., 2021).

Regarding the impact of multimodal EEG responses to sensory input in TMS-EEG measurements, at least two sources of sensory input have been consistently identified as present in typical measurements, namely auditory and somatosensory input. The impact of auditory inputs, which potentially generate auditory evoked potentials, can be properly addressed with masking noise (Massimini et al., 2005, Belardinelli et al., 2019, Rocchi et al., 2021), which was applied (see 2.1.3).

However, it was also necessary to consider the impact of somatosensory-evoked responses. While it has been established in the field to utilize masking noise to suppress auditory evoked potentials (Massimini et al., 2005, Belardinelli et al., 2019, Rocchi et al., 2021), there is evidence indicating that somatosensory inputs from TMS are another source of sensory-evoked responses, which are independent from auditory evoked potentials: Ter Braak et al. demonstrated the presence of SEPs when performing TMS-EEG in a completely deaf subject, which could be attributed to TMS-associated somatosensory input (ter Braack et al., 2015). Conde et al., when applying state-of-the-art masking noise in their TMS-EEG experiment, have observed sensory evoked responses, which could be explained by TMS-associated somatosensory input (Conde et al., 2019). Likewise, Gordon et al. observed sensory-evoked responses while using masking noise considerably suppressing TMS-associated auditory input (Gordon et al., 2021). Ross et al. applied an optimized control for auditory input in a TMS-EEG experiment, which included masking noise, but still found a sensory response in the EEG, which the authors identified as SEP (Ross et al., 2022).

In light of these considerations and in contrast to previous sham procedures applied when delivering cbTMS, a combination of electrical stimulation (ES) to the neck and MS over the ipsilateral trapezius muscle in the sham condition was applied to deliver a multisensory input comparable to cbTMS. This was termed the SHAM-MS condition (Gassmann et al., 2022).

Conditions involving cbTMS were combined with ES to the skin on the neck and MS to the trapezius muscle with the same parameters as in the SHAM-MS – referred to as the REAL condition (Gassmann et al., 2022).

The idea was, that a subtraction of the EEG responses to SHAM-MS from REAL could enable to observe the EEG responses to cbTMS in a time-window otherwise overlapping in time with somatosensory-evoked EEG responses. As the N100 component was expected to reach a saturation in amplitude (Gordon et al., 2021) by the SHAM-MS condition, it was hypothesized that adding cbTMS in the REAL condition should not lead to a further increase in the amplitude of the already saturated N100 response. This was termed a saturation approach for cbTMS (Gassmann et al., 2022).

1.6 Concomitant stimulation of the occipital cortex

When delivering TMS to the cerebellar cortex, the generated electric field may reach the occipital cortex, as it lies in close anatomical proximity to the cerebellar target. This has been described as a possible confounding factor of EEG responses identified to be specifically elicited by cbTMS in recent feasibility studies applying cbTMS (Fernandez et al., 2021).

When Garcia et al. investigated EEG responses to TMS to the occipital cortex, a common oscillation with peaks at 40 ms, 200 ms, and 385 ms post-TMS in areas of left dorsolateral prefrontal, bilateral frontal and parietal cortex were observed (Figure 4) (Garcia et al., 2011). Since the efferent cerebellar-to-cerebral connectivity predominantly involves pre-frontal and parietal areas through the DTC (see 1.2), it is important to control for concomitant stimulation of the occipital cortex when a goal is the identification of cbTMS-specific EEG responses.

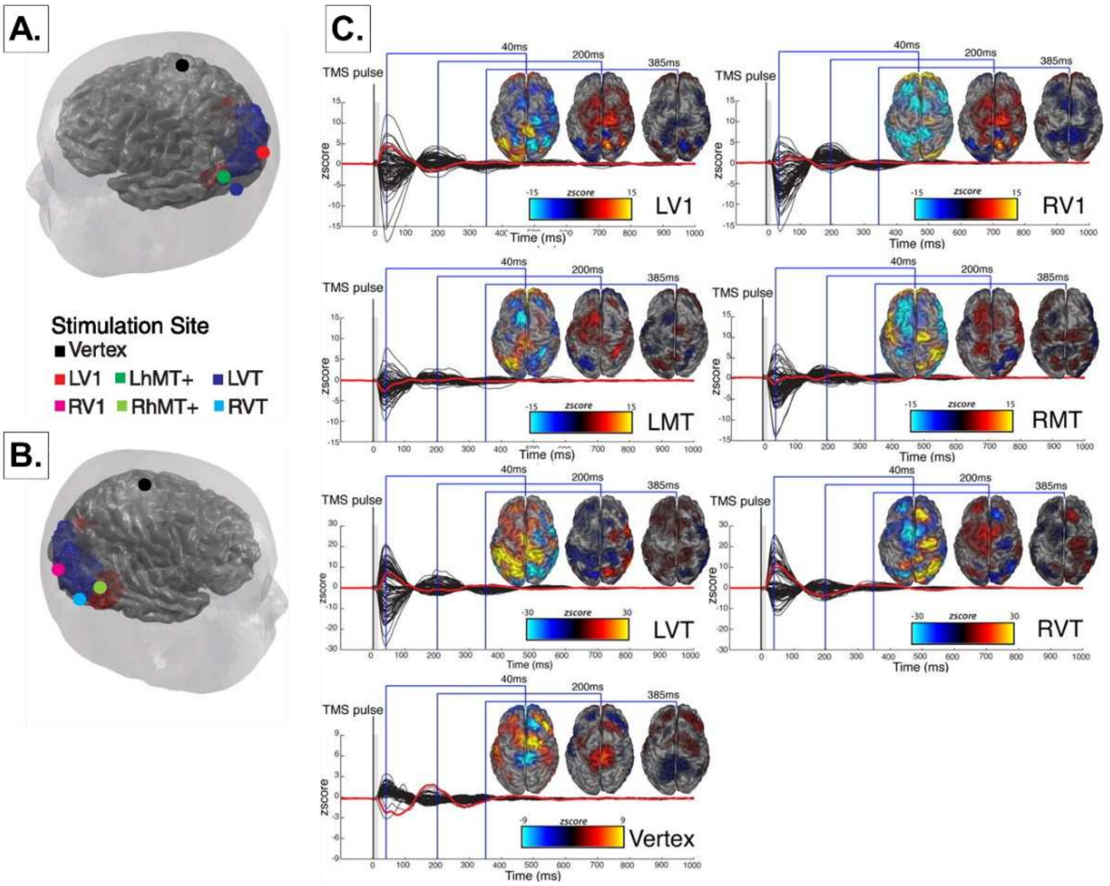

Figure 4: Peaks in the TMS-evoked EEG potential across stimulation sites on different parts of the occipital cortex

Depicts the response in electroencephalography (EEG) for different sites of transcranial magnetic stimulation (TMS) targeting the occipital cortex. **A.** and **B.** show the TMS sites as filled circles with a separate color for each TMS site. R: right. L: left. V1: primary visual areas. hMT+: motion-sensitive human middle temporal cortex. VT: ventral temporal region. **C.** Peaks in the TMS-evoked potential across stimulation site. Each butterfly plot is the TMS-evoked potential after *z*-score transformation and artefact editing. Gray rectangles represent the window of the autoregressive moving average correction, and red lines show the EEG response of the electrode closest to the stimulation site (LV1: electrode O1; RV1: electrode O2; LMT: electrode PO5; RMT: electrode PO6; LVT: electrode PPO9H; RVT: electrode PPO10H; vertex: electrode CZ). Inspection of the TMS-evoked potential across stimulation sites reveals a common oscillation with peaks at 40, 200, and 385 ms, with periodicity ~150-200 ms. Spatial patterns above the time-courses represent the magnitude distribution across the brain. Transparency of the colormap superimposed onto the brain calculated individually per brain map and scaled by percentile rank. Color bar below the spatial patterns. X-axis: time in ms. Y-axis: z-score. **Source:** taken from (Garcia et al., 2011), figures combined and legend modified.

1.7 Objectives and hypotheses

Several objectives and hypotheses to be experimentally tested were formulated. Additionally to gaining further insight into and improving methods and protocols for TMS-EEG, it was aimed at investigating cortical responses in EEG evoked specifically by cbTMS.

Hence, given the current knowledge about the cerebellum, the following hypotheses were drafted:

1. cbTMS will elicit specific EEG responses, which will not be explicable by somatosensory input or concomitant stimulation of the occipital cortex.
2. cbTMS-specific EEG responses will be a marker of an activation of the DTC as the predominant efferent cerebellar pathway to the cerebral cortex.
3. EEG responses specific to cbTMS will be altered when the DTC pathway is structurally impaired.

2 Material and Methods

2.1 Resting state

Parts of the following Methods have been published in an Original Research Article (Gassmann et al., 2022).

2.1.1 Participants

In total, 53 healthy volunteers participated in this study (Gassmann et al., 2022). The final dataset consisted of the data from 46 participants (Gassmann et al., 2022). A total of 7 datasets were excluded (Gassmann et al., 2022).

Before measurements, a questionnaire was used to screen volunteers for contraindications for TMS, taking into account the current safety criteria of the International Federation of Clinical Neurophysiology (Rossi et al., 2021). Exclusion criteria included having any psychiatric or neurological disease or current treatment with drugs that act on the central nervous system (Ziemann et al., 2015), working at night (Ly et al., 2016), pregnancy, or substance addiction (Kaarre et al., 2018, Gassmann et al., 2022). Daily caffeine intake of more than the caffeine content of one beverage was an exclusion criterion (Gassmann et al., 2022). This was decided since lower caffeine doses have been found not to influence cortical excitability (Orth et al., 2005), and due to the exploratory nature of the study. Furthermore, participants with a resting motor threshold (RMT) above 60 % maximum stimulator output (MSO) were excluded from participation, because of the higher vulnerability for artefacts (Ilmoniemi and Kicic, 2010) and because cbTMS intensity was determined on the basis of the RMT, with absolute increments of up to +40 %MSO (Gassmann et al., 2022).

In the following, the reasons for the exclusion of the 6 excluded datasets will be detailed. Due to discomfort of the cbTMS procedure, 3 participants had to be excluded (Gassmann et al., 2022). A further 2 participants were excluded because they showed a RMT >60% MSO (Gassmann et al., 2022). Another screened participant was excluded due to regular consumption of prohibited substances (Gassmann et al., 2022). Lastly, 1 dataset showing excessive, consistent noise in the EEG data had to be rejected from data analysis (Gassmann et al., 2022). Notably, only right-handed subjects with a laterality index >0.5 according to the Edinburgh Handedness Questionnaire (Oldfield, 1971) were included (Gassmann et al., 2022) to avoid varying functional network properties because of being left-handed (De Gennaro et al., 2004). Of the final dataset from 46 participants, 23 were derived from experiment #1 and 23 from experiment #2 (Gassmann et al., 2022). For experiment #1, 9 participants were males and 14 females (Gassmann et al., 2022). Their mean age ± 1 standard deviation (SD) was 24.0 ± 5.2 years (Gassmann et al., 2022). For experiment #2, 14 participants were females and 9 males, with a mean ± 1 SD age of 22.4 ± 2.3 years (Gassmann et al., 2022).

The study was approved by the local Ethics Review Committee of the Medical Faculty of the Eberhard Karls University Tübingen, Germany (364/2020/BO2) in concordance with the Declaration of Helsinki and current TMS safety guidelines of the International Federation of Clinical Neurophysiology (Rossi et al., 2021). All subjects gave their written informed consent prior to study participation.

2.1.2 Materials

Table 1 contains a list of the materials utilized to conduct the experiments.

Table 1: List of Materials

The table contains a list of the materials utilized to conduct the experiments. The first column contains the name of the respective material, the second column a short description of its purpose. The third column contains further details on the utilized material. **Source:** materials as listed in (Gassmann et al., 2022), visualized as a table.

Material	Short description	Detail
Two Magstim 200^2	TMS stimulators	Generate a monophasic current waveform. Manufactured by Magstim Company Ltd., UK.
One figure-of-eight branding iron TMS coil	For delivering cbTMS and occipital cortex TMS	50 mm external diameter. The branding iron design of the TMS coil involves a coated finish, therefore, a casing is

		not needed. This allows for a comparatively closer proximity between brain target and coil surface.
One figure-of-8 TMS coil	For delivering primary motor cortex and trapezius stimulation	90 mm external diameter. With a full casing.
Constant current stimulator DS7A	Application of electrical stimulation	Electrical stimulation was applied with a fixed current of 25 mA throughout all measurements, 200 V compliance voltage and pulse width of 200 µs. Manufactured by Digitimer Ltd, UK.
Two pairs of round electrodes (diameter 1 cm)	For delivering electrical stimulation.	Integrated in the EEG cap, which were placed 2 cm and 4 cm below the electrode Oz and 5 cm lateral from the midline towards either side, with electrodes of the same polarity on the same side. The polarity switched after each pulse.
Three TMS compatible Ag/AgCl sintered ring electrode caps	For recording the EEG signal.	64 channels. Arranged in the International 10-10 montage. Impedance was kept <5 kΩ at the interface between skin and EEG electrodes throughout experiments. One cap for 52 cm, one for 54 cm, one for 56 cm head circumference. Manufactured by EasyCap GmbH, Germany.
Bipolar EMG adhesive hydrogel electrodes	For recording of the EMG.	Recorded from the FDI muscle of the right hand in a bipolar belly-tendon montage. Manufactured by Kendall, Covidien.
One 24-bit 80-channel biosignal amplifier (Model: NeurOne Tesla with	Used for recording EEG and EMG.	Set to 5 kHz sampling rate, and 0.16 Hz–1.25 kHz bandpass filter. Manufactured by Bittium Biosignals Ltd., Finland.

Analog Real-time Out Option)		
One pair of standard issue earbuds	For application of the masking noise.	Connected to the experimental computer containing the audio file.
One reclining chair	For seating participants comfortably.	-
One experimental computer	For conducting measurements.	-
Two positioning arms for TMS coils.	Keeping TMS coils in place during measurements.	-

2.1.3 Masking noise procedure

Masking noise was applied throughout all measurements to suppress auditory evoked potentials (Massimini et al., 2005, Ilmoniemi and Kicic, 2010, Rocchi et al., 2021), which could interfere with the identification of specific EEG responses to cbTMS in certain time-windows. The applied masking noise was created with an identical spectral distribution as the TMS clicking sound associated with the delivery of a TMS pulse (Gassmann et al., 2022). This masking noise was applied through earbuds (Table 1) (Gassmann et al., 2022). The loudness of the masking noise was adjusted individually right before each measurement block to a level capable of either fully suppressing the clicking sound or being on the highest tolerable level, whichever was reached first (Ilmoniemi and Kicic, 2010, Massimini et al., 2005, Gassmann et al., 2022).

2.1.4 Experimental design

To identify EEG responses specifically evoked by cbTMS, a novel protocol was applied, involving novel control conditions. The measurements were conducted in two separate experiments (Gassmann et al., 2022). For each experiment, all measurements were conducted on the same day (Gassmann et al., 2022). Experiment #1 aimed at evaluating the efficacy of the SHAM-MS procedure and the principal viability of the procedure (Gassmann et al., 2022). To confirm and reproduce the results of experiment #1, a second experiment was conducted involving multiple control conditions and building on the experiences of experiment #1 (Gassmann et al., 2022).

In the following, the experimental design of the two experiments will be described. Figure 5 provides a schematic overview of the design of the conducted experiments.

For experiment #1, EEG and EMG were prepared and RMT assessed before measurements (see 2.1.5) (Gassmann et al., 2022). Then, to confirm that the cerebellar cortex was indeed activated by delivering cbTMS, CBI was tested (see 2.1.6.1) and the smallest individual TMS intensity capable of eliciting CBI was fixed as the cbTMS intensity for the remainder of the individual measurements (Gassmann et al., 2022). Then, the individual EEG response to SHAM-MS was tested by applying the SHAM-MS condition in five blocks of increasing MS intensity (see 2.1.8.1), and the smallest intensity achieving a plateau in the N100 response was fixed as the SHAM-MS intensity for the remainder of the individual measurement (Gassmann et al., 2022). Lastly, cbTMS was delivered with an upward induced current in the brain (see 2.1.9) (Gassmann et al., 2022).

For experiment #2, again, EEG and EMG were prepared and RMT assessed before measurements (see 2.1.5) (Gassmann et al., 2022). Then, to confirm that the cerebellar cortex was indeed activated by delivering cbTMS, CBI was tested (see 2.1.6.1) and the smallest individual TMS intensity capable of eliciting CBI was fixed as the cbTMS intensity for the remainder of the individual measurements (Gassmann et al., 2022). For the SHAM-MS intensity, a supra-threshold intensity determined in experiment #1 was applied to achieve a plateau in the N100 response (see 2.1.8.1) (Gassmann et al., 2022). Thereafter, the occipital control condition was administered, set to the same TMS intensity as cbTMS (see 2.1.8.2) (Gassmann et al., 2022). Afterwards, cbTMS with an upward induced current in the brain was applied (see 2.1.9) (Gassmann et al., 2022). Lastly, the coil orientation was rotated by 180 degrees, to deliver cbTMS with a downward induced current (see 2.1.8.3) (Gassmann et al., 2022).

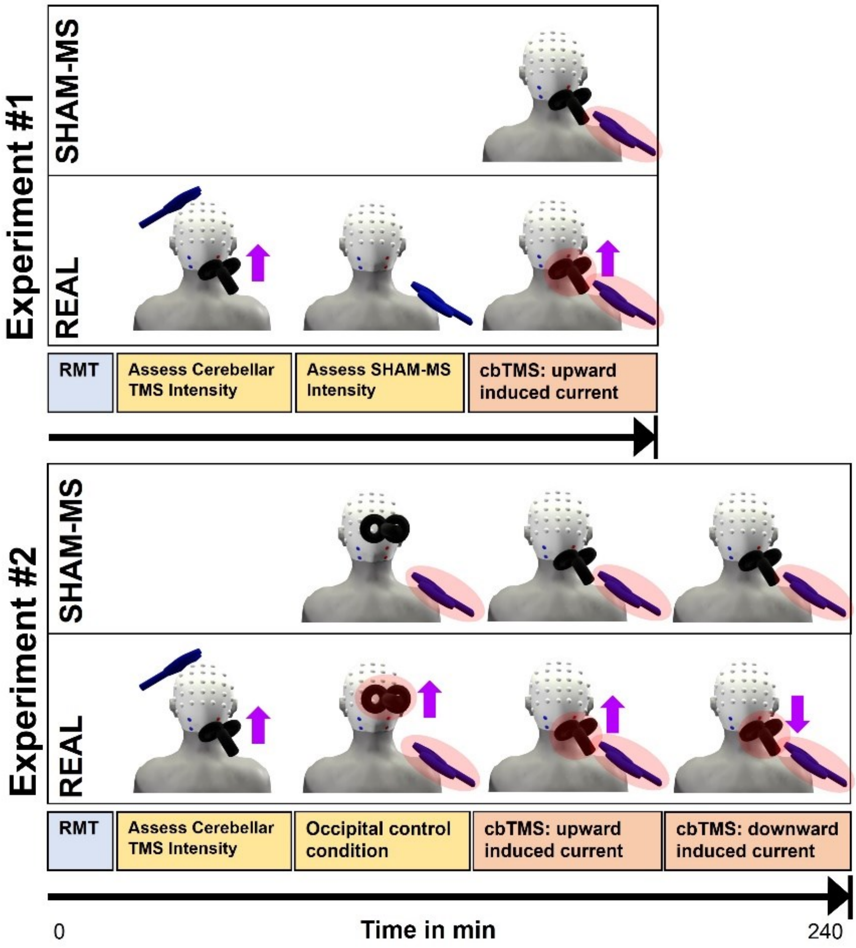

Figure 5: The measurement conditions involved in experiment #1 and experiment #2 of resting state

Depicts the experimental design of the experiments. The blue coil represents the positions of the 90 mm transcranial magnetic stimulation (TMS) coil, while the black coil represents the positions of the 50 mm branding iron TMS coil. Dots on the models' upper neck area represent the electric stimulation electrode positions, with blue and red electrodes each representing a polarity of the stimulation. The polarity switched after each pulse. The white cap schematically represents the electroencephalography (EEG) cap. Purple arrows represent the direction of the induced electric field in the tissue. RMT: resting motor threshold. cbTMS: cerebellar TMS. MS: magnetic stimulation. X-axis: time in minutes (min). **Top row:** The order of conditions for experiment #1, divided into SHAM-MS and REAL experimental conditions, which were delivered randomly intermixed. Pink highlights identify the coils that were used for stimulation in the respective condition, with identical positioning of the coils in REAL and SHAM-MS. **Bottom row:** The order of conditions for experiment #2, divided into SHAM-MS and REAL, with otherwise the same arrangements and conventions as in the top row. **Source:** taken from (Gassmann et al., 2022), legend modified.

2.1.5 Resting motor threshold assessment

In order to determine the motor cortical region corresponding to the right hand, RMT was individually assessed utilizing the relative frequency method (Rossini et al., 2015), while surface EMG of the right FDI was recorded (see 2.1.2) (Gassmann et al., 2022). Participants were comfortably seated in a reclining chair and instructed to relax and stay awake during the experiments (Gassmann et al., 2022).

Determination of the RMT was done by placing a figure-of-eight TMS coil (see 2.1.2) over the hand knob of the left primary motor cortex, oriented tangential to the head and with the coil handle backwards in an angle of 45° to the midline (Figure 6) (Rossini et al., 2015, Gassmann et al., 2022). TMS to this target evoked MEPs in the contralateral, right FDI measured via surface EMG (see 2.1.2) of these muscles (Figure 6) (Gassmann et al., 2022). The position was then individually optimized by determining the stimulation site eliciting the MEP with the largest amplitude in the channel FDI, and this site was marked on the disposable net cap (Rossini et al., 2015, Gassmann et al., 2022). Afterwards, starting at a level slightly above the MEP threshold, TMS intensity was decreased in steps of 1 %MSO (Rossini et al., 2015, Gassmann et al., 2022). The RMT was defined as the minimum intensity that was sufficiently producing a response of 50 µV in at least five out of ten subsequent trials (Rossini et al., 2015, Gassmann et al., 2022).

Following the RMT-assessment, the TMS intensity to elicit MEPs with an average of 0.8 ± 0.1 mV was determined to be used in CBI assessment (see 2.1.6.1) (Gassmann et al., 2022), as this intensity has been described to be preferential for CBI assessment (Fernandez et al., 2018). The intensity of the TMS was increased in steps of 1 %MSO to elicit, on an average of 10 trials, MEPs of 0.8 ± 0.1 mV in peak-to-peak amplitude (Groppa et al., 2012, Gassmann et al., 2022).

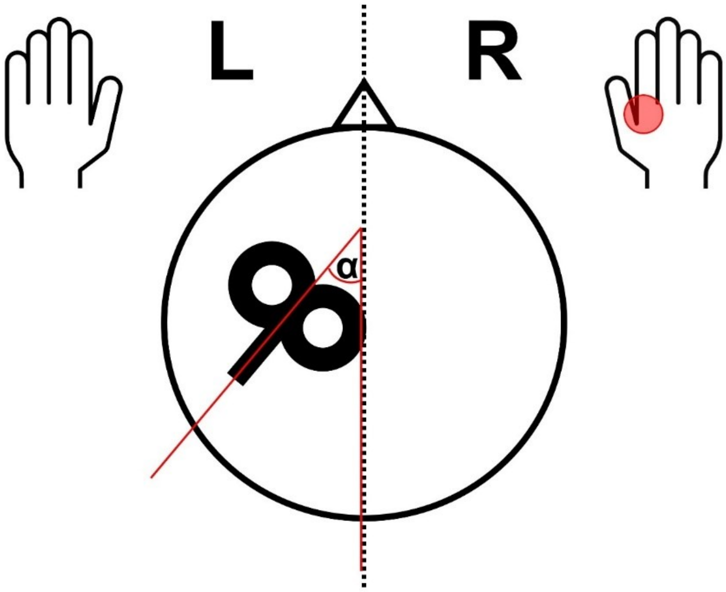

Figure 6: TMS coil positioning for motor cortex stimulation.

Schematic of a head, view from above. The figure-of-eight TMS coil was placed over the hand area of the left primary motor cortex. The black dotted line marks the midline. The red dot marks EMG electrode placement to record from the first dorsal interosseus muscle of the right hand. α=45° L=Left. R=Right.

2.1.6 Confirming cerebellar cortex stimulation

2.1.6.1 Cerebellar brain inhibition

To deliver cbTMS, a figure-of-eight coil was placed on the midpoint of the line between inion and the tip of the mastoid on the right side (Figure 5) (Gassmann et al., 2022), corresponding to the optimal site of stimulation on the group level as described in the literature (Fernandez et al., 2018, Ugawa et al., 1995, Gassmann et al., 2023b). The coil current was pointing downward, inducing an upward current in the brain (Gassmann et al., 2022). In an attempt to avoid concomitant stimulation of the occipital cortex, the coil was pointing upward towards the center of the brain (Gassmann et al., 2022). The handle was tilted 40° lateral from the midline (Gassmann et al., 2022). The figure-of-eight coil delivering TMS to the hand area of the left primary motor cortex was placed on the spot previously determined during RMT assessment to elicit the largest MEP and set to the previously determined TMS intensity eliciting MEPs with an amplitude of on average 0.8 ± 0.1mV (see 2.1.5) (Gassmann et al., 2022).

To elicit CBI, paired-pulse TMS was delivered with an interstimulus-interval of 6 ms, with the TMS pulse targeting the cerebellar cortex preceding single-pulse to the primary motor cortex (Ugawa et al., 1995, Gassmann et al., 2022). CBI was assessed in blocks of increasing cbTMS intensity (RMT+20%MSO, RMT+30%MSO, RMT+40%MSO), to determine the lowest cbTMS intensity that elicited an observable suppression of MEPs, defined as a CBI ratio ≤0.85 (Gassmann et al., 2022). In total, 80 TMS pulses were administered per subject (Gassmann et al., 2022). 40 paired-pulse TMS and 40 single-pulse TMS were delivered randomly intermixed (Gassmann et al., 2022).

CBI was calculated as a ratio utilizing the following calculation (Gassmann et al., 2022):

$$CBI = \frac{Mean\ MEP\ amplitude\ of\ paired - pulse\ TMS}{Mean\ MEP\ amplitude\ of\ single - pulse\ TMS\ to\ primary\ motor\ cortex}$$

2.1.6.2 Electric field simulation

The assessment of CBI served as an indirect and established marker of having reached the cerebellar cortex with TMS. To further provide evidence that this indeed was the case, offline electric field modelling was performed after all experiments were completed, utilizing the SimNIBS® environment (Thielscher et al., 2015), optimized for TMS (Weise et al., 2020, Gassmann et al., 2022).

To simulate the electric field induced over the cerebellar cortex by the specific TMS setup utilized, an official model of the TMS coil (see 2.1.2) utilized to deliver cbTMS in these experiments had to be created first. To assess the specific properties of the coil, a roentgenography of the coil was acquired to assess the coating thickness (Figure 7), while the other relevant parameters were acquired from the manufacturer. An official coil model was then created in cooperation with the SimNIBS® team on the basis of this data and utilized to perform this simulation.

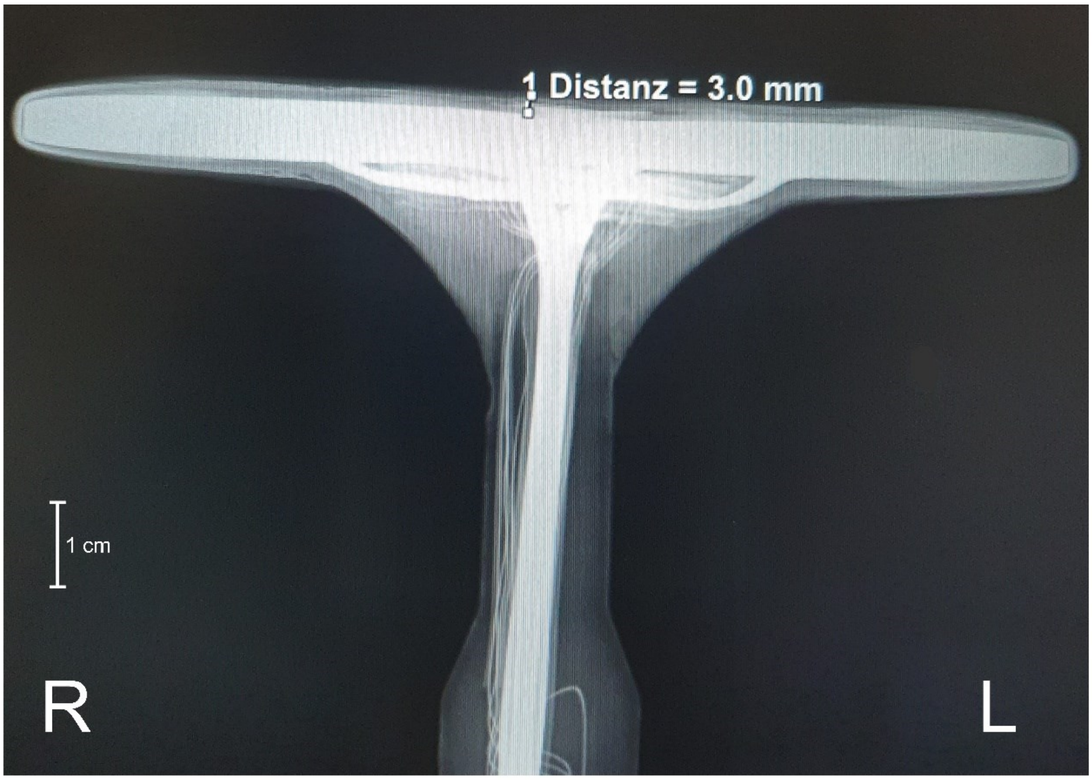

Figure 7: Roentgenography of the TMS coil utilized to deliver cbTMS

Radiography of the TMS coil utilized throughout the experiments to deliver cerebellar transcranial magnetic stimulation (cbTMS) was acquired to create an accurate official coil model in the SimNIBS® environment. With this coil model, a simulation of the generated electric field by cbTMS was performed. R: right. L: left. Calibration bar in the left bottom corner of the image. Distanz indicates a distance vector in millimeter (mm), which was applied to measure the thickness of the coil coating. Only the side view was performed since the other relevant parameters were known from the manufacturer.

However, not only the individual TMS setup had to be included for an accurate simulation of the electric field applied in these experiments, but also the target of TMS. To that end, individual anatomical T1-weighted MRIs were obtained from eight randomly selected participants (Gassmann et al., 2022). These were meshed and segmented utilizing the SimNIBS® headreco tool (Nielsen et al., 2018, Gassmann et al., 2022).

Currently, the minimal strength of an induced electric field over the cerebellar cortex capable of depolarizing neurons has not been conclusively investigated. As a possible solution to this challenge, the electric field induced over the primary motor cortex at RMT intensity was simulated for comparison (Gassmann et al., 2022), as it was known to be capable of eliciting MEPs, and thus, capable of depolarizing neurons. The coil model of the TMS coil utilized for applying TMS to the primary motor cortex (see 2.1.2) was pre-existing in the coil model package of SimNIBS® (Thielscher and Kammer, 2004) and was used to simulate the electric field induced over the primary motor cortex (Gassmann et al., 2022).

The following simulations were performed: TMS at RMT intensity over the left primary motor cortex and TMS at the individual cbTMS intensity applied to the respective subject (see 2.1.6.1) over the right cerebellar hemisphere (Gassmann et al., 2022).

In the SimNIBS® environment, the TMS coils were placed over the actual target utilized in the experiments (Gassmann et al., 2022). Thus, for the simulation of the generated electric field in the cerebellar cortex, the model of the cbTMS coil was set on the midpoint of the line from right mastoid to inion on the scalp (Gassmann et al., 2022). The intensity of TMS was adjusted to the respective cbTMS intensity of the participant (see 2.1.6.1) (Gassmann et al., 2022). For the primary motor cortex, the coil model was placed over the precentral gyrus of the left hemisphere (Gassmann et al., 2022). The electric fields' direction was set perpendicular to the precentral gyrus (Gassmann et al., 2022). The intensity of the current was set to the respective RMT of the participant (Gassmann et al., 2022).

2.1.7 REAL and SHAM-MS

Notably, all conditions involving any cerebral or cerebellar cortical target were divided into an equal number of two conditions, which were applied randomly intermixed – the REAL and the SHAM-MS conditions (Gassmann et al., 2022). The SHAM-MS (see 2.1.8.1) was applied to control for EEG responses to multisensory input (see 1.5.1) (Gassmann et al., 2022). The term REAL always refers to a TMS target involving cerebral or cerebellar cortex additionally to the SHAM-MS (see 1.5.1), while SHAM-MS never involves a target in the cerebellar or cerebral cortex (Gassmann et al., 2022). All corresponding stimuli of either REAL or SHAM-MS were delivered simultaneously (Gassmann et al., 2022).

2.1.8 Control conditions

Three control conditions were applied in this exploratory study to critically evaluate whether observed EEG responses to cbTMS were specific (see 1.5, 1.6) (Gassmann et al., 2022). Namely, a SHAM-MS, an occipital control condition and cbTMS with a different coil orientation inducing a downward current in the brain were administered (Gassmann et al., 2022).

2.1.8.1 SHAM-MS procedure & saturation approach

EEG responses to sensory input overlap in time with EEG responses evoked by TMS to cortical targets in the time-window beyond 60-70 ms post-TMS (Rocchi et al., 2021, Conde et al., 2019, Gordon et al., 2018, Biabani et al., 2019). To address the associated aforementioned challenges (see 1.5.1), a recently published sham procedure involving a titration of sensory EEG responses by increasing the TMS intensity in small increments for each individual (Gordon et al., 2021) was modified (Gassmann et al., 2022). This sham procedure aimed at a saturation of EEG responses to sensory input, utilizing the amplitude of the N100 as a marker for sensory-evoked responses (Gordon et al., 2021).

Likewise, the principle of the saturation approach in this study was to reach a plateau or saturation in the amplitude of sensory-evoked EEG responses in both the REAL and SHAM-MS conditions, since both conditions involved the SHAM-MS procedure (Figure 5) (see 1.5.1) (Gassmann et al., 2022). The EEG responses to SHAM-MS trials could then be subtracted from the EEG responses to the REAL trials, which involved cbTMS additionally to the SHAM-MS (Gassmann et al., 2022). In principle, this should have resulted in an EEG response corresponding to cbTMS without sensory-evoked EEG responses.

For experiment #1, the SHAM-MS consisted of MS to the right trapezius muscle, simultaneously delivered with ES to the neck set to the aforementioned parameters (see 2.1.2) (Gassmann et al., 2022). The intensity of SHAM-MS was individually titrated by delivering five blocks of SHAM-MS in increasing intensity (50 %MSO, 57 %MSO, 64 %MSO, 71 %MSO, 78 %MSO), each block consisting of 60 single-pulse MS combined with ES (Gassmann et al., 2022). After the five blocks, the N100 amplitude for each block was estimated (Gassmann et al., 2022). Data were analyzed for each block in a one-step independent component analysis (ICA) to reject excessive TMS artefacts, blink components, and eye movement components (Gassmann et al., 2022). From the processed data, the signal of the ten most negative channels was averaged for the time-window of 75-125 ms for an estimate of the N100 amplitude (Gassmann et al., 2022). The SHAM-MS intensity eliciting an estimated N100 response within one SD of the amplitude of the estimated N100 response of the next block was selected and fixed as the SHAM-MS intensity for the rest of the measurements in both the REAL and SHAM-MS conditions (Gassmann et al., 2022).

For experiment #2, a fixed SHAM-MS intensity of 85 %MSO was applied on the basis of the threshold determined in experiment #1 (Gassmann et al., 2022). At 78 %MSO, all subjects had reached a plateau in the estimated N100 response (Gassmann et al., 2022). Therefore, a fixed TMS intensity above this threshold was selected (Gassmann et al., 2022). Otherwise, the SHAM-MS procedure was applied with the same parameters as in experiment #1 (Gassmann et al., 2022).

2.1.8.2 Occipital control condition

The occipital control condition was conducted to clarify whether possible concomitant TMS to the occipital cortex could explain cbTMS-EEG responses (see 1.6) (Gassmann et al., 2022).

It involved one block of 280 trials, divided into 140 REAL trials and 140 SHAM-MS trials, delivered randomly intermixed (Gassmann et al., 2022). The SHAM-MS condition involved ES to the neck and MS to the shoulder as aforementioned (see 2.1.7) (Gassmann et al., 2022). The REAL condition involved the same ES and MS as the SHAM-MS, but additionally, single-pulse TMS to the right occipital cortex at the same TMS intensity as cbTMS (see 2.1.6.1) (Gassmann et al., 2022).

For the occipital control condition, the same TMS coil was utilized to deliver occipital cortex stimulation as was previously used to deliver cbTMS (Gassmann et al., 2022). The coil was placed over electrode O2 and an upward monophasic induced current in the tissue was delivered (Figure 5) (Garcia et al., 2011, Gassmann et al., 2022). The intertrial interval involved a jitter (Gassmann et al., 2022), to reduce the subjects' expectancy of the next TMS pulse (Ross et al., 2022).

2.1.8.3 Cerebellar TMS with a downward induced current

To test whether the direction of the induced current influences the EEG responses to cbTMS, the TMS coil utilized to deliver cbTMS was rotated 180°, to induce a downward current in the tissue (Figure 5) (Gassmann et al., 2022). Otherwise, the same TMS parameters as in the condition involving cbTMS with an upward induced current were applied (see 2.1.9) (Gassmann et al., 2022).

A total of 280 trials were obtained, of which 140 trials corresponded to the REAL and 140 trials corresponded to the SHAM-MS condition (Gassmann et al., 2022). SHAM-MS and REAL were delivered randomly intermixed (Gassmann et al., 2022). The SHAM-MS condition consisted of ES to the skin on the neck and MS to the right shoulder on the trapezius muscle, set to SHAM-MS intensity as aforementioned (see 2.1.8.1) (Gassmann et al., 2022). REAL involved the same ES and MS as the SHAM-MS, but in addition, single-pulse TMS to the right cerebellar cortex with a downward monophasic induced current (Gassmann et al., 2022). The cbTMS coil was placed on the midpoint between inion and mastoid and cbTMS intensity fixed to the TMS intensity previously determined after completion of CBI assessment (see 2.1.6.1) (Gassmann et al., 2022). The intertrial interval involved a jitter (Gassmann et al., 2022), to reduce the subjects' expectancy of the next trial and its sensory inputs (Ross et al., 2022).

2.1.9 Cerebellar TMS with an upward induced current

To effectively deliver cbTMS in the REAL condition, TMS was delivered to the right cerebellar hemisphere, with a monophasic, upward induced current in the cerebellar cortex (Gassmann et al., 2022). The cbTMS coil was placed on the midpoint between inion and mastoid (Figure 5) on the same spot as during CBI assessment and was set to the cbTMS intensity determined in CBI assessment (see 2.1.6.1) (Gassmann et al., 2022).

A total of 280 trials were obtained in the condition involving cbTMS with an upward induced current (Gassmann et al., 2022). Of those, 140 trials were corresponding to the SHAM-MS involving ES and MS (see 2.1.7) (Gassmann et al., 2022). Another 140 REAL trials involved the same ES and MS as SHAM-MS, however, cbTMS with an upward induced current was applied in addition (Gassmann et al., 2022). REAL and SHAM-MS were applied randomly intermixed (Gassmann et al., 2022). The intertrial interval involved a jitter (Gassmann et al., 2022), to reduce the subjects' expectancy of the next trial and its sensory inputs (Ross et al., 2022).

2.1.10 Data analysis

Analysis of EEG and EMG data, data processing, statistical analyses and creation of figures were conducted utilizing customized scripts on the MATLAB platform (MathWorks, 2017) and the open source toolbox FieldTrip (Oostenveld et al., 2011).

2.1.10.1 EEG data processing

EEG was recorded continuously, and TMS trigger markers were placed in the data during recording (Gassmann et al., 2022). Afterwards, the data were segmented into epochs according to the TMS markers (Gassmann et al., 2022). The definition of these epochs was from -0.5 s to +1 s around the TMS marker and they were baseline-corrected from -500 ms to +50 ms (Gassmann et al., 2022). Then, data from -6 ms to +20 ms around the TMS marker was removed in all epochs and interpolated with the FieldTrip interpolation method *p-chip* (Gassmann et al., 2022).

Thereafter, EEG data were visually inspected in two rounds (Gassmann et al., 2022). During the first round, the FieldTrip method *summary* was applied to reject trials and channels containing TMS ringing artefacts (Gassmann et al., 2022). In the second round of visual artefact rejection, all trials and channels were inspected trial by trial applying the FieldTrip mode *trial*, and those containing excessive artefacts were rejected (Table 2) (Gassmann et al., 2022). Then, the mean was subtracted from the data and the data was sampled down to 1 kHz (Gassmann et al., 2022)

After these preparations, a two-step ICA procedure was applied to the resulting data (Rogasch et al., 2014, Gassmann et al., 2022). During this ICA, ICA components were calculated and either retained or removed after a visual inspection (Gassmann et al., 2022). Whether am ICA component was removed or retained was decided after the inspection of their average time course, topography, power spectrum and single-trial time course (Rogasch et al., 2017, Gassmann et al., 2022).

During the first step of the ICA, exclusion of components was limited to those that contained high-amplitude TMS-related artefacts (Gassmann et al., 2022). Afterwards, a zero-phase Butterworth bandpass filter of the third order from 0.5 Hz to 100 Hz was administered to the resulting data (Gassmann et al., 2022).

During the second iteration of ICA, the removal of components was focused on those likely representing persistent muscle artefacts, line noise, eye blinks and eye movements (Gassmann et al., 2022). Then, if EEG channels were discarded previously, their signal was interpolated with the signal of the neighboring channels, utilizing the *spline* setting of FieldTrip (Gassmann et al., 2022). Lastly, the data were referenced to the average reference signal (Gassmann et al., 2022).

Table 2: Resting state: excluded trials, channels, and components during data processing

The table depicts the rejection of data in the process of data processing for the respective conditions. Each row corresponds to one experimental condition. The first column contains the percentage of excluded trials (mean ± 1 standard deviation (SD)) after visual artefact rejection. Visual artefact rejection was performed to remove trials and channels presenting excessive artefacts. The second column contains the percentage of excluded channels (mean ± 1 SD) after visual artefact rejection. The third and fourth column show the number of excluded components after the independent component analysis (ICA) in mean ± 1 SD of removed components in step 1 (ICA1) and step 2 (ICA2). The first round of ICA was limited to the removal of components containing high-amplitude transcranial magnetic stimulation (TMS) related artefacts. The second round of ICA focused on the removal of components representing persistent muscle artefacts, line noise, eye blinks and eye movements. **Source:** modified from (Gassmann et al., 2022).

Condition	**Trials**	**Channels**	**ICA 1**	**ICA 2**
cbTMS upward induced current (experiment #1)	**5.54%** ± 3.39%	**8.08%** ± 3.48%	**3.57** ± 2.21	**18.22** ± 5.28
cbTMS upward induced current (experiment #2)	**14.49%** ± 9.40%	**9.24%** ± 3.09%	**4.91** ± 3.78	**22.48** ± 3.91
Occipital control condition	**7.26%** ± 2.82%	**3.46%** ± 2.45%	**3.83** ± 2.10	**20.78** ± 5.48
cbTMS downward induced current	**25.89%** ± 9.06%	**9.65%** ± 2.24%	**4.00** ± 2.80	**26.35** ± 3.80

2.1.10.2 TMS-evoked potentials

After the completion of EEG data processing (see 2.1.10.1), the EEG epochs of each experimental condition were loaded and a zero-phase lowpass Butterworth filter of the third order (45 Hz) applied (Gassmann et al., 2022). Thereafter, TEPs elicited by SHAM-MS and REAL were computed from the EEG data (Gassmann et al., 2022). This was done by calculating the mean over all datasets of a given experimental condition, separated into SHAM-MS trials and REAL trials (Gassmann et al., 2022). Afterwards, EEG responses evoked by SHAM-MS were subtracted from EEG responses elicited by REAL (Gassmann et al., 2022). Additionally, the Global Mean Field Potential (GMFP) was calculated (Gassmann et al., 2022) as a measure to characterize global EEG activity (Esser et al., 2006, Lehmann and Skrandies, 1980). As is the convention in the field, peaks within the cerebellar TEP were labelled by their amplitude and latency.

2.1.10.3 TMS-EEG oscillatory response

To observe changes in oscillatory power at the time of TMS, the time-frequency response (TFR) was calculated utilizing the FieldTrip open source toolbox (Oostenveld et al., 2011, Pellicciari et al., 2017). To achieve this, time-frequency representations were calculated by applying a Morlet wavelet decomposition with frequency-dependent width on single trials (Gassmann et al., 2022). Adding 0.2 cycles for each Hertz, the wavelet width was 2.6 cycles at 4 Hz, (Gassmann et al., 2022).

This procedure was applied to the time-locked average of all trials, corresponding to the time-frequency representations of the evoked response (Pellicciari et al., 2017), and trial-by-trial (Gassmann et al., 2022). The time-frequency representations of the time-locked average of all trials were subtracted from the time-frequency representations of each individual trial (Pellicciari et al., 2017, Gassmann et al., 2022). Consequently, the evoked component in the TFR is eliminated, and the result is the oscillatory response induced by TMS. Afterwards, the time-frequency representations of each trial were z-transformed, and baseline corrected with the data from -500 ms to -100 ms (Pellicciari et al., 2017, Gassmann et al., 2022).

2.1.10.4 Statistical analysis

For the statistical analyses, scripts were created on the MATLAB platform (MathWorks, 2017). EEG responses from REAL and SHAM-MS conditions were compared by arithmetic subtraction (Gordon et al., 2021) within each experimental condition: cbTMS with an upward induced current in experiments #1 and #2, cbTMS with a downward induced current and the occipital control condition (Gassmann et al., 2022).

To analyze EEG responses, nonparametric cluster-based permutation statistics were utilized (Gassmann et al., 2022), which are effectual to control for errors resulting from executing multiple tests (Maris and Oostenveld, 2007). TEP-analysis involved cluster-based t-tests to identify time-windows in the REAL versus SHAM-MS EEG response showing significant differences (Gassmann et al., 2022). The function did not average over time and time windows were not pre-selected (Gassmann et al., 2022). The algorithm determined positive and negative clusters, which were then visually inspected (Gassmann et al., 2022). Within the indicated time windows, signals were then averaged and compared to yield possible significant EEG channel clusters (threshold: $p<0.05$) (Gassmann et al., 2022).

The analysis of induced oscillations was conducted in the same way, with the notable difference of pre-dividing into six frequency bands (Gassmann et al., 2022). The frequency bands were "*theta (θ, 4-7 Hz), alpha (α, 8-12 Hz), low beta (β1, 13-20 Hz), high beta (β2, 21-29 Hz), low gamma (γ1, 30-40 Hz) and high gamma (γ2, 60-90 Hz)*" (Gassmann et al., 2022). These frequency bands have a known physiological meaning. Due to the exploratory nature of this study, a subdivision into frequency bands of known physiological meaning was performed, reducing the degrees of freedom of the analysis and thus the chance of false positives, while accepting a higher chance of false negatives (Gassmann et al., 2022). As six statistical tests ($n=6$) were performed by subdividing into these frequency bands, the significance threshold was adjusted to $p<0.0083$ (Gassmann et al., 2022) with the Bonferroni method (Bonferroni, 1936). The definition of a significant cluster was >2 neighboring electrodes with $p<0.05$ (Gassmann et al., 2022). Monte Carlo p-values were calculated with a two-tailed test at the significance level p<0.025, utilizing 2000 iterations for induced oscillations and 1000 iterations for TEPs (Maris and Oostenveld, 2007, Gassmann et al., 2022).

After completion of these analyses, amplitude distributions of the identified cbTMS-specific clusters (see 4.2.1.1) were analyzed for conditions involving cbTMS, to provide normative data (Gassmann et al., 2022). The congruent significant EEG channels comprising the cbTMS-specific cerebellar P25 (cb-P25) and cerebellar N45 (cb-N45) clusters across cbTMS conditions were selected (Gassmann et al., 2022). Then, their signal was averaged for each subject (Gassmann et al., 2022). "*The most positive value for the cb-P25 and the most negative value for the cb-N45 were determined for each subject within the time-window of the cluster group average*" (Gassmann et al., 2022). Lastly, Gaussian distributions were fitted (Gassmann et al., 2022).

2.1.10.5 Correlation analysis

Pearson correlation analyses were conducted between the significant TEP- (Figure 22) and TFR-clusters (Figure 25) between REAL and SHAM-MS in the condition involving cbTMS with an upwards induced current (see 2.1.9) versus the respective CBI and cbTMS intensity values (Gassmann et al., 2022).

For TEP correlation analyses, the z-values were obtained by calculating the average TEP for each subject and performing a z-transformation. Then, the z-values were averaged over the channels comprising the respective cluster and averaged over the time-window of the respective cluster.

For the TFR correlation analyses, z-values were obtained by loading the previously calculated induced oscillations for each subject, divided into the six frequency bands. Then, data were averaged over the channels and frequencies comprising the respective cluster and averaged over the time-window of the respective cluster.

2.1.10.6 Source analysis

After the analyses previously detailed were conducted, the EEG responses from statistically significant and relevant results of control conditions (see 3.1.3) and the REAL cbTMS condition involving cbTMS with an upward induced current (see 3.1.4) were projected from the recorded two-dimensional EEG data into a three-dimensional source space derived from a commonly used brain atlas, the Montreal Neurological Institute and Hospital (MNI) coordinate system (Gassmann et al., 2022). A generic head model was calculated utilizing a meshed and segmented MNI brain (Gassmann et al., 2022) with the FieldTrip toolbox (Oostenveld et al., 2011).

In consequence, the results derived via this procedure should be understood as an approximation of the source in a generic head model and as an alternative visualization. Using the common MNI brain mesh, cortical surfaces and dipole arrays were obtained, with a forward model applying a customized pipeline (Stenroos and Nummenmaa, 2016), and considering standard EEG positions for the 10-10 montage used in these experiments (Gassmann et al., 2022). Then, reconstruction of the source was performed over the cerebral cortex, applying the L2-minimum-norm estimate (Hamalainen and Ilmoniemi, 1994, Gassmann et al., 2022). To project TEPs, "*each dipole's signal was normalized by z-transforming the signal of each trial with regard to the mean and standard deviation of the baseline prior to stimulation (−500 to −100 ms)*" (Gassmann et al., 2022).

2.1.11 Questionnaire – pain & discomfort

Assuring the tolerability of the applied procedures for subjects participating in cbTMS experiments applying high TMS intensities is relevant. Hence, the tolerability of the cbTMS procedure applied in these experiments was assessed among the participants who performed the full experiment, and volunteers aborting the experiment due to discomfort were reported as such (see 2.1.1) (Gassmann et al., 2022).

To assess the tolerability of the full procedure, participants were offered a pseudonymized numeric rating scale after experiments to indicate the subjective pain and discomfort levels on a scale from zero to ten during the experiments, separately for the SHAM-MS condition and the REAL condition (Dworkin et al., 2008, Gassmann et al., 2022).

"*A Wilcoxon signed-rank test was applied to the reported pain and discomfort scores to compare the REAL vs. SHAM-MS*" (Gassmann et al., 2022).

2.2 Applying the method in a clinical case

Parts of the following methods have been published in a letter-to-the-editor (Gassmann et al., 2023a).

In addition to the experiments in healthy subjects, the newly established protocol of cbTMS (Gassmann et al., 2022) was administered to a patient with a structurally impaired DTC on one side, due to secondary neurodegeneration (Gassmann et al., 2023a). This was conducted on the basis of the results of the resting state experiments (see 3.1) (Gassmann et al., 2022). Therefore, some reference to these results will be made in the following.

At the time of the cbTMS measurements, the patient had a pronounced asymmetry between left and right DTC (Figure 37) (Gassmann et al., 2023a). The objective was to compare cbTMS-evoked EEG responses between the intact and the structurally affected side (Gassmann et al., 2023a). The hypothesis was that EEG responses previously identified to be specifically evoked by cbTMS - namely the cb-P25 and cb-N45, which was interpreted to reflect an activation of the DTC (see 4.2.1.1) - will be observable on the intact side but will be altered or absent on the affected side (Gassmann et al., 2023a).

2.2.1 Patient & clinical syndrome (clinical case)

cbTMS was applied to one 58-year-old female right-handed (laterality index, +88.2, (Oldfield, 1971)) patient 36 months post-stroke (Gassmann et al., 2023a). The patient provided written informed consent before participation and agreed in written to the investigation of her medical documents and subsequent pseudonymized publication of results (Gassmann et al., 2023b). The study was approved by the ethics committee of the medical faculty of the University of Tübingen (715/2021BO). Experiments were conducted according to the current TMS safety guidelines of the International Federation of Clinical Neurophysiology (Rossi et al., 2021) and the patient was screened for the aforementioned contraindications (see 2.1.1) (Gassmann et al., 2023b).

The initial, acute clinical syndrome encompassed a mild left-sided hemiparesis and hemianesthesia with the initial cranial computer tomography in combination with angiography showing that the right posterior cerebral artery was occluded (PCA) (Gassmann et al., 2023a). "*A brain MRI 24 h later showed stroke demarcation encompassing large parts of the right temporal and occipital lobe, the right thalamus, and the splenium of the corpus callosum*" (Gassmann et al., 2023a).

When examining the patient before cbTMS measurements 36 months later on the day of the cbTMS measurements, she showed persistent slight left hemiparesis and hemihypesthesia (Gassmann et al., 2023a). Additionally, she presented a delayed-onset left hemichorea and hemiataxia, which were not described for the acute stage post-stroke, but instead had developed during the 36 months after the stroke occured (Gassmann et al., 2023a). Severity of the hemiataxia was tested utilizing the Scale for Assessment and Rating of Ataxia (SARA) score (Schmitz-Hubsch et al., 2006), with the patient scoring 13.5 points in total (see 3.2.1), indicating mild to moderate ataxia symptoms (Gassmann et al., 2023a). The items of the score that differentiated left to right indicated an asymmetry of the clinical symptoms, with the left side of the body being more strongly affected (Gassmann et al., 2023a).

The aforementioned clinical symptoms of persisting hemiparesis and hemihypesthesia combined with delayed-onset hemichorea, which was progressive (Gassmann et al., 2023b), is consistent with symptoms resulting from the observed ischemic lesions in the ventroposterior thalamus and pulvinar (Figure 37) (Zijlmans, 2011, Gassmann et al., 2023b). These brain regions are supplied by the thalamogeniculate artery. Especially the delayed onset of the left-sided hemiataxia was interpreted to be reflective of the observed neurodegeneration of the left DTC (Gassmann et al., 2023a) – as this is a distinctive feature neurodegenerative ataxic syndromes with adult onset (Faber et al., 2020).

2.2.2 Cerebellar TMS parameters (clinical case)

cbTMS-EEG was delivered to the left and right cerebellar hemisphere, applying the protocol of the resting state experiments (Materials see 2.2) (Gassmann et al., 2022). Masking noise was applied throughout measurements by the same parameters as in resting state experiments (see 2.1.3) (Gassmann et al., 2023b). The cbTMS intensity was determined by titrating the cbTMS intensity until a CBI of ≤0.85 was observed (Gassmann et al., 2023a). This intensity was used for the cbTMS-EEG measurements (Gassmann et al., 2023a). CBI assessment followed the same parameters as in the resting state experiments (see 2.1.6.1) (Gassmann et al., 2023a).

For this clinical subject, no sham condition was applied (Gassmann et al., 2023a). Otherwise, the same TMS parameters as in the resting state experiments were applied (see 2.1.9) (Gassmann et al., 2023a). This was decided since the main results of resting state experiments - the cb-P25 and the cb-N45 - occurred before 60 ms post-TMS (see 4.2.1) (Gassmann et al., 2022) and are thus not overlapping in time with sensory-evoked EEG responses (Rocchi et al., 2021, Conde et al., 2019, Gordon et al., 2018, Biabani et al., 2019). By reducing the number of conditions, it was aimed at increasing the tolerability for the patient (Gassmann et al., 2023a). "*Hence, only significant EEG clusters < 60 ms post-TMS were considered specifically attributable to cbTMS in the statistical analysis (Gassmann et al., 2022)*" (Gassmann et al., 2023a).

2.2.3 Magnetic resonance imaging & diffusion tensor imaging tractography (clinical case)

Anatomical T1-weighted MRI and diffusion tensor imaging (DTI) were performed (Figure 37) (Gassmann et al., 2023a). A SIEMENS Prisma scanner was utilized to obtain images, using a 2-dimensional echo planar imaging diffusion sequence with a repetition time of 3600 ms, an echo time of 64 ms, isometric 2 x 2 x 2 mm voxels, and a b-value of 1500 s/mm² (Gassmann et al., 2023a).

For reconstruction of the DTC via DTI tractography, "*a* […] *diffusion scheme was used, and a total of 64 diffusion sampling directions were acquired. The accuracy of b-table orientation was examined by comparing fiber orientations with those of a population-averaged template (Yeh et al., 2018). A deterministic fiber tracking algorithm was used (Yeh et al., 2013)* […]. *The anisotropy threshold was set at 0.2 to minimize spurious fibers reconstruction. The angular threshold and step size were randomly selected from 15 degrees to 90 degrees and from 0.5 voxel to 1.5 voxels, respectively. The fiber trajectories were smoothed by averaging the propagation direction with 50% of the previous direction. Streamlines with length shorter than 20 or longer than 300 mm were automatically discarded. A total of 2000000 seeds were placed for accurate reconstruction of each* […] *tract. Non-decussating fibers were manually removed. For volumetric analyses, streamlines were voxelated as described by Yeh (Yeh, 2020). This method allowed for total tract volume calculation, which corresponds to the product of the number of streamline-traversed voxels and voxel size. By creating a 3D volume of the voxelated streamlines, surface voxels can be identified as constituting the outer shell of the tract. The total surface area of the tracts then corresponds to the number of surface voxels multiplied by the square of the voxel spacing (Yeh, 2020).*" (Gassmann et al., 2023a). By this method, the volume of the corresponding DTC was calculated from the reconstructed streamlines (Gassmann et al., 2023a).

2.2.4 Electric field simulation (clinical case)

Electric fields generated by the aforementioned TMS coil models (see 2.1.6.2), which were models of the TMS coils utilized in the current experiments, were simulated in SimNIBS® (Thielscher et al., 2015, Gassmann et al., 2023a). "*The patient's anatomical T1-weighted MRI was segmented and meshed with the built-in headreco tool (Nielsen et al., 2018)*" (Gassmann et al., 2023a) to accurately model the target the electric field was applied to (Gassmann et al., 2023a). Then, three simulations were conducted (Gassmann et al., 2023a).

The first simulation modelled the electric field applied over the left primary motor cortex during RMT assessment (Gassmann et al., 2023a). For this simulation, "*the coil model was set on the scalp region atop the left precentral gyrus, with the direction of the E-field* [electric field] *perpendicular to the gyrus and setting current intensity corresponding to the individual RMT.*" (Gassmann et al., 2023a). The second and third simulations modelled the electric field generated over the right and left cerebellar hemisphere (Gassmann et al., 2023a). For these simulations, "*the coil was set on the midpoint between the inion and the mastoid for the left and right side, with an upward direction of the induced E-field* [electric field]*. The stimulation intensity was set to the applied cbTMS intensity* […]*. The wearing of the EEG cap was factored into the E-field* [electric field] *estimations.*" (Gassmann et al., 2023a).

2.2.5 Data analysis (clinical case)

EEG and EMG data were processed and analyzed with customized scripts on the MATLAB platform (MathWorks, 2017), utilizing the FieldTrip toolbox (Oostenveld et al., 2011) in the same way as described for resting state (see 2.1.10.1) (Gassmann et al., 2023a). "*For the analysis of the EEG data, the examiner was blinded as to whether the data was derived from cbTMS to the right or to the left hemisphere.*" (Gassmann et al., 2023a). The rejected trials, channels and components are listed in Table 3.

"*The EEG was recorded continuously and segmented post-hoc, using the trigger markers of the TMS pulses in the data. Epochs were defined from -0.5 s to +1 s around the marker and baseline-corrected (−500 ms to −50 ms).* […] *Data 6 ms before to 20 ms after the marker of the TMS pulse were removed and interpolated using the FieldTrip method "p-chip" in order to eliminate the TMS artifact from the recordings. EEG data were inspected visually. Trials and channels containing excessive artifacts were excluded* […]*. In the second round, data were visually inspected trial-wise. Then, a two-step independent component analysis* […] *was* *performed on the retained data in order to remove signal artifacts related to the TMS pulse, eye movements and persistent muscle activity* […] *(Rogasch et al., 2014). Discarded EEG-channels were interpolated, using the signal of the neighboring channels. The data was re-referenced to the average reference signal. After processing the data, EEG trials were loaded for left-hemispheric cbTMS or right-hemispheric cbTMS and visualized. They were subjected to lowpass filtering (45 Hz, zero-phase Butterworth, 3rd order).*" (Gassmann et al., 2023a).

Table 3: Clinical case: excluded trials, channels, and components during data processing

The table contains the excluded data after data processing. The first column details the type of excluded data. The second column represents the excluded data for the condition involving cerebellar transcranial magnetic stimulation (cbTMS) to the right cerebellar hemisphere, the third column for cbTMS to the left cerebellar hemisphere. Visual artefact rejection was conducted to remove trials or channels with excessive noise in the electroencephalography (EEG) signal. Trials: number of removed trials in percent after visual artefact rejection. Channels: number of removed channels after visual artefact rejection. Independent component analysis (ICA) was conducted in two steps, the first round of ICA was limited to the removal of components containing high-amplitude TMS-related artefacts. The second round of ICA focused on the removal of components representing persistent muscle artefacts, line noise, eye blinks and eye movements. ICA: number of removed components in step 1 (ICA1) and step 2 (ICA2) of the ICA. **Source:** modified from (Gassmann et al., 2023a).

Excluded Data	Right cbTMS	Left cbTMS
Trials	7.5%	8.3%
Channels	4	7
ICA1	9	7
ICA2	25	27

2.2.6 Statistical analysis (clinical case)

"*Analyses were performed on the MATLAB platform (R2017b, The Mathworks, USA)* [(MathWorks, 2017)] *utilizing the FieldTrip toolbox (Oostenveld et al., 2011). The EEG responses elicited by right-hemispheric and left-hemispheric cbTMS were compared by non-parametric cluster-based permutation statistics (Gassmann et al., 2022, Maris and Oostenveld, 2007). A cluster-based* *independent samples t-test was performed, having single TMS trials as observations, was used to identify EEG channels and time points (between 20 ms and 60 ms after TMS) in which left-hemispheric vs. right-hemispheric cbTMS-evoked EEG signals were significantly different. The function did not average over time and further time-windows were not pre-selected. Since no sham stimulation was applied, significant differences beyond 60 ms post-TMS were not considered, as they possibly overlap with EEG responses to multisensory input (Conde et al., 2019, Gordon et al., 2021, Ahn and Frohlich, 2021, Biabani et al., 2019, Rocchi et al., 2021). Afterwards, the signals were averaged within the time windows indicated by the algorithm and compared, yielding significant EEG channel clusters (threshold: p<0.01). A significant cluster was defined as ≥2 neighboring electrodes with p<0.01. Monte Carlo p-values were calculated via a two-tailed test at the significance level p<0.025, using 2000 iterations for TEPs (Maris and Oostenveld, 2007).*" (Gassmann et al., 2023a).

3 Results

3.1 Resting state

Parts of the following results have been published in an original research article (Gassmann et al., 2022).

3.1.1 Resting motor threshold assessment

The mean RMT, averaged over all 46 subjects, was 42.4 ± 5.8 %MSO (mean ± 1 SD) in experiment #1 and 44.1 ± 6.9 %MSO (mean ± 1 SD) in experiment #2 (Gassmann et al., 2022).

3.1.2 Confirming cerebellar cortex stimulation

3.1.2.1 Cerebellar brain inhibition

The average CBI ratio over all 46 subjects was 0.85 ± 0.13 (mean ± 1 SD) (Gassmann et al., 2022). Averaging over all 23 subjects of experiment #1, the mean CBI was 0.88 ± 0.12 (mean ± 1 SD) (Gassmann et al., 2022). As for the average of all 23 subjects of experiment #2, it was 0.83 ± 0.14 (mean ± 1 SD) (Gassmann et al., 2022). In total, 38 subjects elicited a CBI within ± 1 SD of the mean CBI (Figure 8) (Gassmann et al., 2022). Averaged over all 23 subjects of experiment #1, the mean intensity applied to deliver cbTMS was 74.5 ± 10.7 %MSO (mean ± 1 SD) (Gassmann et al., 2022). When averaging over all 23 subjects of experiment #2, the mean intensity applied to deliver cbTMS was 75.8 ± 11.1 %MSO (mean ± 1 SD) (Gassmann et al., 2022).

There was no significant difference ($p>0.05$) between the two groups for CBI or cbTMS intensity (Gassmann et al., 2022).

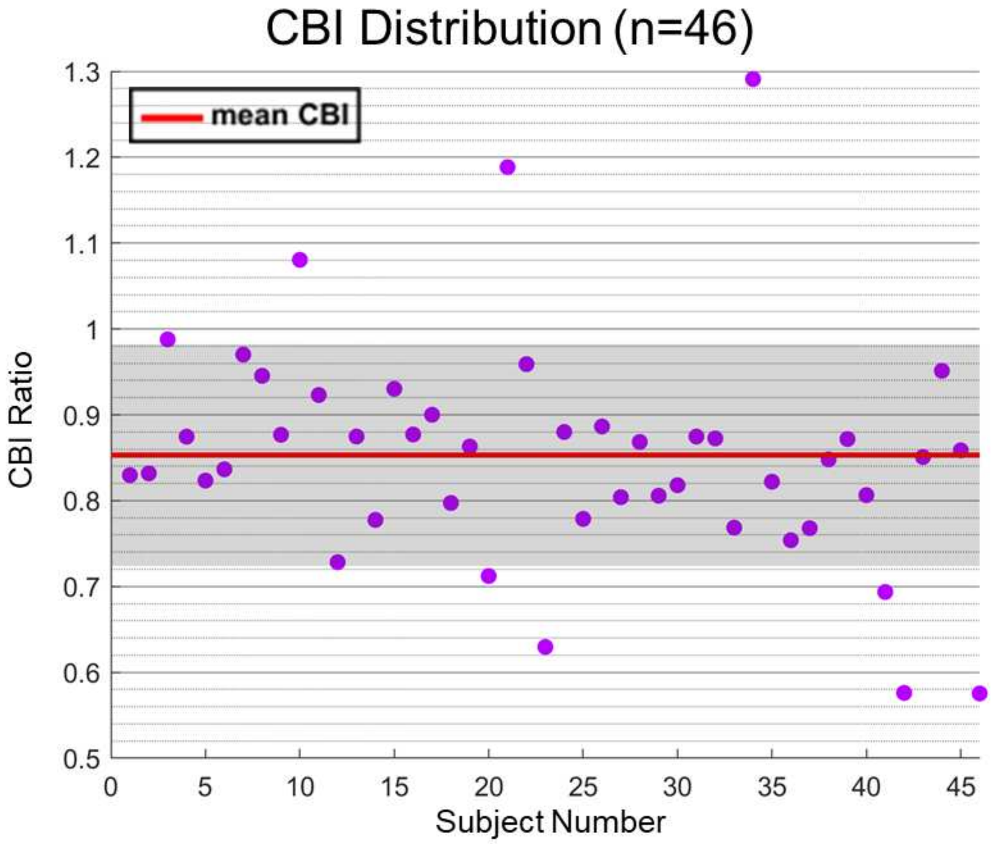

Figure 8: Distribution of cerebellar brain inhibition

The cerebellar brain inhibition (CBI) for each subject is displayed. Each purple dot represents the CBI value of one subject. The mean CBI (n=46) is displayed as a red horizontal line. The grey shaded area represents one standard deviation (SD) of the mean. **Y-axis:** CBI ratio value. **X-axis:** subject number.

3.1.2.2 Electric field simulation

The simulation of the electric field induced by TMS was conducted for the primary motor cortex and the cerebellar cortex (Gassmann et al., 2022).

Over the primary motor cortex, the simulated electric field was centered on the left-hemispheric precentral gyrus (Gassmann et al., 2022). The average peak strength of the electric field in the tissue was 87 V/m (Gassmann et al., 2022). As the simulated TMS intensity was set to the RMT of the respective subject (Gassmann et al., 2022), this electric field strength in the cortex was capable of eliciting MEPs by depolarizing neurons in the primary motor cortex.

Over the cerebellar cortex, the center of the simulated electric field was on the posterior, lateral right cerebellar cortex of the right cerebellar hemisphere, around the horizontal fissure (Gassmann et al., 2022). The average peak strength of the simulated electric field was 120 V/m (Gassmann et al., 2022). Notably, the simulated electric field encompassed inferior-posterior parts of the occipital lobe, corresponding to the secondary visual cortex (Figure 9) (Gassmann et al., 2022).

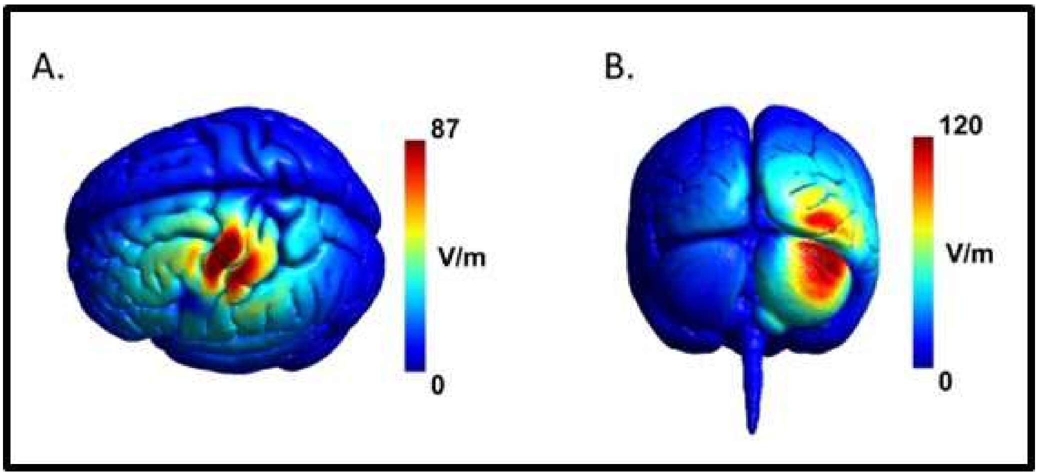

Figure 9: Simulation of the average TMS-induced electric field

A. Transcranial magnetic stimulation (TMS) to the left primary motor cortex at individual resting motor threshold (RMT) intensity. **B.** TMS to the right cerebellar hemisphere at the individually applied cerebellar TMS (cbTMS) intensity. All data correspond to an average of the 8 investigated subjects, projected on a standard brain derived from a common brain atlas (Montreal Neurological Institute (MNI)). Color bars next to the plots indicate electric field strength in the plot in Volt per meter (V/m) **Source:** from (Gassmann et al., 2022), black frame added, legend modified.

3.1.2.3 Individual results

In the following, the individual results for the CBI assessment of all subjects and the 8 individual electric field simulations are presented (Figure 10, Figure 11).

Dataset	Averaged MEP	Cerebellar brain inhibition	Individual electric field simulation
001	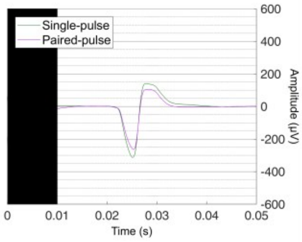	$\frac{406.41\ \mu V}{488.59\ \mu V} \approx 0.83$	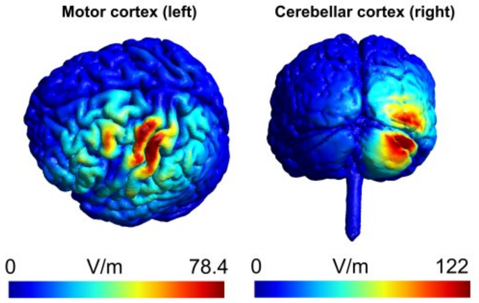
002	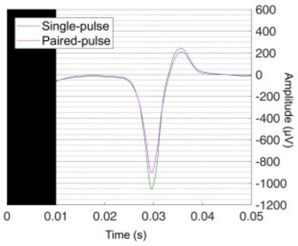	$\frac{1201.30\ \mu V}{1373.69\ \mu V} \approx 0.87$	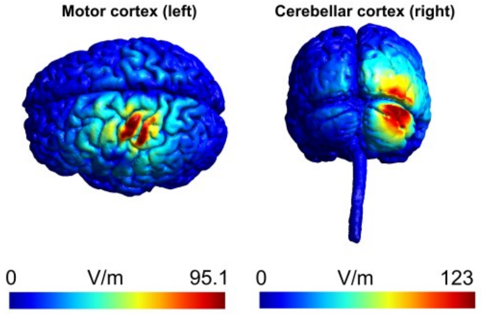
003	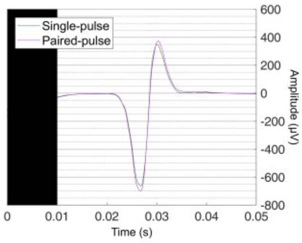	$\frac{1167.20\ \mu V}{1080.21\ \mu V} \approx 1.08$	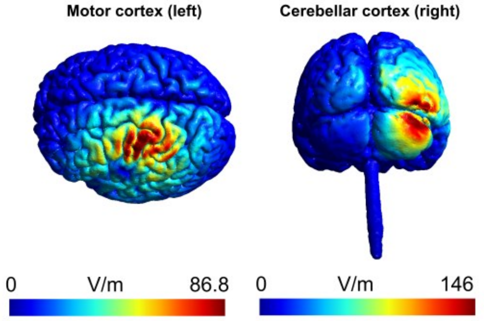
004	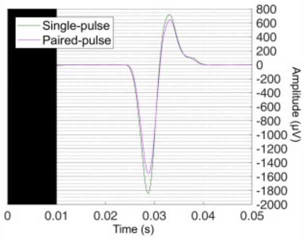	$\frac{2286.27\ \mu V}{2649.20\ \mu V} \approx 0.86$	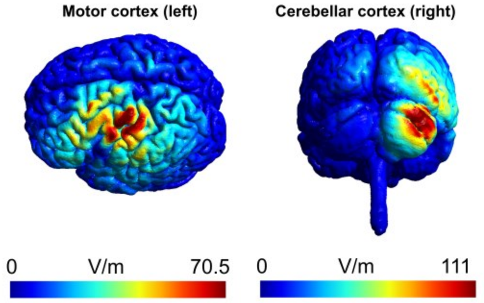

Dataset	Averaged MEP	Cerebellar brain inhibition	Individual electric field simulation
005	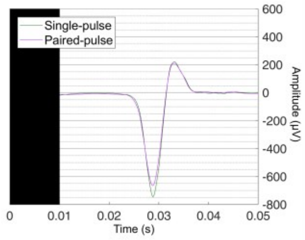	$\frac{989.89\ \mu V}{1032.24\ \mu V} \approx 0.96$	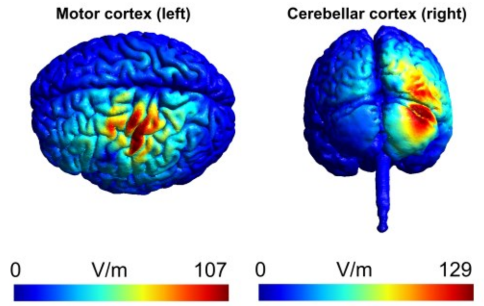
006	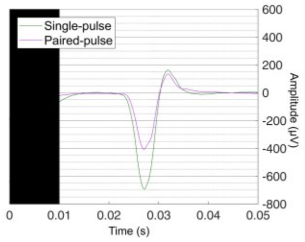	$\frac{612.86\ \mu V}{973.45\ \mu V} \approx 0.63$	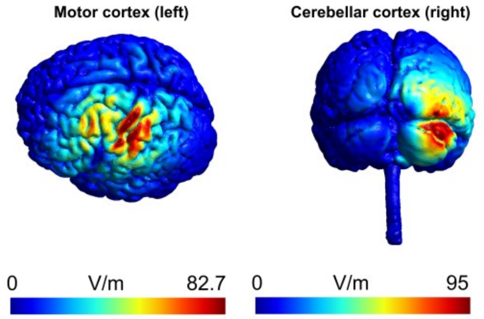
007	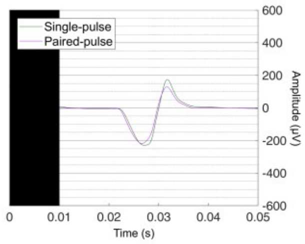	$\frac{398.24\ \mu V}{452.56\ \mu V} \approx 0.88$	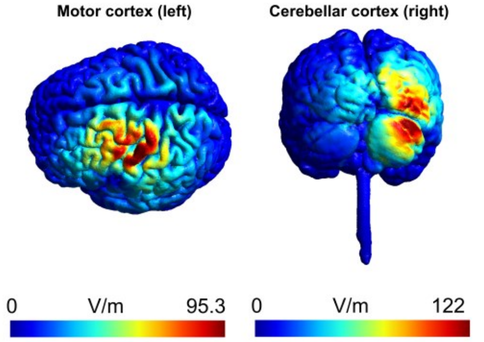
008	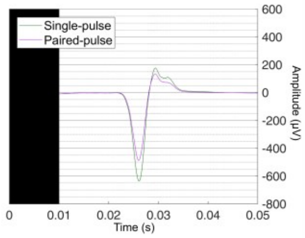	$\frac{669.58\ \mu V}{871.95\ \mu V} \approx 0.77$	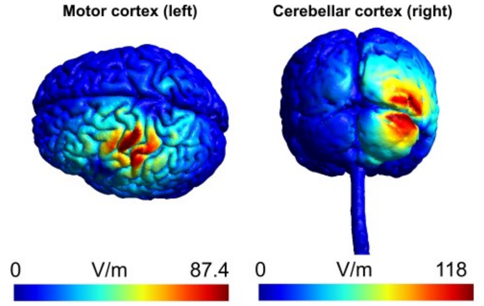

Figure 10: Individual CBI calculations and electric field simulations

The individual cerebellar brain inhibition (CBI) calculations, as well as the individual SimNIBS® models for the subgroup of subjects with anatomical individual magnetic resonance imaging (MRI) (n=8) are displayed. Each row of the table corresponds to one individual dataset. **First column:** Dataset number. **Second column:** The individual average motor evoked potentials (MEPs) obtained during CBI assessment are displayed, for single-pulse transcranial magnetic stimulation (TMS) to the left primary motor cortex (green) and paired-pulse TMS to the right cerebellar hemisphere and left primary motor cortex (purple). Black bar indicates the exclusion period around the TMS pulse (time = 0s). X-axis: time in seconds (s) after the TMS pulse to primary motor cortex. Y-axis: amplitude in µV of the electromyography (EMG) of the target muscle. **Third column:** Individual calculation of the CBI. **Fourth column:** SimNIBS® modeling, utilizing individual MRI. Color bars are located below the plots, indicating electric field strength in Volt per meter (V/m). **Left:** Simulation of TMS to the left primary motor cortex with TMS intensity set to the individual resting motor threshold (RMT). Superior view on the left hemisphere. **Right:** Simulation of TMS to the right cerebellar hemisphere with TMS intensity set to the individual cerebellar TMS (cbTMS) intensity. Posterior view. **Source:** taken from (Gassmann et al., 2022), figure and legend modified.

Dataset	Averaged MEP	Cerebellar brain inhibition
001	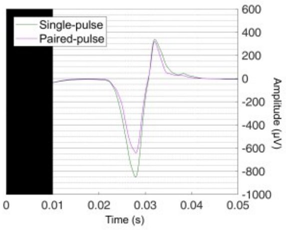	$\frac{1111.52\ \mu V}{1339.68\ \mu V} \approx 0.83$
002	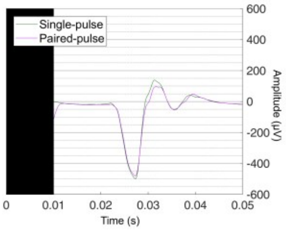	$\frac{797.90\ \mu V}{807.74\ \mu V} \approx 0.99$
003	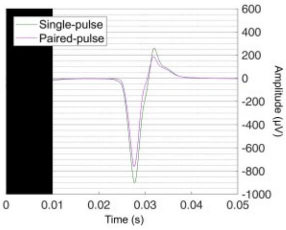	$\frac{1014.81\ \mu V}{1232.54\ \mu V} \approx 0.82$
004	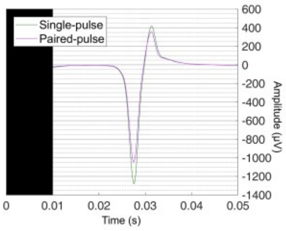	$\frac{1447.62\ \mu V}{1730.56\ \mu V} \approx 0.84$

Dataset	Averaged MEP	Cerebellar brain inhibition
005	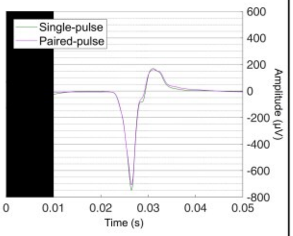	$\frac{926.86\ \mu V}{955.40\ \mu V} \approx 0.97$
006	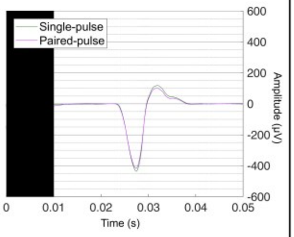	$\frac{553.88\ \mu V}{585.88\ \mu V} \approx 0.95$
007	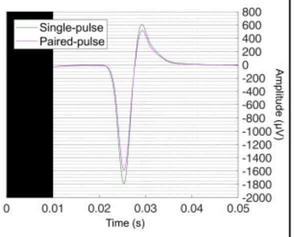	$\frac{2135.79\ \mu V}{2436.17\ \mu V} \approx 0.88$
008	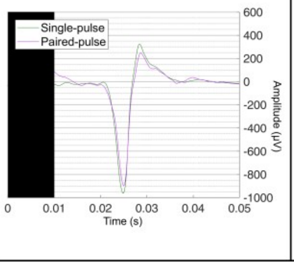	$\frac{1365.57\ \mu V}{1479.40\ \mu V} \approx 0.92$

Dataset	Averaged MEP	Cerebellar brain inhibition
009	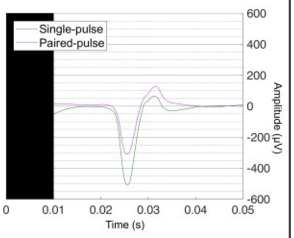	$\frac{474.35\ \mu V}{651.32\ \mu V} \approx 0.73$
010	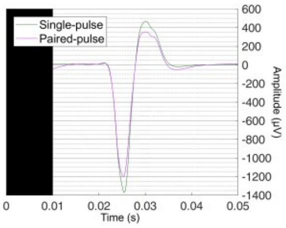	$\frac{1805.04\ \mu V}{2063.6\ \mu V} \approx 0.87$
011	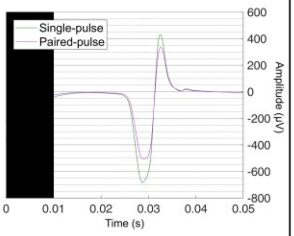	$\frac{903.32\ \mu V}{1161.74\ \mu V} \approx 0.78$
012	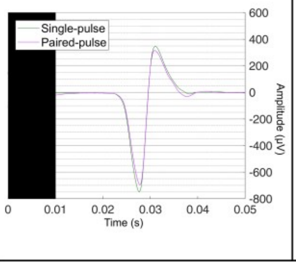	$\frac{1103.66\ \mu V}{1186.45\ \mu V} \approx 0.93$

Dataset	Averaged MEP	Cerebellar brain inhibition
013	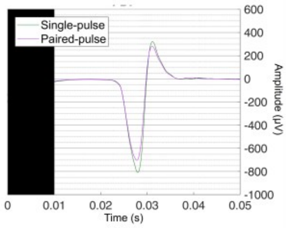	$\frac{1047.46\ \mu V}{1194.28\ \mu V} \approx 0.88$
014	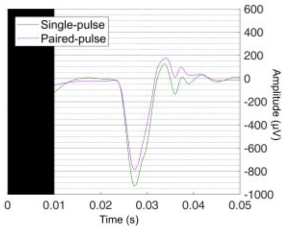	$\frac{1118.42\ \mu V}{1242.62\ \mu V} \approx 0.90$
015	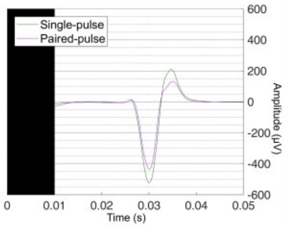	$\frac{658.89\ \mu V}{826.43\ \mu V} \approx 0.80$
016	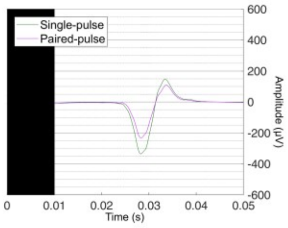	$\frac{367.15\ \mu V}{515.52\ \mu V} \approx 0.71$

Dataset	Averaged MEP	Cerebellar brain inhibition
017	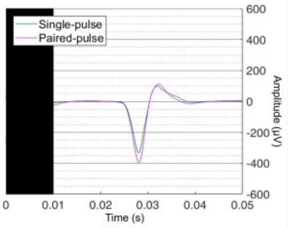	$\frac{564.46\ \mu V}{474.93\ \mu V} \approx 1.19$
018	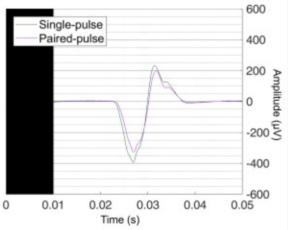	$\frac{603.76\ \mu V}{775.30\ \mu V} \approx 0.78$
019	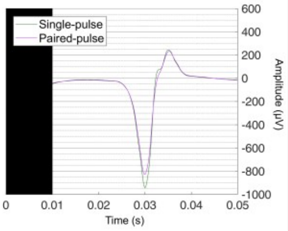	$\frac{1145.25\ \mu V}{1292.11\ \mu V} \approx 0.89$
020	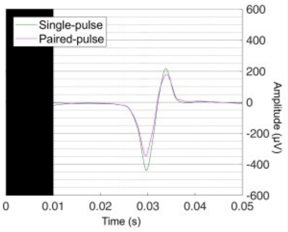	$\frac{556.14\ \mu V}{691.69\ \mu V} \approx 0.80$

Dataset	Averaged MEP	Cerebellar brain inhibition
021	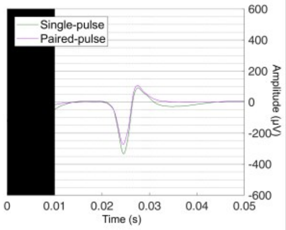	$\frac{416.72\ \mu V}{479.92\ \mu V} \approx 0.87$
022	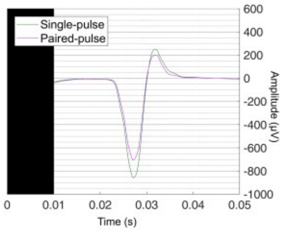	$\frac{998.79\ \mu V}{1239.61\ \mu V} \approx 0.81$
023	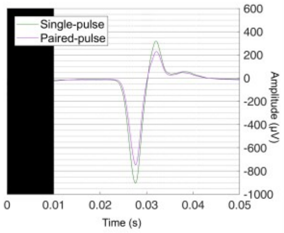	$\frac{1094.4\ \mu V}{1338.02\ \mu V} \approx 0.82$
024	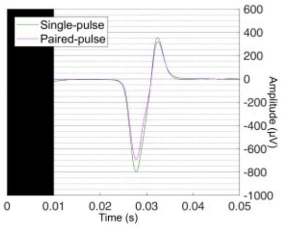	$\frac{1028.59\ \mu V}{1175.99\ \mu V} \approx 0.87$

Dataset	Averaged MEP	Cerebellar brain inhibition
025	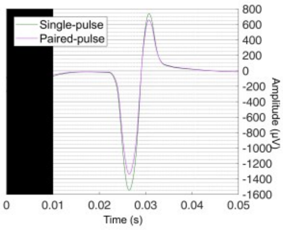	$\frac{2022.57\ \mu V}{2318.03\ \mu V} \approx 0.87$
026	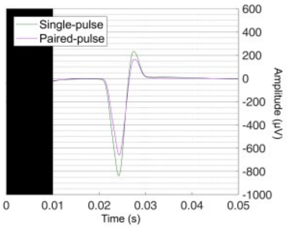	$\frac{841.64\ \mu V}{1095.09\ \mu V} \approx 0.77$
027	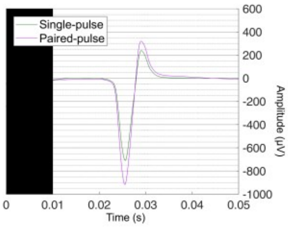	$\frac{1302.27\ \mu V}{1008.65\ \mu V} \approx 1.29$
028	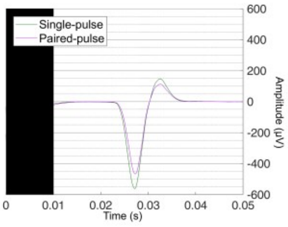	$\frac{614.83\ \mu V}{747.89\ \mu V} \approx 0.82$

Dataset	Averaged MEP	Cerebellar brain inhibition
029	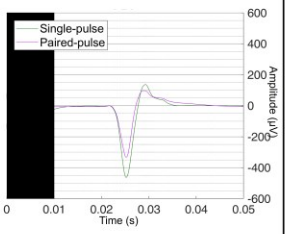	$\frac{477.48\ \mu V}{633.35\ \mu V} \approx 0.75$
030	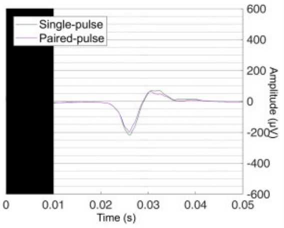	$\frac{297.07\ \mu V}{350.3\ \mu V} \approx 0.85$
031	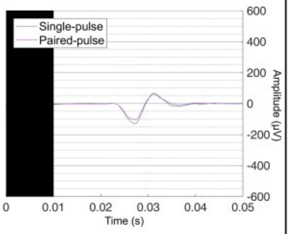	$\frac{189.71\ \mu V}{217.61\ \mu V} \approx 0.87$
032	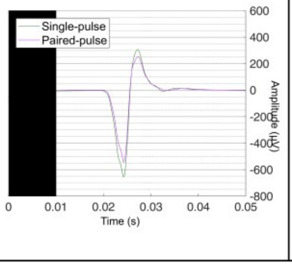	$\frac{881.29\ \mu V}{1092.82\ \mu V} \approx 0.81$

Dataset	Averaged MEP	Cerebellar brain inhibition
033	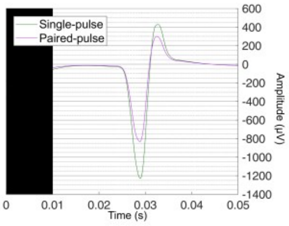	$\frac{1199.12\ \mu V}{1728.84\ \mu V} \approx 0.69$
034	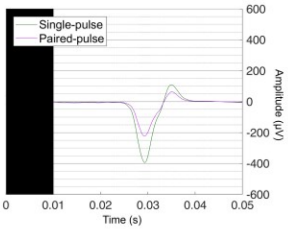	$\frac{314.28\ \mu V}{545.57\ \mu V} \approx 0.58$
035	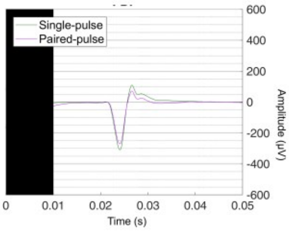	$\frac{388.92\ \mu V}{457.11\ \mu V} \approx 0.85$

Dataset	Averaged MEP	Cerebellar brain inhibition
036	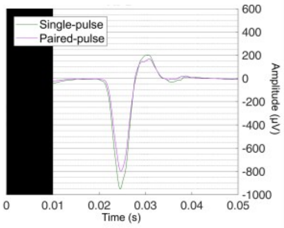	$\frac{1119.49\mu V}{1303.87\mu V} \approx 0.86$
037	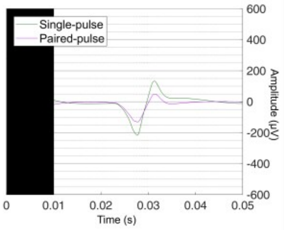	$\frac{218.03\ \mu V}{378.94\ \mu V} \approx 0.58$
038	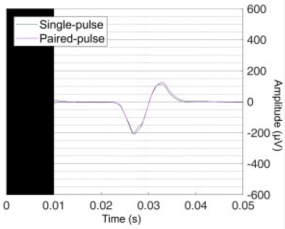	$\frac{357.66\ \mu V}{375.99\ \mu V} \approx 0.95$

Figure 11: Individual CBI calculation

The individual cerebellar brain inhibition (CBI) calculations are displayed. Each calculation corresponds to one individual. Two tables are shown next to one another, for each table, the columns are described. **First column**: Dataset number. **Second column**: The individual average motor evoked potential (MEP) obtained during CBI assessment is displayed, for single-pulse TMS to left primary motor cortex (green) and paired-pulse TMS to the right cerebellar hemisphere and left primary motor cortex (purple). **X-axis:** Time in seconds (s) after the TMS pulse to the primary motor cortex. **Y-axis:** Amplitude in μV in the electromyography (EMG) of the target muscle. **Third column:** Individual calculation of the CBI. **Source:** modified from (Gassmann et al., 2022).

3.1.3 Control conditions

3.1.3.1 SHAM-MS procedure & saturation approach

Applying the saturation approach in experiment #1 (see 2.1.8.1), a plateau of the amplitude of the N100 response could be identified for all subjects (Figure 12) (Gassmann et al., 2022). Calculating the average EEG response ±1 standard error of the mean (SEM) (n=23) in the time window 75 to 125 ms after SHAM-MS was delivered for each of the five blocks of increasing SHAM-MS intensity, an overlapping of the SEM bars could be observed (Figure 12) (Gassmann et al., 2022). Between the average EEG response to the 71 %MSO block and the 78 %MSO block, no significant difference was observed on the group level (p>0.05).

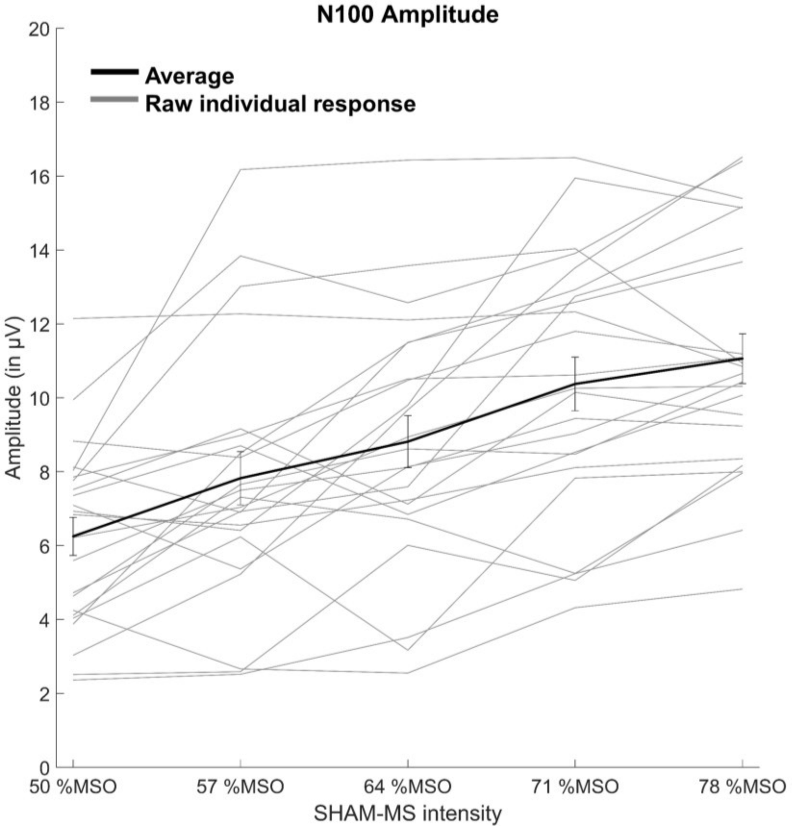

Figure 12: Saturation approach results

Depicted is the amplitude of the N100 component in the electroencephalography (EEG) results elicited in five blocks of increasing magnetic stimulation (MS) during the titration of SHAM-MS. The EEG response was averaged over the time window of 75-125 ms after SHAM-MS was delivered. Then, the ten EEG channels with the largest N100 component in this time window were selected and averaged. In grey, the raw EEG response amplitude in this time window is displayed, with each line representing one individual (n=23). The average EEG signal over all subjects (n=23) of experiment #1 is displayed in black, with the error bars representing ±1 standard error of the mean (SEM). **X-axis:** intensity of MS in %MSO. **Y-axis:** N100 amplitude in µV. **Source:** taken from (Gassmann et al., 2022), figure and legend modified.

3.1.3.2 Occipital control condition

When inspecting the EEG signals elicited by REAL and SHAM-MS in the occipital control condition (see 2.1.8.2), several differences could be observed (Figure 13) (Gassmann et al., 2022). The REAL of the occipital control condition, involving TMS to the right occipital cortex, elicited a localized early positive deflection in electrodes over the right occipital cortex, 20 ms to 45 ms after REAL was applied

(Gassmann et al., 2022). In the same time window, a negative deflection in electrodes over the left parietal cortex was observed (Gassmann et al., 2022). These responses were not observed in the SHAM-MS (Gassmann et al., 2022). In the time window beyond 70 ms, both SHAM-MS and REAL elicited a large-amplitude, negative response in fronto-central electrodes peaking after ~100 ms, followed by a large-amplitude positive deflection in central electrodes after ~200 ms (Gassmann et al., 2022). The subtraction of SHAM-MS from REAL, following the saturation approach rationale (see 2.1.8.1), revealed a late positive deflection 200 ms to 480 ms at the target site in electrodes over the right occipital cortex (Figure 13) (Gassmann et al., 2022).

When comparing the TEPs elicited by REAL and SHAM-MS in the occipital control condition via a cluster-based permutation t-statistics (see 2.1.10.2), several significant and relevant clusters were observed (Gassmann et al., 2022). Namely, the aforementioned localized early positive deflection over the targeted right occipital cortex from 20 ms to 45 ms, the mirrored focal negative deflection over the left parietal cortex and the late positive deflection from 200 ms to 480 ms at the target site over the right occipital cortex were observed (Figure 14) (Gassmann et al., 2022). Notably, no significant differences (p>0.05) were observed in the time window beyond 60 ms after REAL or SHAM-MS were delivered (Gassmann et al., 2022).

Following the calculation of TFRs (see 2.1.10.3) elicited by REAL and SHAM-MS in the occipital control condition, SHAM-MS was subtracted from REAL (Gassmann et al., 2022). Both conditions elicited an early increase in low gamma and high gamma power, as well as a late decrease in alpha power (Gassmann et al., 2022). When subtracting SHAM-MS from REAL, a difference in early high beta power was observed at the site of TMS (Figure 15) (Gassmann et al., 2022).

When comparing the TFRs elicited by REAL and SHAM-MS utilizing a cluster-based permutation t-statistics (see 2.1.10.4), a significant early increase in high beta power centered at the site of stimulation from 50 ms to 120 ms was observed (Gassmann et al., 2022). Furthermore, a later increase in high gamma power in electrodes over central posterior regions from 120 ms to 150 ms was found (Figure 16) (Gassmann et al., 2022).

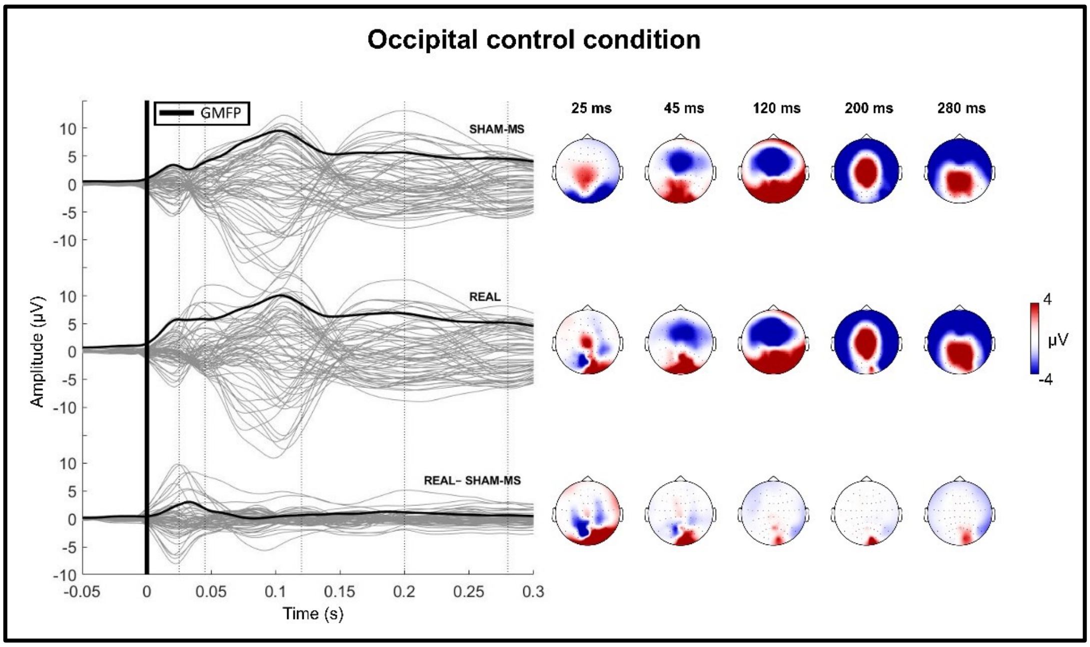

Figure 13: Occipital control condition: time courses and spatial distributions of the EEG signals

Butterfly plots (left) display the time course of the electroencephalography (EEG) responses following SHAM-MS (top) and REAL (middle), and the subtraction of SHAM-MS from REAL (bottom: REAL – SHAM-MS), averaged across all subjects (n=23). Each gray line corresponds to the signal from one EEG channel. The black line corresponds to the Global Mean Field Potential (GMFP). The vertical black bar indicates the time of stimulation (0 s) and the period of data exclusion contaminated by the stimulation artefact (-6 ms to +20 ms). X-axis: time in seconds (s). Y-axis: amplitude in µV. Dotted lines represent the time-points that are displayed in the topographical plots (right). Colors in the topographical plots indicate voltage in µV, as shown in the calibration bar to the right. **Source:** taken from (Gassmann et al., 2022), figure and legend modified.

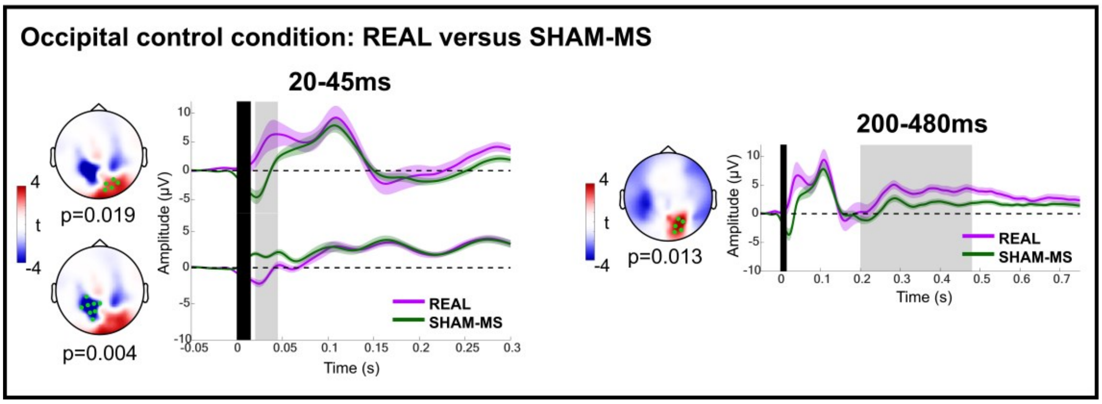

Figure 14: Occipital control condition: statistical comparison of TMS-evoked EEG responses from REAL and SHAM-MS

Topographical plots represent results from the cluster-based t-statistics (REAL versus SHAM-MS), with the time windows and the p-values of the significant clusters indicated, with color bars to the left of topographical plots indicating the t-value. Electroencephalography (EEG) channels marked as green dots indicate significant clusters. The time course of the averaged signal of the electrodes comprising each significant cluster is displayed in the respective plot to the right. Black bar: time of stimulation (0 s) and the period of data exclusion contaminated by the stimulation artefact. Gray shaded area: significant time window of the cluster, indicated atop the respective plot. Purple: EEG response to REAL. Green: EEG response to SHAM-MS. Shaded areas correspond to ±1 standard error of the mean (SEM). X-axis: time in seconds (s). Y-axis: amplitude in µV. **Source:** taken from (Gassmann et al., 2022), figure and legend modified.

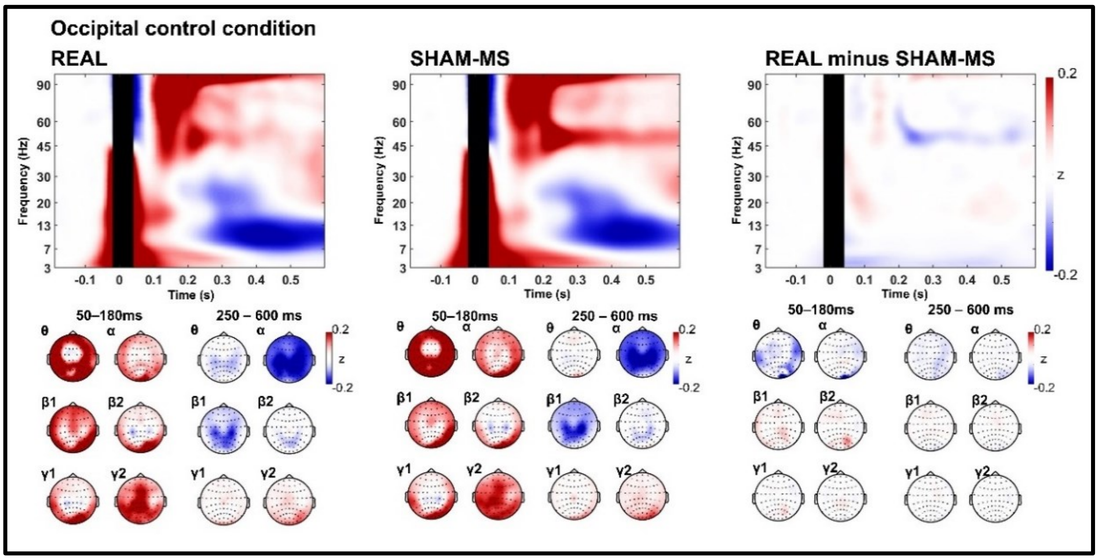

Figure 15: Occipital control condition: TMS-induced oscillations

Transcranial magnetic stimulation (TMS) induced oscillations in the occipital control condition from occipital TMS (left column), SHAM-MS (middle column) and the subtraction of SHAM-MS from REAL (right column). Occipital TMS was delivered over the electrode O2, which is situated atop the right occipital cortex. The time-frequency plots display the corresponding oscillatory responses, averaged across all channels and all subjects (n=23). The vertical black bars indicate time of stimulation (0 s) and the period of data exclusion contaminated by the stimulation artefact (-6 ms to +20 ms). X-axis: time in seconds (s). Y-axis: frequency in Hertz (Hz). Topographical plots represent the average power of the corresponding condition in the specified frequency bands and time windows, color represents z-transformed data, with red indicating increase and blue indicating decrease in power compared to baseline, as indicated by the color bars next to the respective plots. **Source:** taken from (Gassmann et al., 2022), figure and legend modified.

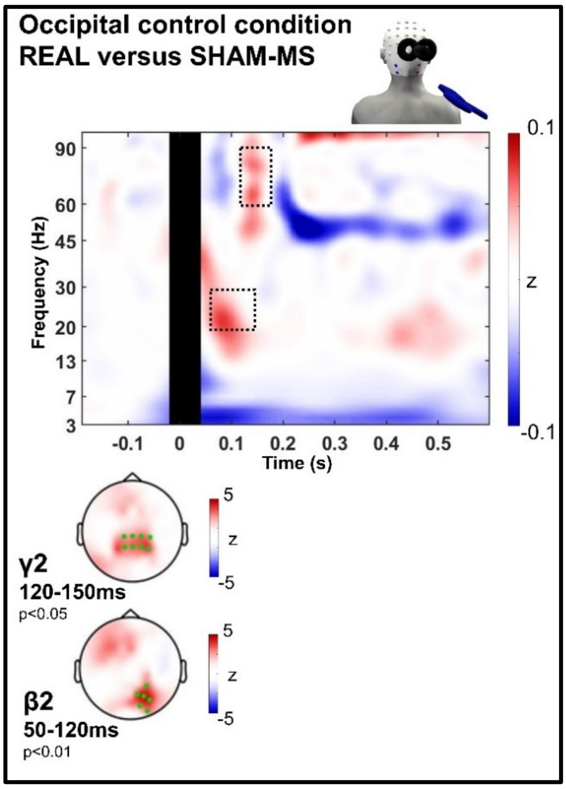

Figure 16: Occipital control condition: statistical comparison of TMS-induced oscillations from REAL and SHAM-MS

The time-frequency plots display the difference in the oscillatory response from the REAL involving occipital transcranial magnetic stimulation (TMS) and the SHAM-MS (REAL versus SHAM-MS), averaged across all channels and all subjects (n=23). Black bars indicate the time of stimulation (0 s) and the period of data exclusion contaminated by the stimulation artefact, and the dotted boxes represent the frequencies and time windows of significant clusters. X-axis: time in seconds (s). Y-axis: frequency in Hertz (Hz). Topographical plots represent the average power difference (REAL versus SHAM-MS) within the frequency and time windows of significant clusters. The frequency band, time window and p-value of each significant cluster are indicated next to the respective topographical plot. EEG channels marked as green dots indicate the significant clusters. On the right-hand side of each plot, the respective calibration bar is indicated, with the z-values being a normalization of the power spectral density. **Source:** taken from (Gassmann et al., 2022), figure and legend modified.

3.1.3.3 Cerebellar TMS with a downward induced current

When applying cbTMS with a downward induced current (see 2.1.8.3), several differences between REAL and SHAM-MS can be observed in the time courses and spatial distributions of the EEG signals (Figure 17) (Gassmann et al., 2022). REAL, involving cbTMS with a downward induced current, elicited an early positive deflection in electrodes over the left prefrontal cortex, followed by a negative deflection in electrodes over the left parietal cortex, which was not present in the SHAM-MS (Gassmann et al., 2022). Both SHAM-MS and REAL elicited a negative response in fronto-central electrodes peaking after ~100 ms, which was followed by a positive deflection in central electrodes after ~200 ms (Gassmann et al., 2022). When subtracting SHAM-MS from REAL following the saturation approach rationale (see 2.1.8.1), a left parietal negative deflection ~100 ms persisted, as well as a persistent negative cluster in electrodes over the left parietal cortex in late time windows (Gassmann et al., 2022).

The comparison of the TEPs elicited by REAL and SHAM-MS with a cluster-based permutation t-statistics (see 2.1.10.2) yielded several significant and relevant clusters (Figure 18) (Gassmann et al., 2022). A positive deflection from 20 to 26 ms after REAL was applied was observed in electrodes over the left prefrontal cortex with a mirrored negative deflection in right parietal electrodes (Gassmann et al., 2022). Furthermore, a negative deflection from 35 to 55 ms in electrodes over the left parietal cortex, mirrored by a positive deflection in right parietal electrodes was observed (Gassmann et al., 2022). In the time window beyond 60 ms post-TMS, a left parietal negative deflection 60-120 ms was found, as well as a persistent left parietal negativity in electrodes over the left parietal cortex (Gassmann et al., 2022).

After TFRs for REAL and SHAM-MS were calculated (see 2.1.10.3), SHAM-MS was subtracted from REAL (Gassmann et al., 2022). An early increase in low gamma and high gamma power, as well as a late decrease in alpha power was observed in both REAL and SHAM-MS data (Gassmann et al., 2022). When subtracting SHAM-MS from REAL, a broadband difference in power was found (Figure 19) (Gassmann et al., 2022).

When comparing TFRs elicited by REAL and SHAM-MS with a cluster-based permutation t-statistics (see 2.1.10.4), several significant and relevant differences were observed (Figure 20) (Gassmann et al., 2022). An increase in theta power in frontal and occipital electrodes was observed from 50-230 ms post-cbTMS (Gassmann et al., 2022). Also, an increase in high beta power in left prefrontal regions and right occipital regions ranging from 50-190 ms and an increase in low and high gamma in electrodes over posterior and frontal regions 50-190 ms and 50-250 ms post-cbTMS were found (Gassmann et al., 2022). Lastly, a decrease in alpha power in posterior regions 490-550 ms after REAL was delivered was observed (Gassmann et al., 2022).

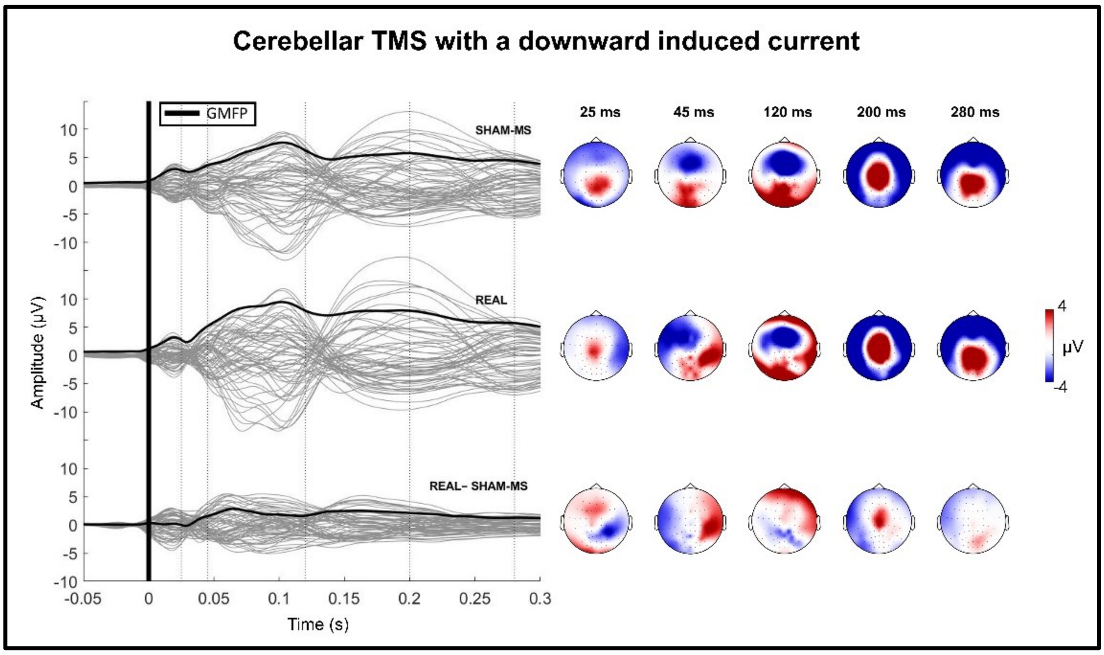

Figure 17: cbTMS with a downward induced current: time courses and spatial distributions of the EEG signals

Butterfly plots (left) display the time course of the electroencephalography (EEG) responses following SHAM-MS (top) and REAL (middle), and the subtraction of SHAM-MS from REAL (bottom: REAL minus SHAM-MS), averaged across all subjects (n=23). Each gray line corresponds to the signal from one EEG channel. The black line corresponds to the Global Mean Field Potential (GMFP). The vertical black bar indicates the time of stimulation (0 s) and the period of data exclusion contaminated by the stimulation artefact. X-axis: time in seconds (s). Y-axis: amplitude in µV. Dotted lines represent the time-points that are displayed in the topographical plots (right). Colors in the topographical plots indicate voltage in µV, as shown in the calibration bars. **Source:** taken from (Gassmann et al., 2022), figure and legend modified.

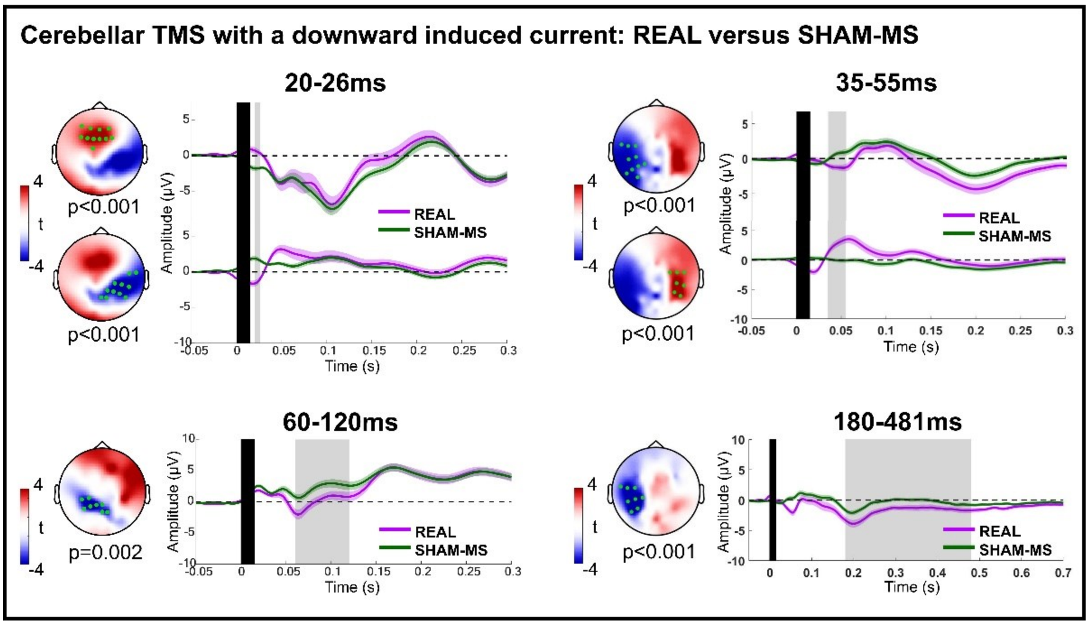

Figure 18: cbTMS with a downward induced current: statistical comparison of TMS-evoked EEG responses from REAL and SHAM-MS

Topographical plots represent results from the cluster-based t-statistics (REAL versus SHAM-MS), with the time windows and the p-values of the significant clusters indicated. Electroencephalography (EEG) channels marked as green dots indicate significant clusters. The time course of the averaged signal of the electrodes comprising each significant cluster is displayed in the respective plot to the right. Black bar: time of stimulation (0 s) and the period of data exclusion contaminated by the stimulation artefact. Gray shaded area: significant time window of the cluster, indicated atop the respective plot. Purple: REAL. Green: SHAM-MS. Shaded areas correspond to ±1 standard error of the mean (SEM). X-axis: time in seconds (s). Y-axis: amplitude in µV. **Source:** taken from (Gassmann et al., 2022), figure and legend modified.

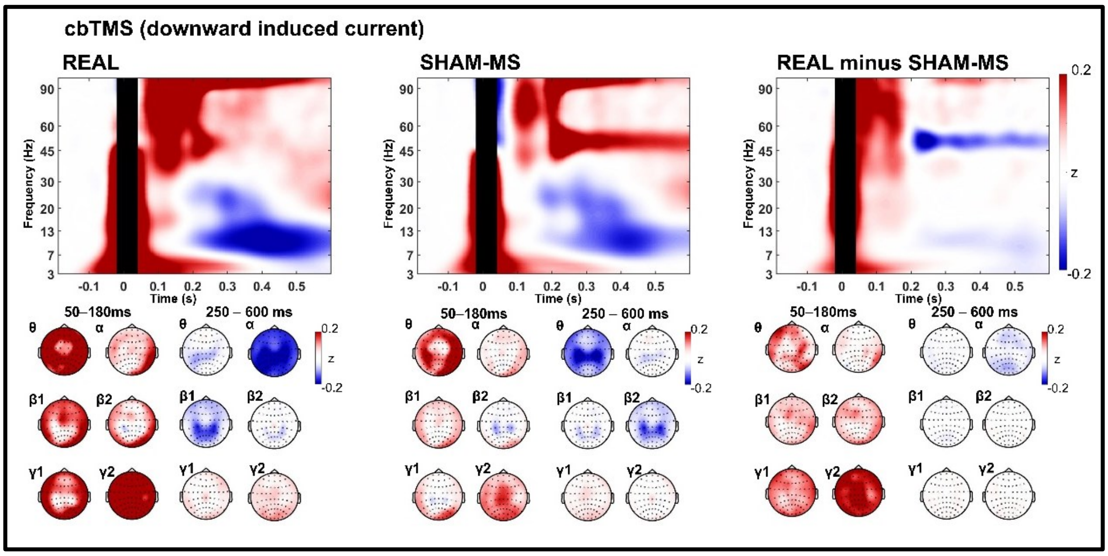

Figure 19: cbTMS with a downward induced current: TMS-induced oscillations

Transcranial magnetic stimulation (TMS) induced oscillations in electroencephalography (EEG) from REAL (left column), SHAM-MS (middle column) and the subtraction of SHAM-MS from REAL (right column). The figure displays the control condition involving cerebellar TMS (cbTMS) with a downward induced current in the right cerebellar cortex. The time-frequency plots display the corresponding oscillatory responses, averaged across all channels and all subjects (n=23). The vertical black bars indicate time of stimulation (0 s) and the period of data exclusion contaminated by the stimulation artefact. X-axis: time in seconds (s). Y-axis: frequency in Hertz (Hz). Topographical plots represent the average power of the corresponding condition in the specified frequency bands and time windows, color represents z-transformed data, with red indicating increase and blue indicating decrease in power compared to baseline. **Source:** taken from (Gassmann et al., 2022), figure and legend modified.

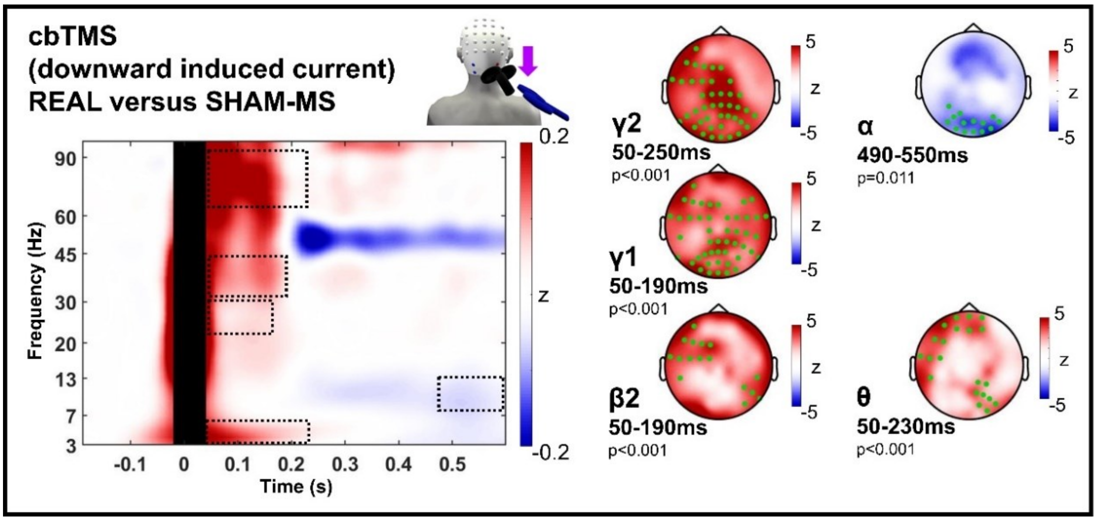

Figure 20: cbTMS with a downward induced current: statistical comparison of TMS-induced oscillations from REAL and SHAM-MS

The time-frequency plots display the difference in the oscillatory response from the REAL and SHAM-MS conditions (REAL versus SHAM-MS), averaged across all channels and all subjects (n=23). Black bars indicate the time of stimulation (0 s) and the period of data exclusion contaminated by the stimulation artefact, and the dotted boxes represent the frequencies and time windows of significant clusters. Topographical plots represent the average power difference (REAL versus SHAM-MS) within the frequency and time windows of significant clusters. The frequency band, time window and p-value of each significant cluster are indicated next to the respective topographical plot. Electroencephalography (EEG) channels marked as green dots indicate the significant clusters. On the right-hand side of each plot, the respective calibration bar is indicated, with the z-values being a normalization of the power spectral density. X-axis: time in seconds (s). Y-axis: frequency in Hertz (Hz). **Source:** taken from (Gassmann et al., 2022), figure and legend modified.

3.1.4 Cerebellar TMS with an upward induced current

When delivering cbTMS with an upward induced current (see 2.1.9), differences between REAL and SHAM-MS could be observed (Gassmann et al., 2022). REAL, involving cbTMS with an upward induced current, elicited a positive deflection in the left-hemispheric prefrontal electrodes, peaking after ~25 ms (Gassmann et al., 2022). Moreover, a left-hemispheric negative deflection peaking ~45 ms was observed (Gassmann et al., 2022). These deflections were not present in the SHAM-MS (Gassmann et al., 2022). Both SHAM-MS and REAL elicited a large negative potential in fronto-central electrodes at ~100 ms, the N100, and a positive midline potential at ~200 ms (Gassmann et al., 2022). Subtraction of SHAM-MS from REAL, following the saturation approach (see 1.5.1), revealed a negative, left-hemispheric potential in parietal electrodes ~100 ms post-TMS (Gassmann et al., 2022). The early potentials observed in the time window <60 ms post-TMS persisted after subtraction of SHAM-MS (Gassmann et al., 2022). Notably, these findings were reproducible across experiments #1 and #2 (Figure 21) (Gassmann et al., 2022).

Comparing TEPs elicited by REAL and SHAM-MS with a cluster-based permutation t-statistics (see 2.1.10.2), significant and relevant clusters were observed in experiment #1 and reproduced in experiment #2 (Figure 22) (Gassmann et al., 2022). A positive left prefrontal cluster peaking ~25 ms post-TMS, as well as a negative cluster in electrodes over the left fronto-parietal cortex peaking ~45 ms post-TMS were observed (Figure 22), which were not observed in EEG responses to control conditions (see 3.1.3) (Gassmann et al., 2022). In the same time window of the N45, from 35 to 55 ms, a positive cluster in electrodes over the right occipital cortex was found (Figure 22), bearing resemblance to the early cluster when applying the occipital control condition (Figure 14) (Gassmann et al., 2022). Even though both SHAM-MS and REAL elicited a high-amplitude N100 response (Figure 22), a cluster was determined 100 ms post-TMS, as the spatial distribution of the N100 was different between REAL and SHAM-MS (Gassmann et al., 2022). This potential was observed in left parietal electrodes, while SHAM-MS elicited a midline potential (Figure 22) (Gassmann et al., 2022). A persistent positive cluster in electrodes over the right occipital cortex was observed in experiment #1, from 180 ms to 320 ms in experiment #1, which was also observed in experiment #2 from 180 ms to 480 ms, bearing resemblance to the late cluster when applying the occipital control condition (Figure 14) (Gassmann et al., 2022). These clusters were mirrored by a long-lasting negative cluster in electrodes over the left parietal cortex in the same time window (Gassmann et al., 2022). Significant clusters observed in experiment #1 were reproduced in experiment #2 (Figure 22) (Gassmann et al., 2022).

When directly comparing the typical fronto-central N100 response after SHAM-MS was subtracted between conditions involving cbTMS with an upward induced current and the control conditions, no difference was observed – after SHAM-MS subtraction, the mean amplitude was ~0 μV in all applied conditions (Figure 23A). However, when selecting the electrodes of the negative cluster in left parietal electrodes ~100 ms post-TMS in conditions involving cbTMS with an upward induced current (Figure 23), a significant difference ($p<0.01$) is observed between conditions involving cbTMS with an upward induced current and the occipital control condition.

After the calculation of the TFRs (see 2.1.10.3) elicited by REAL and SHAM-MS, SHAM-MS was subtracted from REAL (Gassmann et al., 2022). Both REAL and SHAM-MS elicited an early increase in theta power, and a late decrease in alpha power, however, both stronger in the REAL (Gassmann et al., 2022). The REAL condition elicited an early increase in theta, high beta, low and high gamma power, which was not observed in the SHAM-MS (Figure 24) (Gassmann et al., 2022).

Utilizing a cluster-based permutation t-statistics (see 2.1.10.4) to compare the TFRs elicited by SHAM-MS and REAL, multiple significant differences were determined, with results being reproduced across experiments #1 and #2 (Figure 25) (Gassmann et al., 2022). In early time windows, a cluster showing an increase in theta power in the frontal and occipital regions was observed (Gassmann et al., 2022). Furthermore, an increase in high beta power in left prefrontal regions and right occipital regions and increased low and high gamma in frontal and posterior regions were found (Gassmann et al., 2022). Moreover, a cluster showing a late decrease in alpha power in posterior regions was observed (Figure 25) (Gassmann et al., 2022).

Analysis of amplitude distributions (see 2.1.10.4) yielded that cb-P25, cb-N45, and the SHAM-MS EEG responses were normally distributed (Figure 26) (Gassmann et al., 2022). The expected values of the distributions of SHAM-MS responses were close to 0 μV (Gassmann et al., 2022). Hence, for the cb-P25 and cb-N45, amplitude distributions and expected values were not altered substantially by the subtraction of SHAM-MS (Gassmann et al., 2022).

When calculating the cb-P25 and cb-N45 cluster amplitudes per subject and experiment, they were observed to be reproducible and were present in a majority of subjects (Figure 27) (Gassmann et al., 2022).

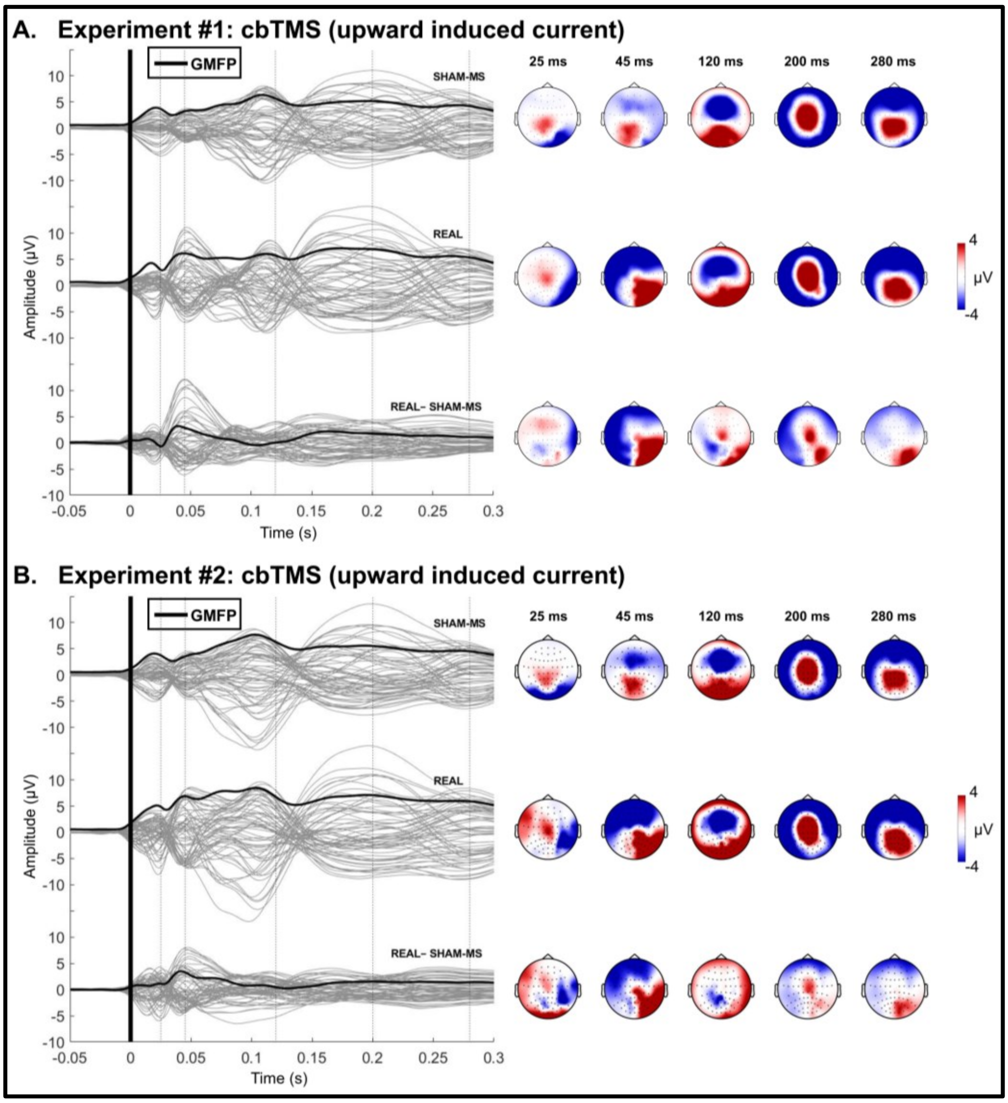

Figure 21: Display of time course and spatial distribution of the EEG signals elicited by cbTMS with an upward induced current

Divided in experiment #1 (**A.**) and experiment #2 (**B.**). Butterfly plots (left) display the time course of the electroencephalography (EEG) responses following the SHAM-MS (top) and the REAL condition (middle), and the subtraction of SHAM-MS from REAL, averaged across all subjects (each n=23) in experiment #1 and #2. Each gray line corresponds to the signal from one EEG channel. The black line corresponds to the Global Mean Field Potential (GMFP). The vertical black bar represents the time of stimulation (0 s) and the period of data exclusion contaminated by the stimulation artefact. X-axis: time in seconds (s). Y-axis: amplitude in µV. Dotted lines represent the time-points that are displayed in the topographical plots (right). Colors in the topographical plots indicate voltage in µV, as shown in the calibration bars to the right. **Source:** taken from (Gassmann et al., 2022), figure and legend modified.

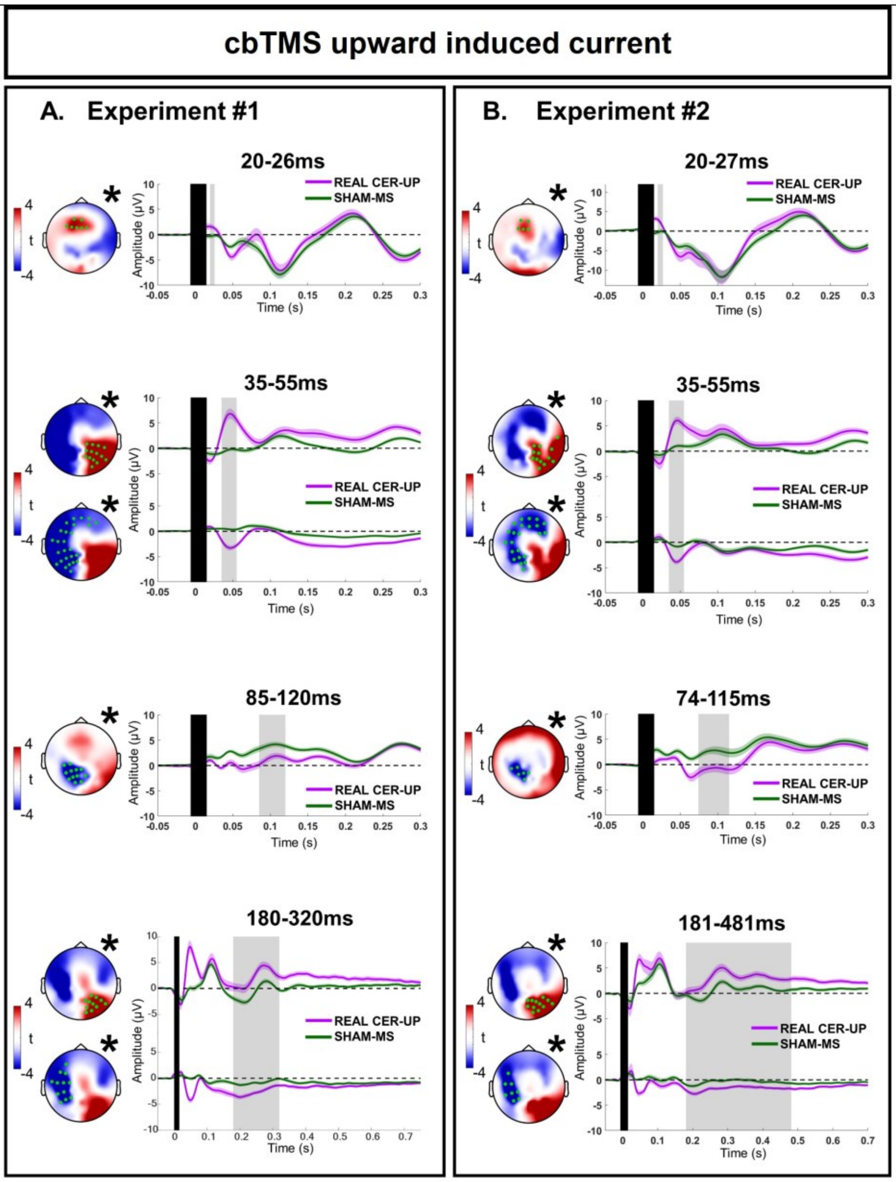

Figure 22: Comparison of TMS-EEG responses from cbTMS with an upward induced current and the sham procedure

Comparison of electroencephalography (EEG) responses from cerebellar TMS (cbTMS) with an upward induced current and the sham procedure (SHAM-MS) in experiment #1 (A.) and experiment #2 (B.). Topographical plots represent results from the cluster-based t-statistics (REAL versus SHAM-MS), with time windows of the significant clusters. Asterisks indicate $p<0.001$. EEG channels marked as green dots indicate significant clusters. The time courses of the averaged signal from the channels comprising each significant cluster are displayed in the respective plot to the right. Black bar: time of stimulation (0 s) and the period of data exclusion contaminated by the stimulation artefact. Gray shaded area: significant time window of the cluster. Purple: REAL. Green: SHAM-MS. Shaded areas correspond to ±1 standard error of the mean (SEM). X-axis: time in seconds (s). Y-axis: amplitude in µV. **Source:** taken from (Gassmann et al., 2022), figure and legend modified.

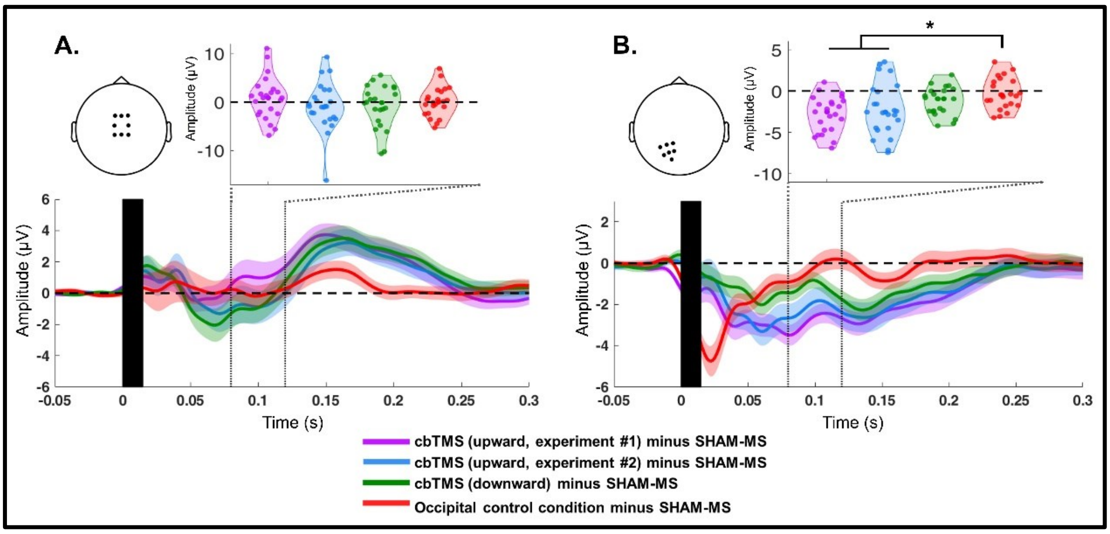

Figure 23: Direct comparison of the N100 cluster elicited by cbTMS with an upward induced current with control conditions

Top row: Selected electrodes marked with black dots on the topographical plot. Violin plots show the electroencephalography (EEG) signal amplitude in the time-window of the N100 cluster (80-120 ms after cerebellar transcranial magnetic stimulation (cbTMS)). Each violin represents one condition, with each dot inside each violin being the average amplitude of the cluster (n=23). Asterisks indicate a significant difference ($p<0.01$). Y-axis: Amplitude in μV. X-axis: Conditions. **Bottom row**: Average time-course of the EEG response to the respective condition. Black bar marks the TMS pulse (0s). Shaded areas represent ±1 standard error of the mean (SEM). SHAM-MS: sham control condition. Y-axis: Amplitude in μV. X-axis: Time in seconds (s).

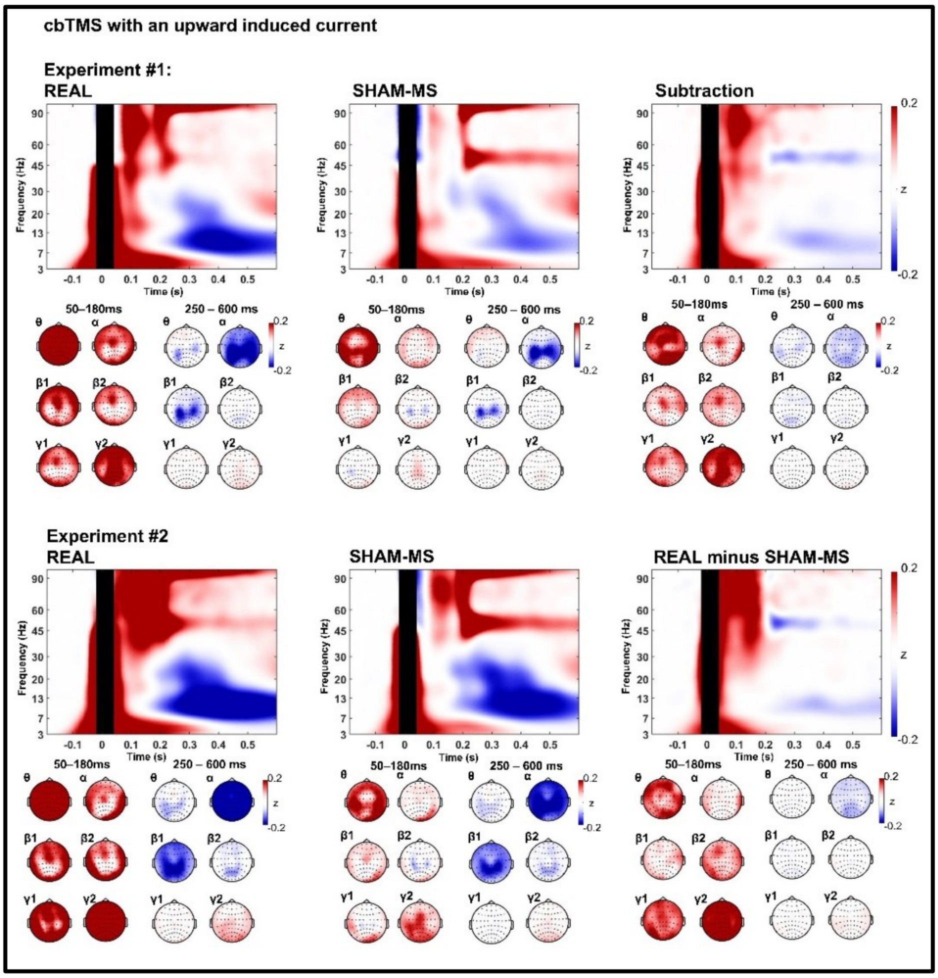

Figure 24: TMS-EEG induced oscillations in the cbTMS condition with an upward induced current

Electroencephalography (EEG) induced oscillations from REAL (left column), SHAM-MS (middle column) and the subtraction of SHAM-MS from REAL (right column). The figure is divided into experiment #1 (top) and experiment #2 (bottom). The time-frequency plots display the corresponding oscillatory responses, averaged across all channels and all subjects (n=23). The vertical black bars indicate the time of stimulation (0 s) and the period of data exclusion contaminated by the stimulation artefact. X-axis: time in seconds (s). Y-axis: frequency in Hertz (Hz). Topographical plots represent the average power of the corresponding condition in the specified frequency bands and time windows, color represents z-transformed data, with red indicating increase and blue indicating decrease in power compared to baseline, as indicated in the color bars next to the respective plots. **Source:** taken from (Gassmann et al., 2022), figure and legend modified.

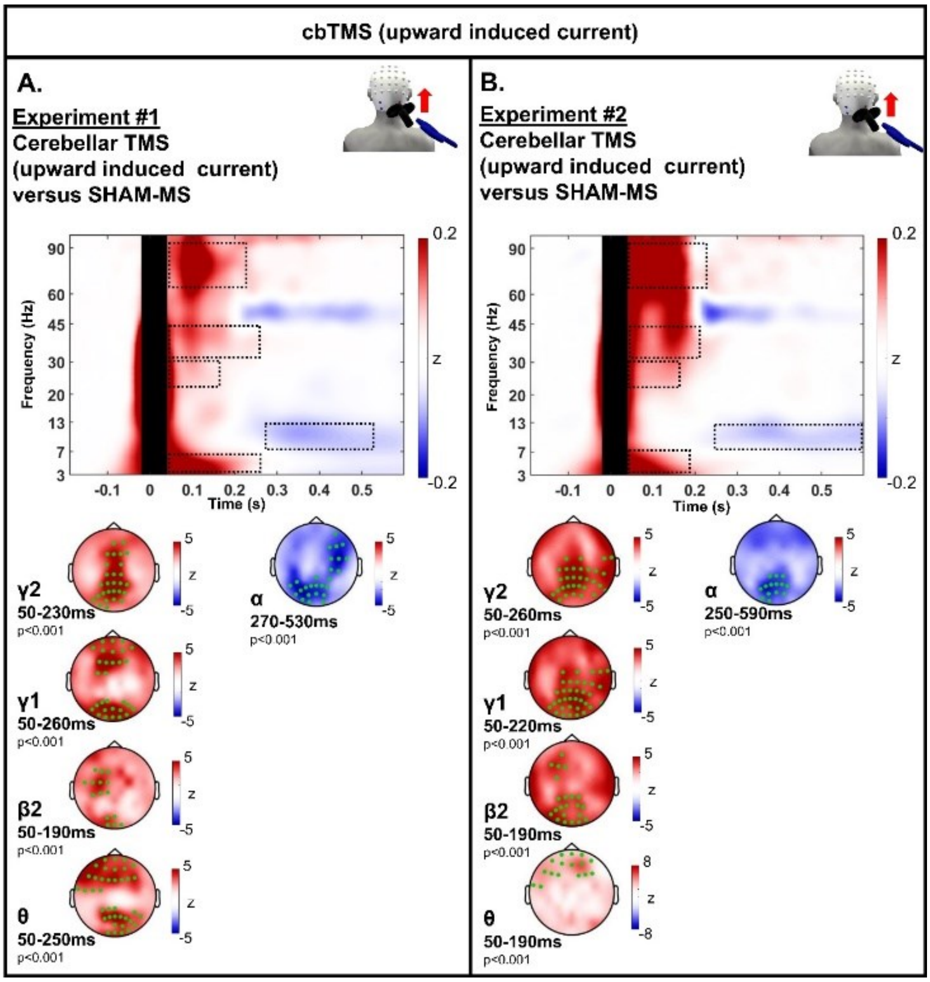

Figure 25: Comparison of TMS-EEG induced oscillations in the REAL minus SHAM-MS conditions

A. Cerebellar transcranial magnetic stimulation (cbTMS) with an upward induced current in experiment #1. **B.** cbTMS with an upward induced current in experiment #2. The time-frequency plots display the difference in the oscillatory response from the REAL and SHAM-MS conditions (REAL versus SHAM-MS), averaged across all channels and all subjects. Black bars indicate the time of stimulation (0 s) and the period of data exclusion contaminated by the stimulation artefact, and the dotted boxes represent the frequencies and time windows of significant clusters. Topographical plots represent the average power difference (REAL versus SHAM-MS) within the frequency and time windows of significant clusters. The frequency band, time window and p-value of each significant cluster are indicated next to the respective topographical plot. Electroencephalography (EEG) channels marked as green dots indicate the significant clusters. On the right-hand side of each plot, the respective calibration bar is indicated, with the z-values being a normalization of the power spectral density. X-axis: Time in seconds (s). Y-axis: Frequency in Hertz (Hz). **Source:** taken from (Gassmann et al., 2022), legend and figure modified.

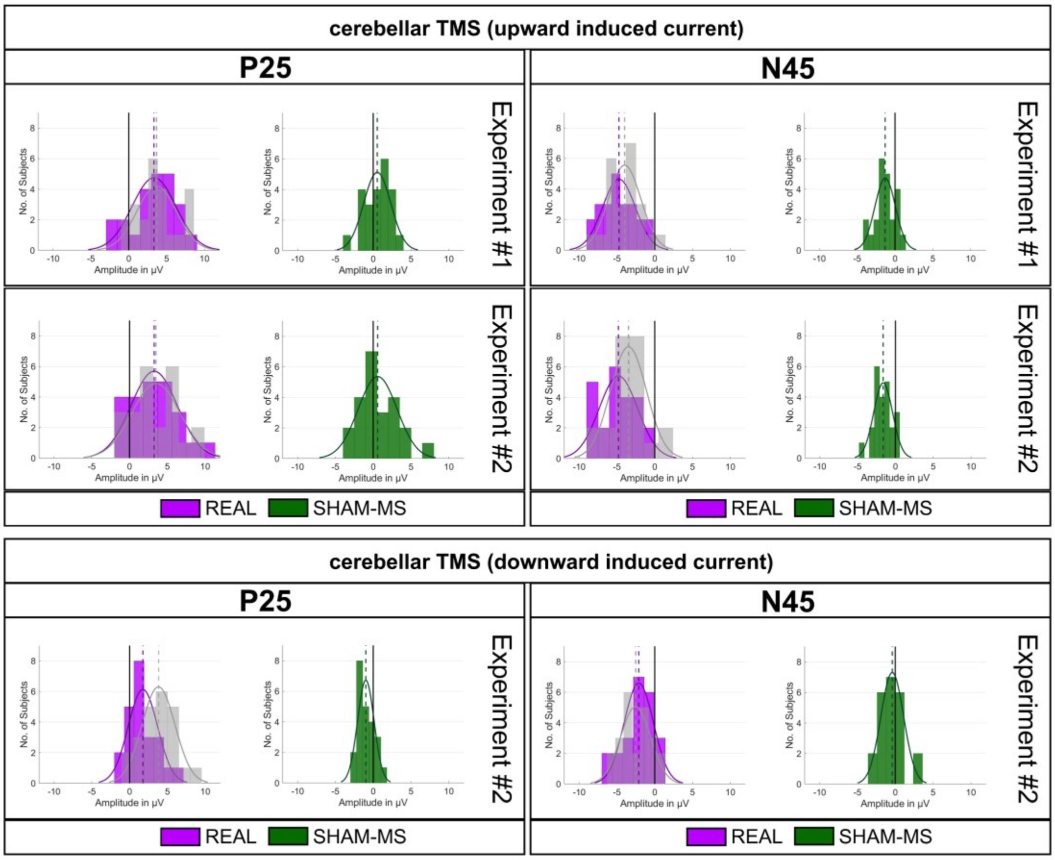

Figure 26: Amplitude distributions of P25 and N45 EEG responses in conditions involving cbTMS

Histograms illustrating the amplitude distributions of the cb-P25 (left) and cb-N45 (right) potentials of the conditions involving cerebellar transcranial magnetic stimulation (cbTMS) with an upward induced (top) and downward induced current (bottom) in experiment #1 (n=23) and experiment #2 (n=23). For each condition, the respective SHAM-MS (green), REAL (purple) and REAL minus SHAM-MS (grey) distributions are shown. The fitted Gaussian distributions are shown in the respective color, the dotted vertical lines mark the expected value of the respective distribution. The black vertical lines mark 0 μV. **X-axis:** amplitude in μV. **Y-axis:** number of subjects per bin. **Source:** taken from (Gassmann et al., 2022), figure and legend modified.

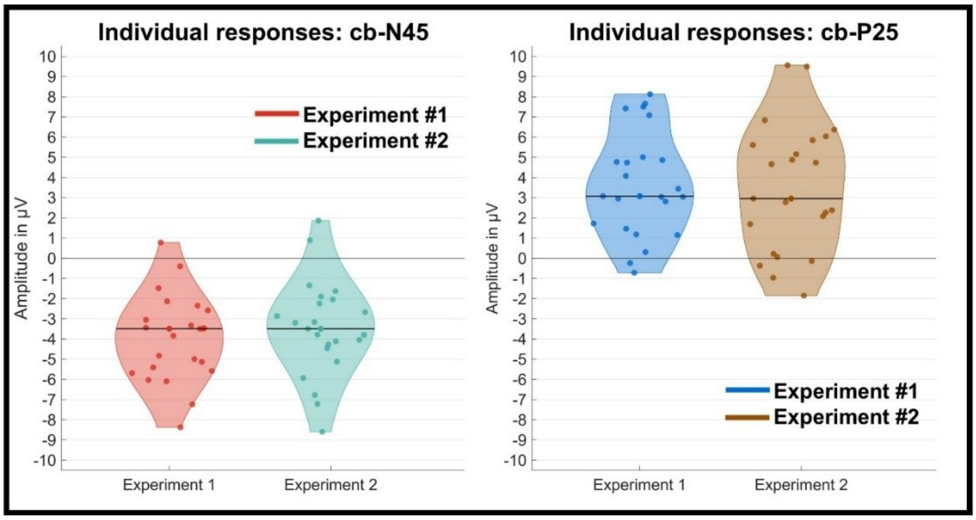

Figure 27: Individual cb-P25 and cb-N45 cluster values

The individual cb-N45 (left) and cb-P25 (right) electroencephalography (EEG) responses are displayed as violin plots. Each dot represents one individual value. The horizontal black line in each violin plot marks the group mean value. **X-axis:** experiment number. **Y-axis:** amplitude in µV. **Source:** taken from (Gassmann et al., 2022), legend modified.

3.1.5 Source analysis

The projection of EEG responses from statistically significant TEP clusters into the source space (see 2.1.10.6) yielded several results. As a generic head model was utilized, results will be described with on the level of accuracy of regions of the brain, not individual gyri.

When projecting the TEP clusters of the condition involving cbTMS with an upward induced current (Figure 22) into the source space (Figure 28, Figure 29), some results were unique to the REAL. Namely, the cb-P25 was projected onto the left prefrontal cortex, contralateral to cbTMS. The cb-N45 was projected onto left prefrontal and left temporo-parietal areas (Figure 29).

For both SHAM-MS and REAL, the N100 projected onto fronto-central areas, however, in the REAL there was an additional projection onto posterior parietal areas. Furthermore, both SHAM-MS and REAL showed a large positive deflection projecting onto fronto-central areas. However, in the REAL, there is an additional projection onto left parietal areas and right occipital areas (Figure 29).

The projection of the TEP clusters observed in the occipital control condition (Figure 14) yielded several results. The early positive cluster 20 to 45 ms after REAL was delivered projected onto right occipital areas, the negative cluster in the same time window onto left occipital areas. The late positive cluster from 200-480 ms projected onto right occipital areas (Figure 30).

For the TEP clusters observed when delivering cbTMS with a downward induced current (Figure 18), the cb-P25 cluster projects more lateral than when delivering cbTMS with an upward induced current (Figure 31). Otherwise, results observed in the condition involving cbTMS with an upward induced current were reproduced (Figure 28).

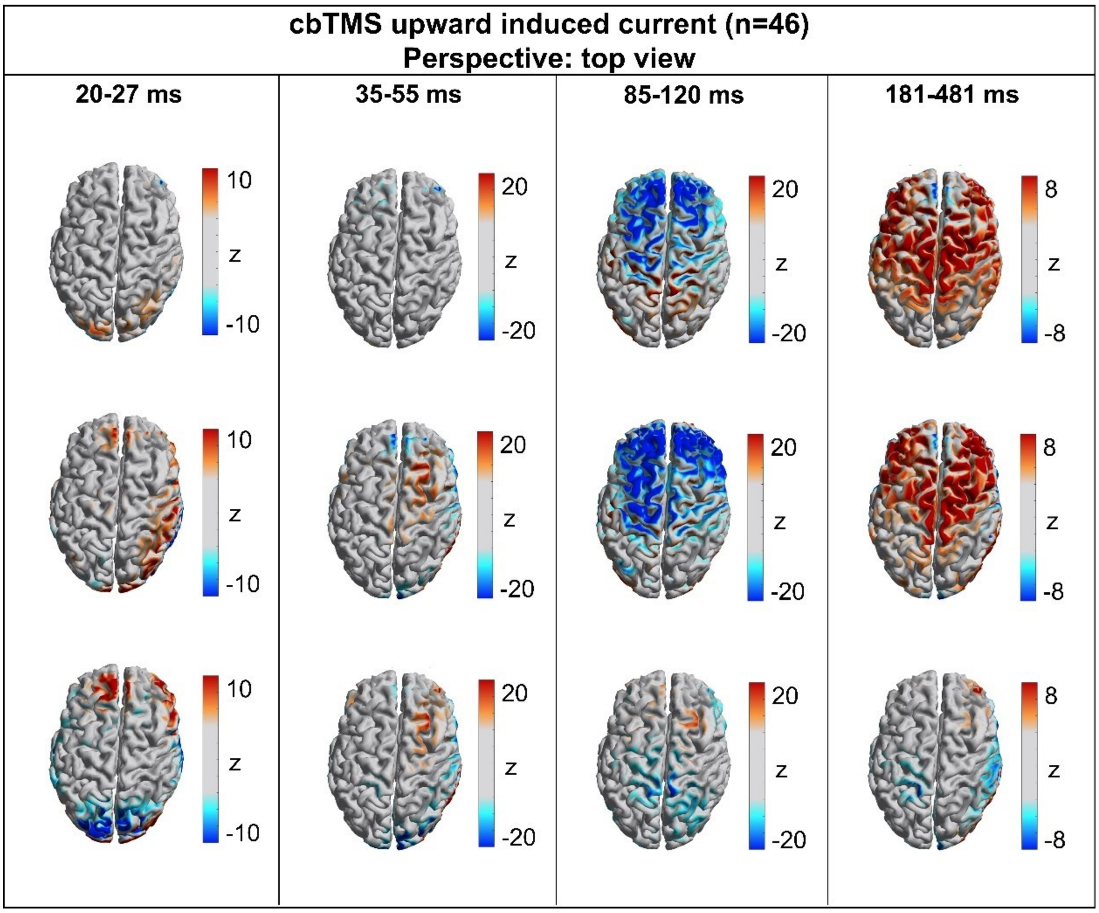

Figure 28: cbTMS upward induced current: source estimation of the EEG responses - top view

Top row: projection of electroencephalography (EEG) responses evoked by SHAM-MS. **Middle row:** projection of EEG responses elicited by the REAL condition involving cerebellar transcranial magnetic stimulation (cbTMS) with an upward induced current. **Bottom row:** projection of REAL minus SHAM-MS EEG responses. Each column displays one of the statistically significant clusters (Figure 22). Color bars to the right of the plots display the scaling of the z-values. The time window of the projected cluster is displayed on top of each column. **Source:** taken from (Gassmann et al., 2022), figure and legend modified.

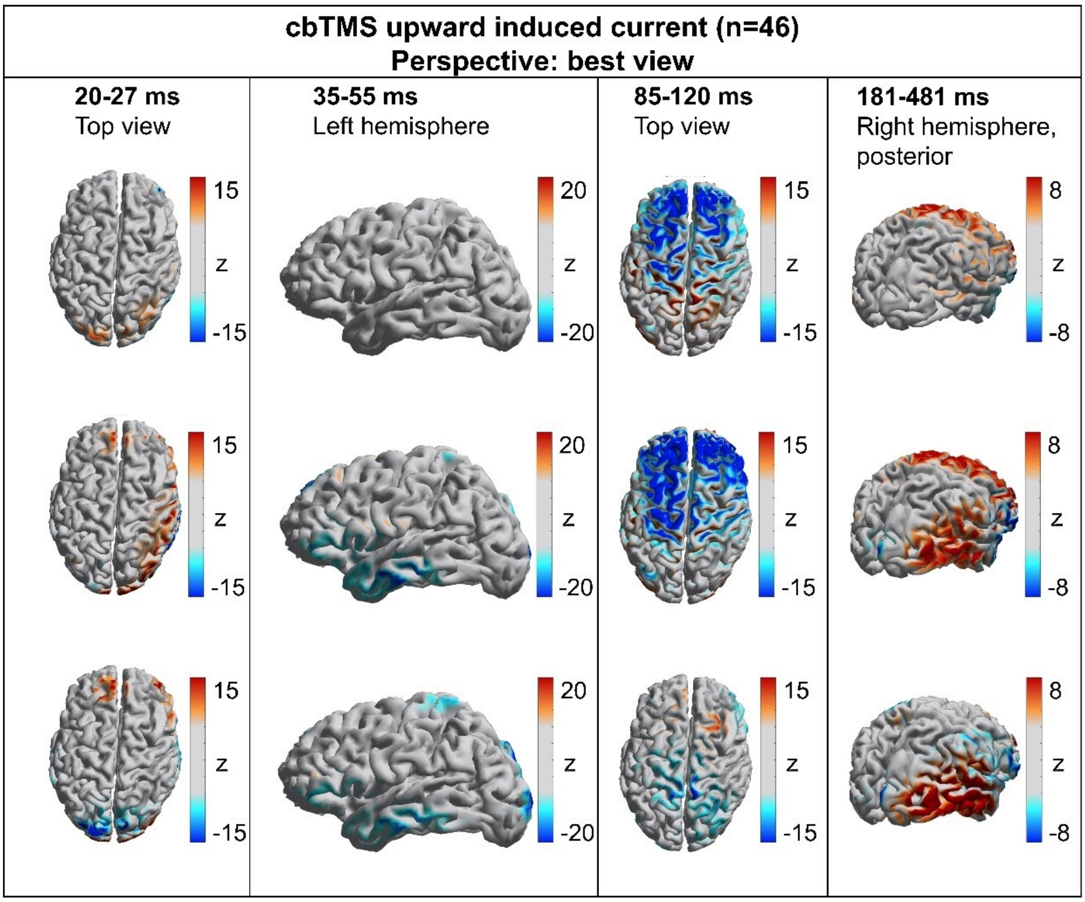

Figure 29: cbTMS upward induced current: source estimation of the EEG responses - best view

Best view means the 3-dimensional source plot was rotated to view the regions deemed most relevant. **Top row:** projection of electroencephalography (EEG) responses elicited by SHAM-MS. **Middle row:** projection of EEG responses evoked by the REAL condition involving cerebellar transcranial magnetic stimulation (cbTMS) with an upwards induced current. **Bottom row:** projection of REAL minus SHAM-MS EEG responses. Each column displays one of the statistically significant clusters (Figure 22). Color bars to the right of the plots display the scaling of the z-values. The time window of the projected cluster is displayed on top of each column. **Source:** taken from (Gassmann et al., 2022), legend and figure modified.

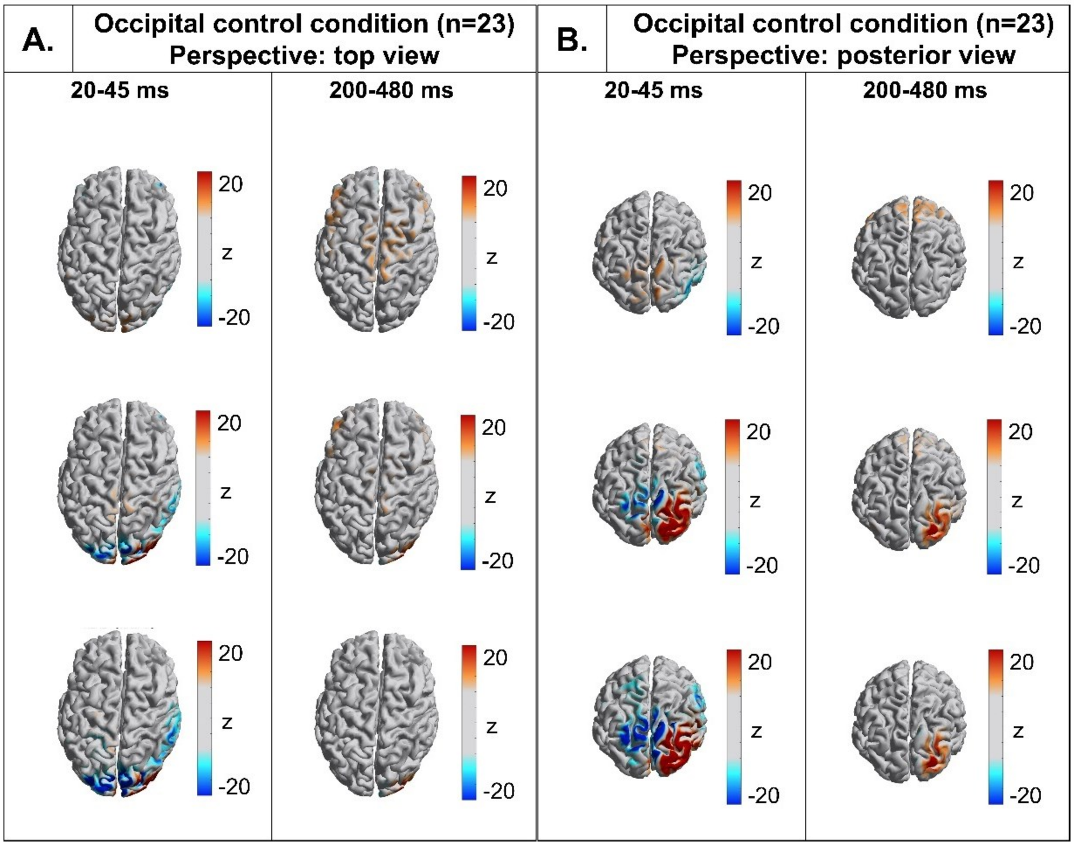

Figure 30: Occipital control condition: source estimation of the EEG responses

Top row: projection of electroencephalography (EEG) responses evoked by SHAM-MS. **Middle row:** projection of EEG responses elicited by the REAL condition involving occipital transcranial magnetic stimulation (TMS). **Bottom row:** projection of REAL minus SHAM-MS EEG responses. Each column displays one of the statistically significant clusters (Figure 14). Color bars to the right of the plots display the scaling of the z-values. **A.** Top view. The time window of the projected cluster is displayed on top of each column. **B.** Posterior view. **Source:** taken from (Gassmann et al., 2022), figure and legend modified.

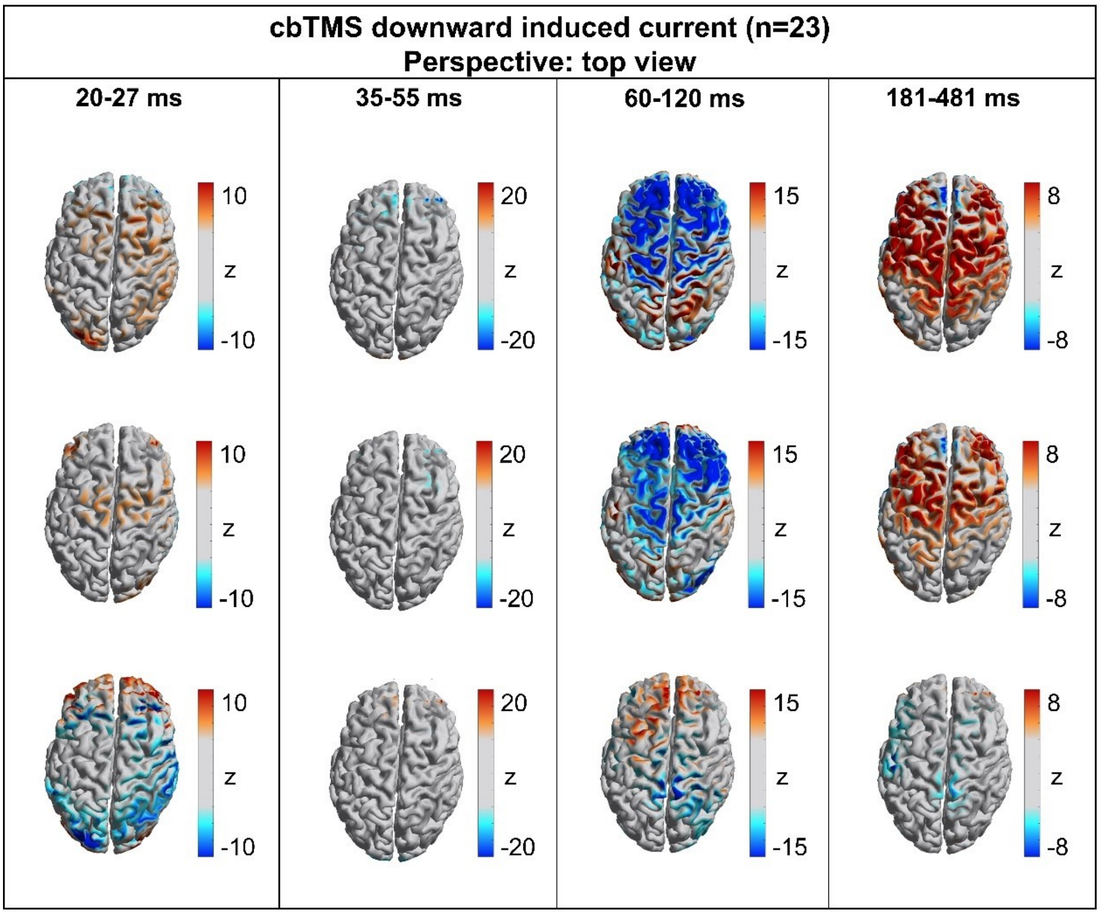

Figure 31: cbTMS downward induced current: source estimation of the EEG response - top view

Top row: projection of electroencephalography (EEG) responses evoked by SHAM-MS. **Middle row:** projection of EEG responses elicited by the REAL condition involving cerebellar transcranial magnetic stimulation (cbTMS) with a downward induced current. **Bottom row:** projection of REAL minus SHAM-MS EEG responses. Each column displays one of the statistically significant clusters (Figure 18). Color bars to the right of the plots display the scaling of the z-values. The time window of the projected cluster is displayed on top of each column. **Source:** taken from (Gassmann et al., 2022), figure and legend modified.

3.1.6 Correlation analysis

After a correction for multiple tests was applied utilizing the Bonferroni method (Bonferroni, 1936), adjusting the significance threshold to $p<0.002272$, the correlation analyses showed no linear correlations of significance (Figures 32-35) (Gassmann et al., 2022).

Correlation testing was conducted between CBI and TEP cluster amplitudes (Figure 32), between cbTMS intensity and TEP cluster amplitudes (Figure 33), between CBI with cbTMS induced power changes (Figure 34) and cbTMS intensity with cbTMS induced power changes (Figure 35) (Gassmann et al., 2022).

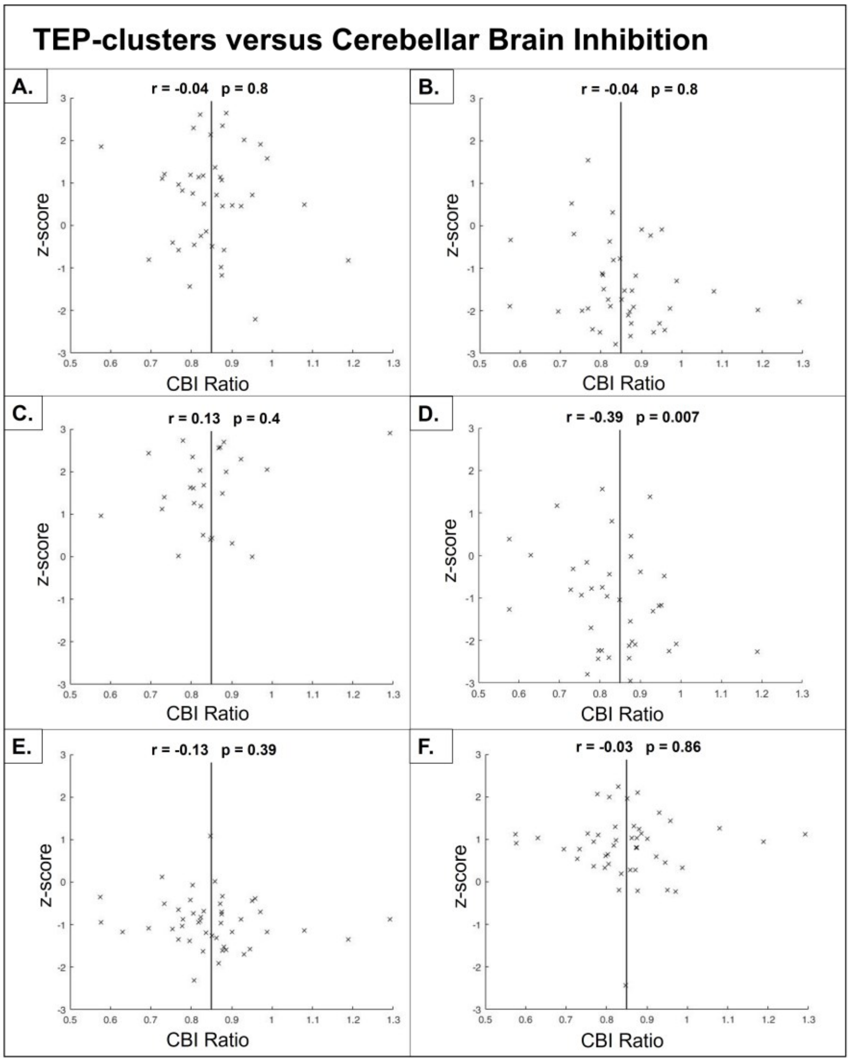

Figure 32: Scatterplot derived from Pearson correlation testing of TEP-clusters versus CBI values

For the depicted correlation analyses, the electroencephalography (EEG) clusters observed in the resting state between REAL involving cerebellar transcranial magnetic stimulation (cbTMS) with an upward induced current versus SHAM-MS were utilized (Figure 23). The resulting z-values of the TMS-evoked potential (TEP) clusters were tested for a linear correlation (Pearson) with the cerebellar brain inhibition (CBI) ratios of the subjects (n=46). The results of the correlation tests are displayed on the top of the respective plot. Each black cross represents one subject. The CBI ratio of 0.85 has been marked with a vertical black line. X-axis: CBI ratio. Y-axis: z-score. r: Pearson correlation coefficient. p: p-value with adjusted significance threshold to $p<0.002272$ to control for multiple tests. **A.** Positive cluster from 20-27ms. **B.** Negative cluster from 35-55 ms. **C.** Positive cluster from 35-55 ms. **D.** Negative cluster from 85-120 ms. **E.** Negative cluster from 180-481 ms. **F.** Positive cluster from 180-481 ms.

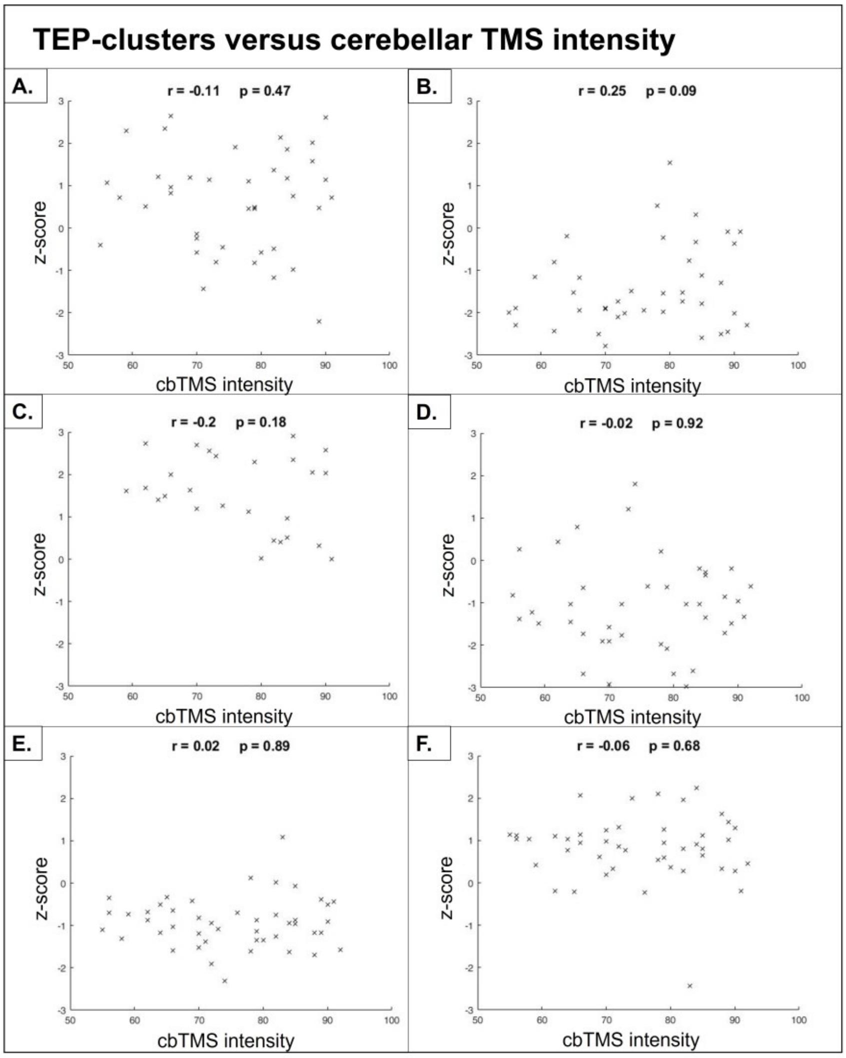

Figure 33: Scatterplot derived from Pearson correlation testing of TEP-clusters versus cbTMS intensity

For the depicted correlation analyses, the electroencephalography (EEG) clusters observed in the resting state between REAL involving cerebellar transcranial magnetic stimulation (cbTMS) with an upward induced current versus SHAM-MS were utilized (Figure 23). The resulting z-values of the TMS-evoked potential (TEP) clusters for each subject (n=46) were tested for a linear correlation (Pearson) with the cbTMS intensity values in percent of maximum stimulator output (%MSO). The results of the correlation test are displayed on the top of the respective plot. Each black cross represents one subject. X-axis: cbTMS intensity in %MSO. Y-axis: z-score of the respective cluster. r: Pearson correlation coefficient. p: p-value with adjusted significance threshold to $p<0.002272$ to control for multiple tests. **A.** Positive cluster from 20-27ms. **B.** Negative cluster from 35-55 ms. **C.** Positive cluster from 35-55 ms. **D.** Negative cluster from 85-120 ms. **E.** Negative cluster from 180-481 ms. **F.** Positive cluster from 180-481 ms.

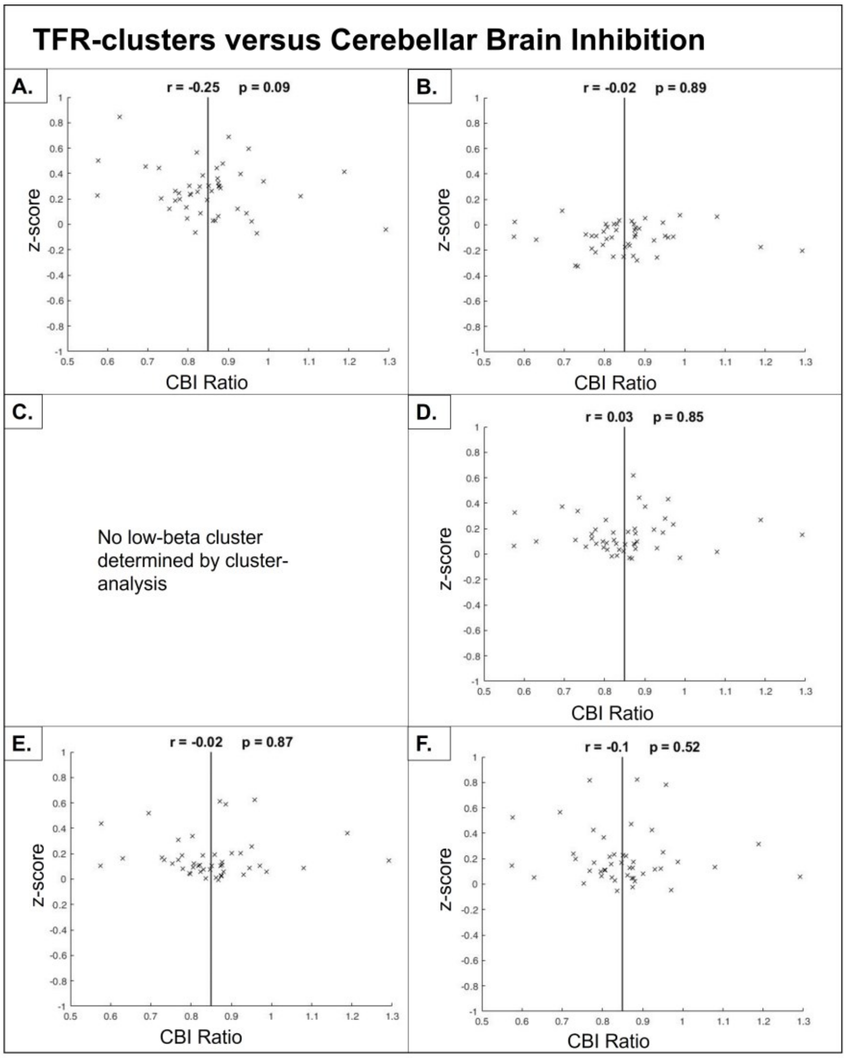

Figure 34: Scatterplot derived from Pearson correlation testing of TFR-clusters versus CBI values

For the depicted correlation analyses, the time-frequency response (TFR) clusters observed in the resting state between REAL involving cerebellar transcranial magnetic stimulation (cbTMS) with an upward induced current versus SHAM-MS were utilized (Figure 26). The resulting z-values of the TFR clusters were tested for a linear correlation (Pearson) with the cerebellar brain inhibition (CBI) values (n=46). The results of the correlation test are displayed on the top of the respective plot. The CBI ratio of 0.85 has been marked with a vertical black line. Each black cross represents one subject. X-axis: CBI ratio. Y-axis: z-score of the respective cluster. r: Pearson correlation coefficient. p: p-value with adjusted significance threshold to $p<0.002272$ to control for multiple tests. **A.** Theta (4-7Hz) from 50 to 290 ms. **B.** Alpha (8-12Hz) from 270 to 590 ms. **C.** Low beta (13-20 Hz): no significant cluster was determined in this frequency band. **D.** High beta (21-29 Hz) from 50 to 190 ms. **E.** Low gamma (30-40 Hz) from 50 to 200 ms. **F.** High gamma (60-90 Hz) from 50 to 250 ms.

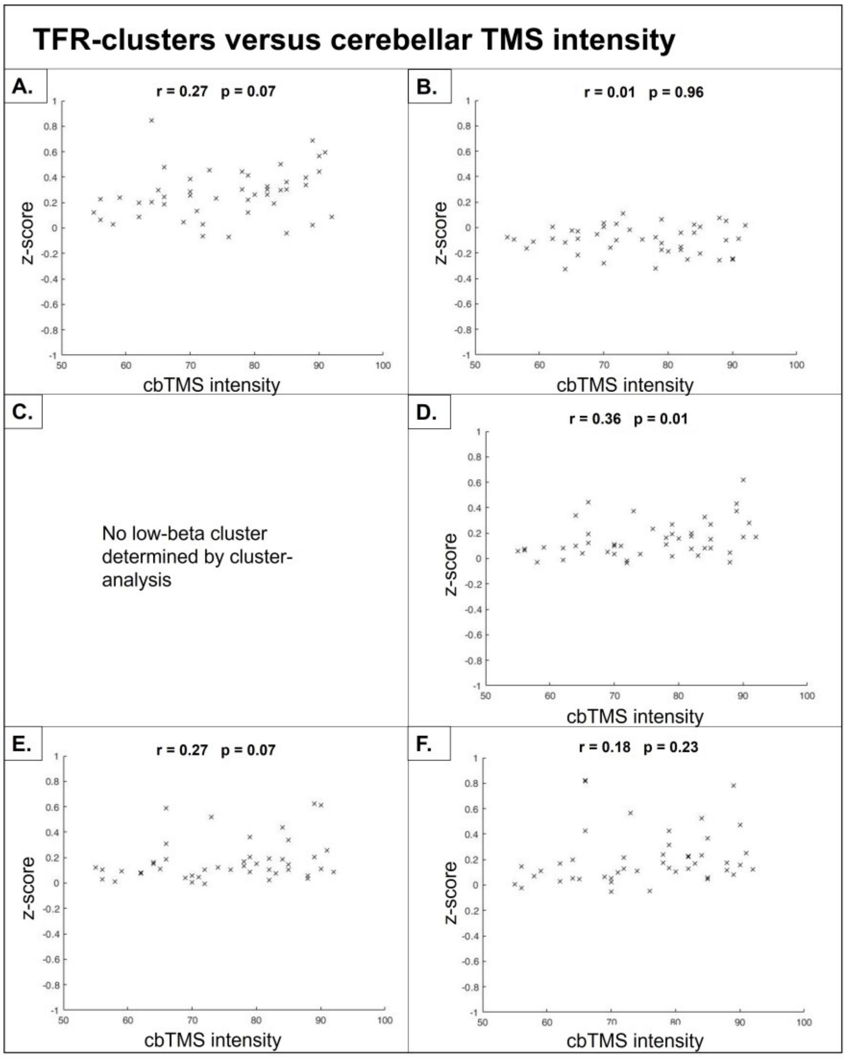

Figure 35: Scatterplot derived from Pearson correlation testing of TFR-clusters versus cbTMS intensity

For the depicted correlation analyses, the time-frequency response (TFR) clusters observed in the resting state between REAL involving cerebellar transcranial magnetic stimulation (cbTMS) with an upward induced current versus SHAM-MS were utilized (Figure 26). The resulting z-values of the TFR clusters were tested for a linear correlation (Pearson) with the cbTMS intensity values (n=46). The results of the correlation test are displayed on the top of the respective plot. Each black cross represents one subject. X-axis: cbTMS intensity in percent of maximum stimulator output (%MSO). Y-axis: z-score of the respective cluster. r: Pearson correlation coefficient. p: p-value with adjusted significance threshold to $p<0.002272$ to control for multiple tests. **A.** Theta (4-7Hz) from 50 to 290 ms. **B.** Alpha (8-12Hz) from 270 to 590 ms. **C.** Low beta (13-20 Hz): No significant cluster was determined in this frequency band. **D.** High beta (21-29 Hz) from 50 to 190 ms. **E.** Low gamma (30-40 Hz) from 50 to 200 ms. **F.** High gamma (60-90 Hz) from 50 to 250 ms.

3.1.7 Questionnaire: pain & discomfort

The results from the numeric rating scale indicated a large interindividual variability in tolerability and generally a moderate to low level of pain and discomfort (Figure 36) (Gassmann et al., 2022). While there was a difference (p<0.05) in the subjective pain and discomfort levels between REAL and SHAM-MS conditions on the group-level in experiment #1, no significant difference was found in experiment #2, where a fixed SHAM-MS intensity higher than the threshold determined in experiment #1 (see 3.1.3.1) was utilized (Gassmann et al., 2022). The effect sizes (Cohen's d) of the significant differences between SHAM-MS and REAL in experiment #1 were small (d=0.35) for discomfort scores and medium (d=0.64) for pain scores.

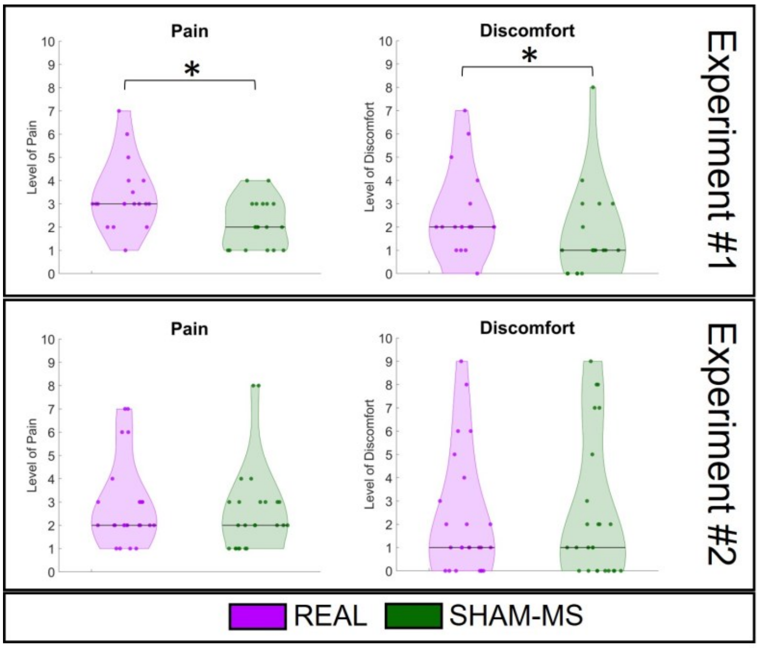

Figure 36: Numeric Rating Scales: level of reported pain and tolerability

Displayed are the subjective levels of pain and tolerability (0 = no pain or discomfort; 10 = maximum pain or discomfort) in the REAL (purple) and SHAM-MS (green) conditions. Each dot in each violine plots represents the individual ratings of one subject. Medians are indicated as horizontal black lines in the violin plots. Asterisks (*) indicate p<0.05. X-axis: condition. Y-axis: response on the numeric rating scale. **Top row:** data from experiment #1 of the resting state. **Bottom row:** data from experiment #2 of the resting state. **Source:** taken from (Gassmann et al., 2022), legend modified.

3.2 Applying the method in a clinical case

Parts of the following results have been published in a letter-to-the-editor (Gassmann et al., 2023a).

3.2.1 Scale for Assessment and Rating of Ataxia score (clinical case)

The SARA score on the day of the cbTMS measurements was 13.5 points, indicating mild to moderate ataxia symptoms (Gassmann et al., 2023a). A clear asymmetry of symptoms could be observed, presenting a hemiataxic syndrome of the left corporal side (Table 4) (Gassmann et al., 2023a).

Table 4: SARA score results of the patient on the day of cbTMS measurements

The table contains the results of the administered Scale for Assessment and Rating of Ataxia score (SARA) (Schmitz-Hubsch et al., 2006). **Left column:** tested item. **Middle column:** score determined for the item. **Right column:** standard description of scored item. **Source:** SARA score results from (Gassmann et al., 2023a), visualized as a table and additional information added.

ITEM		SCORE	DESCRIPTION
Gait		3	Considerable staggering, difficulties in half-turn, but without support
Stance		2	Able to stand with feet together for >10 s, but only with sway
Sitting		2	Constant sway, but able to sit > 10 s without support
Speech Disturbance		1	Suggestion of speech disturbance
Finger chase	Left	2	Dysmetria, under-/overshooting target <15 cm
	Right	0	No dysmetria
Nose-finger test	Left	2	Tremor with an amplitude <5 cm
	Right	0	No tremor
Fast alternating hand movements	Left	4	Unable to complete 10 cycles
	Right	0	Normal, no irregularities (performs <10 s)
Heel-shin slide	Left	3	Severely abnormal, goes off shin 4 or more times during 3 cycles
	Right	0	Normal

3.2.2 *Magnetic resonance imaging & diffusion tensor imaging tractography (clinical case)*

In the inspection of the MRI, substantial parts of the right mesial temporal and occipital lobes were encompassed by a lesion, also affecting the pulvinar and ventroposterior nucleus of the right thalamus (Figure 37) (Gassmann et al., 2023a). "*Total surface areas of the right and left DTCs were 18332 mm^2 and 11383 mm^2, respectively. Fractional anisotropy values recorded at each voxel traversed by the tracts were similar (voxel level: T(60661)=0.421, p=0.674) for the right DTC (mean=0.486, SD=0.143) and left DTC (mean=0.485, SD=0.134). Overall mean diffusivity values recorded the same way were lower (voxel level: T(60661)=5.234, p=1.668 x 10^{-7}) for the right DTC (mean=0.710, SD=0.211) than for the left DTC (mean=0.729, SD=0.273). Axial diffusivity values were lower (voxel level: T(60661)=3.203, p=0.001) for the right DTC (mean=1.124, SD=0.316) than for the left DTC (mean=1.142, SD=0.378). Radial diffusivity values were lower (voxel level: T(60661)=5.813, p=6.151 x 10^{-9}) for the right DTC (mean=0.502, SD=0.199) than for the left DTC (mean=0.522, SD=0.251).*" (Gassmann et al., 2023a).

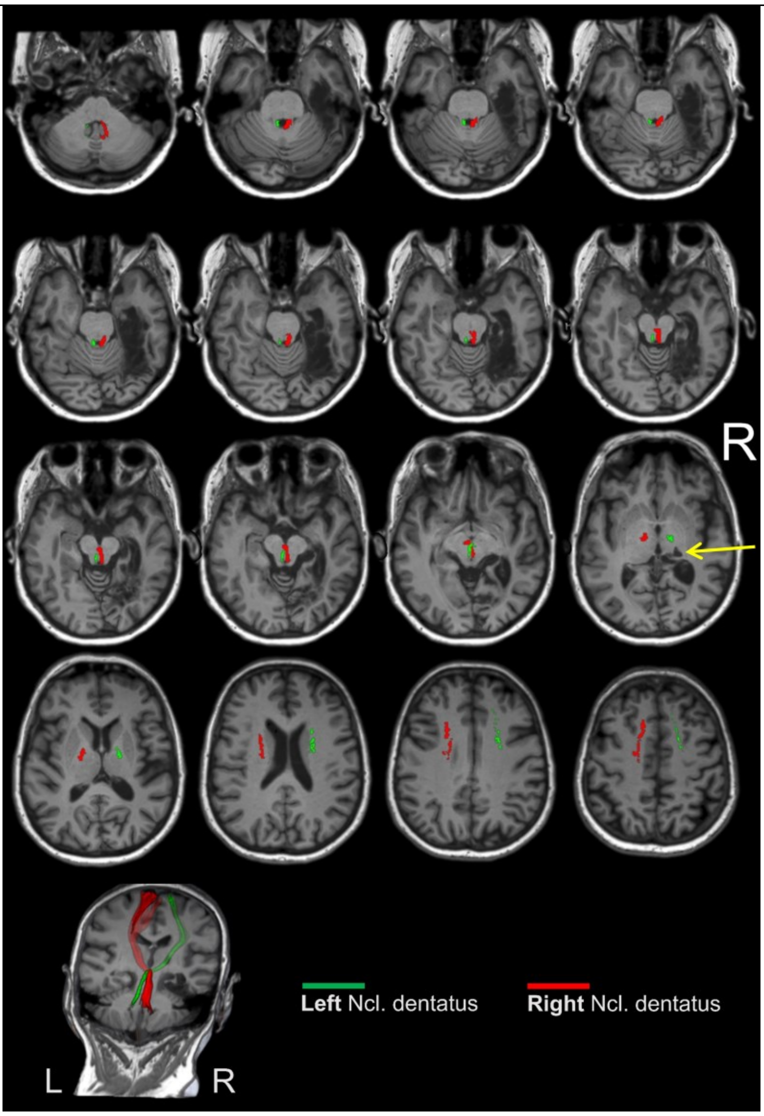

Figure 37: T1-weighted structural cMRI of the patient in combination with tractography

The decussating dentato-thalamo-cortical tract (DTC) originating from right (red) and left (green) dentate nuclei are overlaid on T1-weighted structural axial slices of the cranial magnetic resonance imaging (cMRI). The demarcated infarction in the territory of the posterior cerebral artery (PCA) of the right cerebral hemisphere stroke encompassed parts of white and gray matter of the right mesial temporal lobe and parts of the occipital lobe. Additionally, the infarction has affected parts of the right pulvinar and ventroposterior thalamus (yellow arrow) in the vascular territory of the thalamogeniculate artery originating from the P1 segment of the PCA. Consecutive *e vacuo* widening of the inferior and posterior horns of the right lateral ventricle. The DTC originating from the left dentate nucleus has a lower number of streamlines and a lesser volume than its contralateral counterpart. R: right (neurological convention). Ncl.: nucleus **Source:** taken from (Gassmann et al., 2023a), legend modified.

3.2.3 Combined results (clinical case)

In the following results, right and left DTC refers to the reconstruction of the DTC via DTI tractography (see 2.2.3) with the reconstruction originating from the right or left dentate nucleus in the cerebellum. When observing the results of the DTI tractography (see also 3.2.2), the reconstructed DTC which originated from the dentate nucleus in the right cerebellar hemisphere (right DTC) was larger than the left DTC (Gassmann et al., 2023a). While DTI tractography yielded 988 streamlines with a total volume of 6433 mm^3 on the right side, the reconstructed left DTC yielded 75 streamlines with a total volume of 2614 mm^3 (Figure 38C) (Gassmann et al., 2023a).

CBI was observed with paired-pulse TMS eliciting an MEP suppression to 80% of the average amplitude of the single-pulse TMS to the primary motor cortex (Figure 38A) (Gassmann et al., 2023a). The estimation of the induced electric field strength of cbTMS in the cerebellar cortex yielded comparable field distributions and field strengths between left and right cbTMS (Figure 38B) (Gassmann et al., 2023a).

TMS to the right cerebellar hemisphere evoked a fronto-central positive deflection contralateral to the site of cbTMS, peaking at ~25 ms post cbTMS (Figure 38E) (Gassmann et al., 2023a). TMS to the left cerebellar hemisphere, in which a structurally affected DTC was reconstructed, did not elicit a similar potential in this time-window (Figure 38F) (Gassmann et al., 2023a). A negative deflection of large amplitude in fronto-central electrodes was observed 100 ms after cbTMS was delivered as an EEG response - irrespective of the side to which cbTMS was delivered (Gassmann et al., 2023a) (Figure 38E-F). When comparing EEG responses to right and left cbTMS with a cluster-based permutation statistics (see 2.2.6), a significant ($p<0.001$) and relevant ($d=1.29$ (Cohen’s d); 95% confidence interval: [+1.20 +1.48]) positive cluster in left fronto-central electrodes was observed ranging from 20 ms to 25 ms after cbTMS was delivered (Figure 38D) (Gassmann et al., 2023a). Notably, no significant cluster in fronto-central electrodes ~100 ms post-cbTMS was determined (Gassmann et al., 2023a). Clusters in late time-windows were discarded, since no SHAM-MS condition was applied (Gassmann et al., 2023a).

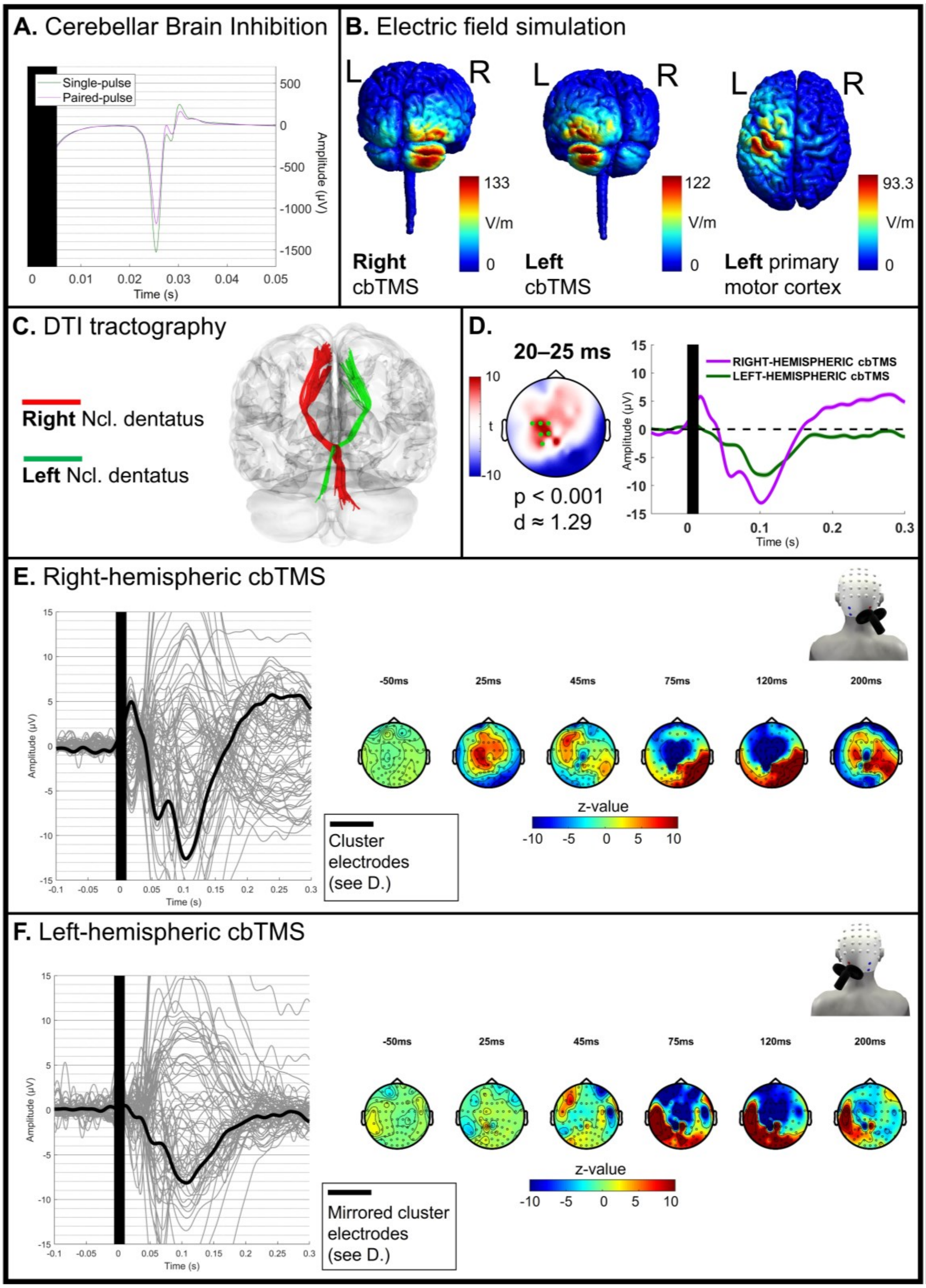
A. Cerebellar Brain Inhibition
Single-pulse
Paired-pulse
500
0
-500
-1000
-1500
Amplitude (µV)
0
0.01
0.02
0.03
0.04
0.05
Time (s)
B. Electric field simulation
L
R
133
V/m
0
Right
cbTMS
L
R
122
V/m
0
Left
cbTMS
L
R
93.3
V/m
0
Left primary
motor cortex
C. DTI tractography
Right Ncl. dentatus
Left Ncl. dentatus
D.
20–25 ms
10
t
-10
p < 0.001
d ≈ 1.29
RIGHT-HEMISPHERIC cbTMS
LEFT-HEMISPHERIC cbTMS
15
10
5
0
-5
-10
-15
Amplitude (µV)
0
0.1
0.2
0.3
Time (s)
E. Right-hemispheric cbTMS
15
10
5
0
-5
-10
-15
Amplitude (µV)
-0.1
-0.05
0
0.05
0.1
0.15
0.2
0.25
0.3
Time (s)
Cluster
electrodes
(see D.)
-50ms
25ms
45ms
75ms
120ms
200ms
z-value
-10
-5
0
5
10
F. Left-hemispheric cbTMS
15
10
5
0
-5
-10
-15
Amplitude (µV)
-0.1
-0.05
0
0.05
0.1
0.15
0.2
0.25
0.3
Time (s)
Mirrored cluster
electrodes
(see D.)
-50ms
25ms
45ms
75ms
120ms
200ms
z-value
-10
-5
0
5
10

Figure 38: Results when applying the method to a patient with secondary neurodegeneration on one side

A. Cerebellar brain inhibition (CBI) assessment performed on the subject with the time-course of the electromyography (EMG) response in the right first dorsal interosseus (FDI). Green: EMG response to transcranial magnetic stimulation (TMS) to the primary motor cortex. Purple: EMG response to paired-pulse TMS to the right cerebellar hemisphere preceding TMS to the left primary motor cortex. Y-axis: amplitude in µV. X-axis: time in seconds (s). Black bar indicates the TMS pulse. **B.** Electric field simulation of cerebellar TMS (cbTMS) to the right and left cerebellar hemisphere. Next to each plot is the calibration bar indicating the peak electric field in V/m. R: right. L: left. **C.** Glass brain representation of the reconstructed dentato-thalamo-cortical tract (DTC). Red: DTC originating from the right dentate. Green: DTC originating from the left dentate. Ncl.: Nucleus. **D.** Topographical plot displays the results from the cluster-based independent-sample t-statistics comparing electroencephalography (EEG) responses elicited by cbTMS to the right cerebellar versus left cerebellar hemisphere. The time window of the significant positive cluster is 20–25 ms. P-value and Cohen’s d are indicated below the topographical plot. EEG channels marked as green dots indicate the significant cluster. The time course plot displays the EEG responses from right cbTMS (purple) and left cbTMS (green), averaged across the channels that composed the significant cluster indicated in the topographical plot. Y-Axis: amplitude in µV. X-axis: time in seconds (s). **E.** Butterfly plot of the time-course of the EEG response to right cbTMS. The thick black line corresponds to the left-hemispheric electrodes determined by the cluster analysis (see D.), each grey line corresponds to one EEG channel. The black bar corresponds to the TMS pulse. X-axis: time in seconds (s). Y-axis: amplitude in µV. Topographical plots display the spatial distribution of the EEG signal at certain time-points, as indicated above the respective topographical plot. **F.** Butterfly plot of the time-course of the EEG response to left cbTMS. The thick black line corresponds to right-hemispheric electrodes mirroring the left-hemispheric cluster. Otherwise, same conventions as in E. **Source:** taken from (Gassmann et al., 2022), figure and legend modified.

4 Discussion

Parts of the following discussion have been published in an original research article (Gassmann et al., 2022), in a letter-to-the-editor (Gassmann et al., 2023a) and in a commentary (Gassmann et al., 2023b).

The cerebellar cortex is a challenging target for TMS. Concomitant stimulation of the occipital cortex and strong somatosensory input due to high TMS intensities being applied have so far impeded the identification of EEG responses specifically elicited by cbTMS. In this exploratory study, cbTMS was delivered at a novel level of control, applying control conditions specifically adapted for cbTMS and leveraging state-of-the-art data cleaning methods for artefact removal. Utilizing the convergence of evidence of different methods to assess EEG markers of cbTMS, specific EEG responses to cbTMS could be identified in resting state and were subsequently tested in a clinical case.

4.1 Methodology: challenges, limitations, opportunities

In the following, the applied methodology will be discussed critically, taking into consideration its limitations, and leveraging its strengths as a starting point for future cbTMS-EEG studies.

4.1.1 cbTMS parameters

Confirming that the cerebellar cortex was reached with sufficient electric field strength by cbTMS was crucial in this study, because of its exploratory nature. Hence, the intensity to deliver cbTMS was determined on the basis of the established method of CBI assessment, providing indirect evidence for effective cbTMS. CBI could reliably be elicited (see 3.1.2.1) (Gassmann et al., 2022). Additionally, the electric field induced over the cerebellar cortex at this intensity was evaluated by simulating the electric field. Considering the results of the simulation of the electric field (Figure 9), the average electric field strength induced over the cerebellar cortex (120 V/m) with cbTMS at the intensity determined through CBI was higher than the average electric field induced over the primary motor cortex (87 V/m) at the RMT intensity (Gassmann et al., 2022). Since MEPs are elicited at the RMT, an electric field of this strength is capable of depolarizing corticospinal neurons in the primary motor cortex. Hence, this is providing converging evidence that the cbTMS intensity applied in this study was capable of depolarizing neurons in the cerebellar cortex.

Nonetheless, there is an active debate in the field about the optimal TMS coil to assess CBI (Hardwick et al., 2014, Spampinato et al., 2020, Fernandez et al., 2018, Can et al., 2019). Consequently, the adequateness of the selected TMS coil to deliver cbTMS in this study (see 2.1.2) will be scrutinized in the following. Figure-of-eight coils with a similar diameter as the one utilized in this study to deliver cbTMS (see 2.1.2) - but with a full casing - were tested and were described by some authors to have elicited CBI unreliably, favoring double-cone coils for CBI assessment (Hardwick et al., 2014, Spampinato et al., 2020). Spampinato et al. assessed CBI with a range of double-cone coils by different manufacturers and compared the resulting CBI (Spampinato et al., 2020). Even though Spampinato et al. state that double-cone coils would be more appropriate and reliable to deliver cbTMS than figure-of-eight coils (Spampinato et al., 2020), since their study was limited to the testing of double-cone coils, their findings provide no direct evidence of the supposed superiority of double-cone coils in delivering cbTMS and assessing CBI. Furthermore, Spampinato et al. found that uncoated coils set to maximum tolerable TMS intensity were eliciting significantly stronger suppression of MEPs, and thus, a more pronounced CBI (Spampinato et al., 2020). The absence of a full casing allows for a closer distance between coil and cortex. The coil utilized in the current study to deliver cbTMS had no casing, as it was a branding iron coil (see 2.1.2). Therefore, the findings of Spampinato et al. provide direct evidence to prefer uncoated TMS coils over coated TMS coils when assessing CBI, as was the case in the current study (see 2.1.2). The study by Hardwick et al. tested different figure-of-eight coils with a full casing and applied a fixed maximum TMS intensity of up to 80 %MSO (Hardwick et al., 2014), while the intensity utilized in the current study to deliver cbTMS was above 80 %MSO for a number of subjects (see 3.1.2.1), and the TMS coil utilized to deliver cbTMS did not have a casing (see 2.1.2).

It should be noted that figure-of-eight coils have been used regularly to elicit CBI in previous studies (Fernandez et al., 2018). A recent study performing a direct comparison of figure-of-eight and double-cone coils to deliver cbTMS found no systematic difference between these coil types and stated that the figure-of-eight coil is suited for focal cbTMS (Can et al., 2019) – in this work, the person who first described the phenomenon of CBI participated as last author, Yoshikazu Ugawa (Ugawa et al., 1995). Lastly, it can be concluded that CBI was reliably elicited utilizing an uncoated figure-of-eight coil, as evidenced by the individual CBI assessment results provided (see 3.1.2.3) (Gassmann et al., 2022).

After the discussion of the cbTMS intensity and TMS coil selection in the last paragraphs, the method of targeting the cerebellar cortex with TMS will be discussed in the following. The state-of-the-art method is the utilization of anatomical surface landmarks (Fernandez et al., 2018). In the current study, an anatomical surface landmark was chosen as well (see 2.1.2) (Gassmann et al., 2022). Consequently, since individual anatomy varies, the peak electric field may not target the same functional regions for all subjects. Nonetheless, the electric field simulation in the current study shows a broad distribution of the electric field over the cerebellar cortex, even reaching inferior-posterior occipital cortical areas (see 3.1.2.2) (Gassmann et al., 2022). This, in combination with the rather homogenous CBI values with most subjects being within ± 1 SD of the mean CBI (see 3.1.2.1) (Gassmann et al., 2022), provides evidence that the electric field delivered to the cerebellar cortex in this study was comparable across subjects.

4.1.2 Control conditions

In this study, a TMS coil delivering MS to the shoulder was added and the intensity of MS titrated until a plateau in the N100 response was reached, termed the SHAM-MS (see 2.1.8.1) (Gassmann et al., 2022). In the REAL, cbTMS was delivered simultaneously with the stimuli of SHAM-MS (Gassmann et al., 2022). The assumption was, that a subtraction of EEG responses elicited by SHAM-MS from the EEG responses elicited by REAL unveiled the cerebellar component of the EEG response (Gassmann et al., 2022). However, even though previous studies could demonstrate that EEG sensory responses and TEPs have a potential overlap in time, and thus affect the measured amplitude of one another (Biabani et al., 2019, Conde et al., 2019, Rocchi et al., 2021, Gordon et al., 2018), the nature of this overlap has not been conclusively investigated. EEG sensory responses and TEPs may merely overlap in time, or they may interact with one another in more complex ways, which lead some authors to suggest an entanglement of the responses (Rocchi et al., 2021). Nonetheless, previous studies demonstrated that this occurs in the time-window 60 ms (Biabani et al., 2019) to 70 ms post-TMS (Conde et al., 2019, Gordon et al., 2021, Ahn and Frohlich, 2021), while EEG responses before this time-window have not been observed to be affected. Consequently, EEG responses to cbTMS observed before this time-window should remain unchanged by the subtraction of SHAM-MS responses, which was the case in this study (Figure 22, Figure 26) (Gassmann et al., 2022). However, it also follows that the method of simple arithmetic subtraction of EEG responses may pose a limitation for TMS responses observed in time-windows beyond 60-70 ms post-TMS, if the interaction of EEG sensory responses and TEPs would be found to be more complex in future studies. The method of simple arithmetic subtraction was chosen for its simplicity and practicability, and to make the least assumptions possible.

Another novel control condition applied in this study was the occipital control condition (Gassmann et al., 2022). This was done in response to the remarks about possible concomitant TMS to the occipital cortex by Fernandez et al. when assessing the feasibility of cbTMS-EEG (Fernandez et al., 2021). The occipital control condition was delivered with the same TMS intensity and with the same SHAM-MS condition as cbTMS with an upward induced current, but the TMS coil was placed superior to the site of stimulation for cbTMS to deliberately target the occipital cortex in close proximity to the cerebellar target (see 3.1.3.2) (Gassmann et al., 2022). The results in this study demonstrate that concomitant stimulation of the occipital cortex can occur when delivering cbTMS (Gassmann et al., 2022). This interpretation is supported by a confluence of evidence. Firstly, the significant late positive cluster in right occipital electrodes (Figure 14) bore resemblance to the positive cluster in right occipital electrodes when delivering cbTMS with an upward induced current (Figure 22) (Gassmann et al., 2022). Secondly, the simulation of the electric field showed that posterior parts of the occipital lobe are encompassed by the electric field generated by cbTMS (Figure 9) (Gassmann et al., 2022). Thirdly, when inspecting the projection onto the source level of the EEG responses to the occipital control condition, the late cluster 200-480 ms over right occipital areas (Figure 30) showed similarity with the right occipital part of the cluster 181-481 ms post-cbTMS with an upward induced current (Figure 29) (Gassmann et al., 2022).

The effect of electric field directionality was tested by applying cbTMS with a downward induced current (see 2.1.8.3) (Gassmann et al., 2022). In this study, it was observed that both cbTMS with an upward and downward induced current elicited a similar cb-P25 potential (Figure 18, Figure 22) and a high beta increase in electrodes over the contralateral prefrontal cortex (Figure 19, Figure 25) (Gassmann et al., 2022). Nonetheless, the cb-N45 was configured differently when cbTMS was delivered with a downward induced current (Figure 18) (Gassmann et al., 2022). A possible explanation for this observation would be, that depending on the directionality of the electric field, cells in the cortex are differentially responsive, causing this difference. Ugawa et al. observed cbTMS with an upward induced current to be more effective in eliciting CBI and attributed this difference to be due to cerebellar anatomy, stating that most axons of the Purkinje cells in the cerebellar cortex are oriented upward and lateromedial towards the dentate nucleus (Ugawa et al., 1995).

Tolerability of cbTMS has only been assessed by few previous studies, which have described the figure-of-eight TMS coil to be more tolerable than other TMS coil types (Fernandez et al., 2018). The numeric rating scale for pain and discomfort applied in this study showed moderate levels of pain and discomfort when applying either SHAM-MS or REAL (Figure 36) (Gassmann et al., 2022). When individually titrating the SHAM-MS intensity in experiment #1, a significant difference was observed (Gassmann et al., 2022). When selecting a suprathreshold SHAM-MS intensity in experiment #2, no significant difference between SHAM-MS and REAL was observed, possibly due to a better saturation of multisensory input (Figure 36) (Gassmann et al., 2022).

4.1.3 Calculation of time-frequency responses

Before applying the TFR calculation method (see 2.1.10.3), its validity was critically evaluated and will therefore be discussed in the following.

To this end, 100 trials of a signal containing an alpha oscillation and noise were simulated. Then, two conditions were created, one that added a transient deflection of constant amplitude at time=0 of all trials, simulating an ideal SEP, shape-invariant, and another condition that added transients of varying amplitude from trial to trial, simulating a realistic SEP, shape-variant. Time-frequency representations calculated should correspond solely to the modulation of non-phase-locked induced oscillations (Pellicciari et al., 2017), not to the evoked response.

One method of calculating the TFR is subtracting the average EEG signal time-locked to TMS from the total signal and calculating time-frequency representations from the result (Gordon et al., 2021). Applying this method, the presence of a transient of varying amplitude led to a residual response on the time-frequency analysis (Figure 39). Therefore, time-frequency representations calculated utilizing this methodology might contain residual phase-locked evoked responses, affecting the calculated induced oscillations.

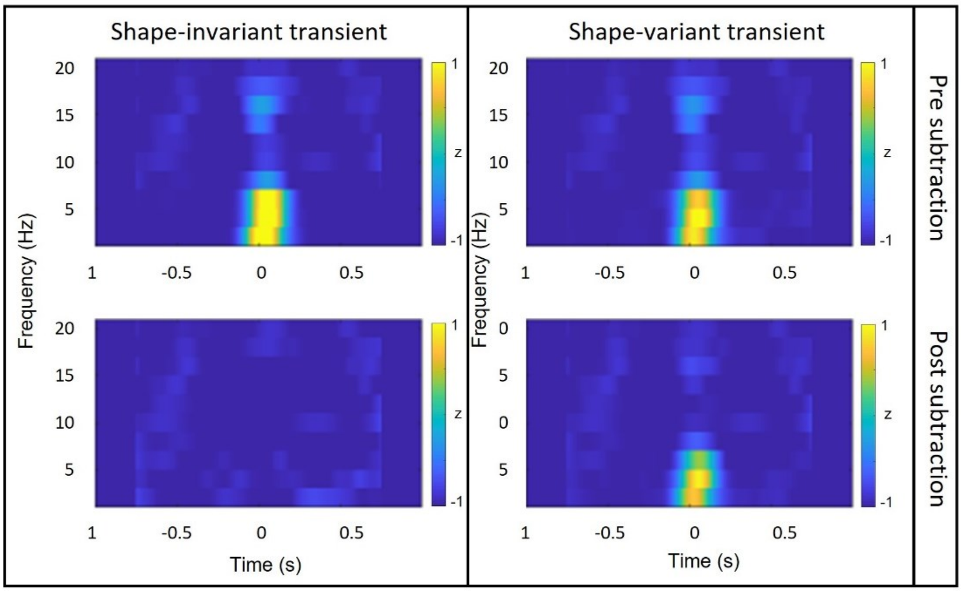

Figure 39: Time-frequency-response calculation method: trial-by-trial subtraction of the time-locked average of all trials

Results of the analyses of a simulated signal containing an alpha oscillation and noise. The signal was divided in 100 trials in which a transient deflection of constant amplitude at time=0 was added (shape-invariant), and 100 trials in which a transient deflection of varying amplitude at time=0 was added (shape-variant). Plots correspond to the time-frequency responses of the signals, averaged across all trials. The top row corresponds to the results from the unchanged signal, and the bottom row corresponds to the result from the signal following the trial-by-trial subtraction of the evoked response, ergo the time-locked average of all trials. Calibration bars next to the respective plot. **X-axis:** time (s). **Y-axis:** frequency (Hz).

Consequently, a TFR calculation method involving subtraction of the time-frequency representations of the evoked EEG potentials from the single trials' time-frequency representations (Pellicciari et al., 2017) was chosen (Gassmann et al., 2022) to circumvent the problem of shape-invariant SEPs affecting the calculated TFR.

To test this approach, another 100 trials of a signal containing an alpha oscillation and noise were simulated. Then, two conditions were created, one that added a transient deflection of constant amplitude at time=0 of all trials, simulating an ideal SEP, shape-invariant, and another condition that added transients of varying amplitude from trial to trial, simulating a realistic SEP, shape-variant. Applying the aforementioned method on the data confirmed that the simulated evoked response did not affect the calculated TFR (Figure 40).

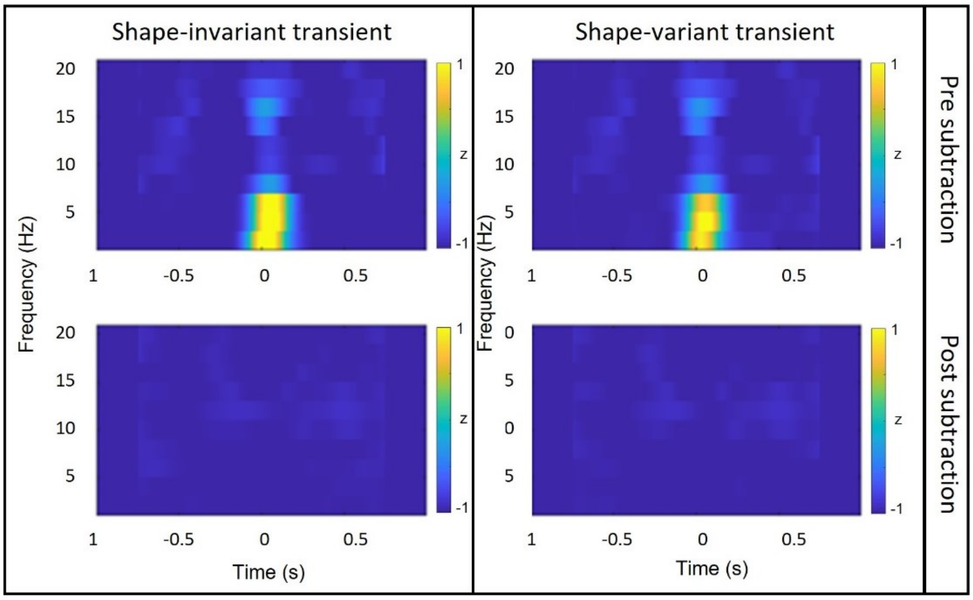

Figure 40: Time-frequency-response calculation method: subtracting the time-frequency representations of the evoked EEG potentials from the single trials' time-frequency representations

Results of the analyses of a simulated signal containing an alpha oscillation and noise. The signal was divided in 100 trials in which a transient deflection of constant amplitude at time=0 was added (shape-invariant), and 100 trials in which a transient deflection of varying amplitude at time=0 was added (shape-variant). Plots correspond to the time-frequency responses of the signals, averaged across all trials. The top row corresponds to the results from the unchanged signal. The bottom row corresponds to the result from the time-frequency analysis following the trial-by-trial subtraction of the time-frequency response of the evoked response (the time-locked average of all trials). Calibration bars next to the respective plot. **X-axis:** time in seconds (s). **Y-axis:** frequency in Hertz (Hz).

4.1.4 Source analysis

A projection of results into the source space can provide additional information on the origin of the identified cbTMS-specific EEG responses. In the resting state study, a generic head model from an MNI atlas was utilized to project EEG responses into the source space (see 2.1.10.6) (Gassmann et al., 2022). Consequently, these results had to be interpreted cautiously. Alternatively, MRIs from all subjects would have needed to be collected to calculate a common head model. However, as the main objective of this exploratory study was the identification of specific EEG responses to cbTMS, and the assessment of the feasibility of cbTMS utilizing several control conditions, acquiring individual MRIs from all subjects was beyond the scope. The 8 individual MRIs acquired from resting state subjects did not provide a sufficient sample size for proper source analysis, and as they represented only a minority of subjects, were not sufficient to project EEG responses observed on the group level. Instead, these 8 individual MRIs from randomly selected subjects served the purpose of electric field modelling with a sufficient sample size (see 2.1.6.2) (Gassmann et al., 2022). Future studies testing cbTMS-EEG could acquire individual MRIs for all participants for a more accurate source analysis.

4.1.5 Diffusion tensor imaging tractography

The reconstruction of the DTC utilizing DTI tractography (see 2.2.3) in the patient was complementary to the assessment of the clinical syndrome with delayed-onset left hemiataxia (see 2.2.1), as the clinical syndrome could plausibly be explained by a neurodegeneration of the left DTC through transneuronal connectional diaschisis resulting from the pulvinar lesion (Gassmann et al., 2023a). Furthermore, the T1-weighted MRI showed a large lesion in the right hemisphere and a structurally intact left hemisphere (Figure 37) (Gassmann et al., 2023a). Nonetheless, DTI tractography provided important additional evidence for a structural impairment of one DTC. The accurate reconstruction of the DTC utilizing DTI tractography is challenging, as the DTC is a decussating tract. Possible sources for reconstruction errors and the applied methodology to avoid these errors will be discussed in the following.

The DTC is a decussating, large fiber tract (see 1.2). Fiber tracking across decussations carries the risk of reconstruction errors due to complex fiber configurations in these voxels, which was termed the crossing fiber problem (Jones et al., 2013, Gassmann et al., 2023a). Several quality checks had to be conducted to mediate this challenge and to report an asymmetry of the DTC (Gassmann et al., 2023a).

One quality check involved the inspection of the raw analysis without any manual pruning of non-decussating streamlines (Gassmann et al., 2023a). This raw analysis yielded an asymmetry, with 17798 streamlines representing the right DTC and 6659 representing the left DTC (Gassmann et al., 2023a). Furthermore, another method utilizing a different algorithm was applied (Yeh et al., 2010, Gassmann et al., 2023a). With this alternative method, an asymmetry was observed, with the right DTC showing greater volume than the left DTC (Gassmann et al., 2023a). "*The above* [other method with a different algorithm] *reported significantly different diffusivity values with lower overall mean diffusivity, axial and radial diffusivity in the right DTC compared to the left DTC*" (Gassmann et al., 2023a). This finding was indicative of an altered microstructure in the DTC originating from the left dentate nucleus (Gassmann et al., 2023a).

In conclusion, the observed asymmetry of the DTC in DTI tractography was robust. DTI tractography may be applied in cbTMS-EEG studies as part of convergent evidence when testing the structural intactness of the DTC.

4.2 Discussion of results

Through the development and application of novel control conditions specifically addressing the challenges of delivering cbTMS, specific EEG responses could be identified - namely, the cb-P25 and cb-N45, and a contralateral prefrontal increase in high beta power (Gassmann et al., 2022). These responses most likely reflect the activation of the predominant cerebellar efferent pathway, the DTC. As a starting point for testing these EEG responses in clinical populations, they were tested in one patient with an asymmetry of the DTC post-stroke (Gassmann et al., 2023a). These interpretations and the results of the clinical case will be discussed in the following.

4.2.1 cbTMS elicits specific TEPs: cb-P25 and cb-N45

When delivering cbTMS and comparing SHAM-MS to REAL in resting state, significant differences were observed (Gassmann et al., 2022). The observed clusters, and whether they were found to be specific to cbTMS, will be discussed in the following.

4.2.1.1 P25 and N45

Two early clusters were observed in conditions involving cbTMS with an upward or downward induced current - a positive left prefrontal cluster peaking ~25 ms post-TMS, and a negative cluster over the left fronto-parietal cortex peaking ~45 ms post-TMS (Figure 22) (Gassmann et al., 2022). A positive EEG potential in a TEP peaking after 25 ms is referred to as P25, a negative EEG potential peaking after 45 ms as N45. Consequently, these clusters were termed "*cb-P25*" and "*cb-N45*" (Gassmann et al., 2022).

As to the observed cb-N45 (Gassmann et al., 2022), Fernandez et al. observed a comparable negative cluster applying cbTMS utilizing a double-cone coil, and hypothesized this cluster may be specifically attributable to the DTC, but stated that further investigations were necessary to test this hypothesis (Fernandez et al., 2021). As the current study involved a SHAM-MS control as well as an occipital control condition, and since the cb-N45 remained specific to cbTMS, the cb-N45 was found to be specific to cbTMS (Gassmann et al., 2022). Moreover, the cb-P25 was not observed in control conditions and remained specific to cbTMS (Gassmann et al., 2022). Due to the spatial distribution, with both clusters being observed contralaterally to the site of cbTMS and in electrodes over prefrontal and parietal areas, we understood them to most likely indicate an "*activation of the DTC*" (Gassmann et al., 2022).

Taking into consideration the neuroanatomy of the cerebellum, this interpretation is feasible. Efferent projections of the cerebellum predominantly traverse dentate and thalamic nuclei - with the most relevant being motor, sensory, parietal, and prefrontal loops (D'Angelo, 2018). Utilizing high resolution tractography, it has been demonstrated in humans *in vivo* that the cerebellum is connected with contralateral prefrontal and associative areas (Palesi et al., 2015, Palesi et al., 2017), as was also shown in anatomical investigations *ex vivo* (Voogd, 2003). Utilizing the transneuronal transport of neurotropic viruses in non-human primates, it was found that efferent cerebello-dentato-thalamo-cortical projections predominantly target the contralateral primary motor cortex and the dorsolateral prefrontal cortex (Kelly and Strick, 2003). In another study utilizing retrograde transneuronal transport of viruses in non-human primates, when injecting the virus in the posterior parietal cortex, its transport labeled substantial numbers of neurons in the dentate nucleus of the cerebellum, supporting the argument that the posterior parietal cortex is another target of cerebellar output (Clower et al., 2005). In human fMRI studies, connectivity was found between the cerebellar cortex and the contralateral parietal cortex (Buckner et al., 2011, O'Reilly et al., 2010). The converging evidence of these different methods is indicative of prefrontal and parietal areas being predominant targets of the cerebellar efferent projections.

The cb-N45 and cb-P25 clusters were reproduced across two experiments, were not observed in any of the control conditions (Gassmann et al., 2022) and are anatomically plausible to reflect a response to TMS to the cerebellar cortex (see previous paragraph). Therefore, these responses were interpreted to reflect an activation of the DTC (Gassmann et al., 2022).

When investigating the amplitude distributions of the cb-P25 and cb-N45 elicited by SHAM-MS and REAL, further evidence could be provided that a SHAM-MS condition is not needed to observe these EEG potentials occurring before 60-70 ms post-cbTMS, as SHAM-MS responses in these electrodes in these time-windows showed a normal distribution with an expected value ~0 µV (Figure 26) (Gassmann et al., 2022). Furthermore, the individual amplitudes of the cb-P25 and cb-N45 were analyzed, and further evidence provided that they were reliably reproducible across the two experiments and elicited by a majority of subjects (Figure 27) (Gassmann et al., 2022). Figure 26 visualizes comprehensively that cb-P25 and cb-N45 were normally distributed (Gassmann et al., 2022). However, no linear correlations between any observed significant cluster when delivering cbTMS with an upward induced current (Figure 22) and either individual CBI or cbTMS intensity values were found (Figures 32-35) (Gassmann et al., 2022).

4.2.1.2 N100

Across recent studies applying cbTMS, different EEG responses have been attributed to cbTMS (Gassmann et al., 2023b, Gassmann et al., 2022, Fong et al., 2023, Du et al., 2017). Namely, Fong et al. attributed a P80 and N110 EEG potential specifically to cbTMS (Fong et al., 2023). Du et al. attributed the N100 potential observed post-TMS to cbTMS (Du et al., 2017). The N110 and N100 potential attributed to cbTMS in recent studies (Fong et al., 2023, Du et al., 2017) most likely reflect an unspecific response to sensory input, as evidenced by the SHAM-MS results in the current study, which elicited a similar N100 potential (see 3.1.4) (Gassmann et al., 2022), and the multitude of studies that observed an overlapping of sensory-evoked responses with TEPs in the time-window beyond 60-70 ms post-TMS (Gordon et al., 2021, Biabani et al., 2019, Ahn and Frohlich, 2021, Conde et al., 2019). Consequently, EEG responses observed in this time-window cannot safely be specifically attributed to cbTMS.

Nonetheless, the N100 component observed in the current study when delivering cbTMS was indeed significantly different from SHAM-MS (Figure 22) (Gassmann et al., 2022). Namely, a negative cluster over left parietal areas was found highly reproducibly 100 ms post-cbTMS with either an upward (Figure 22) or downward (Figure 18) induced current after subtracting SHAM-MS from REAL (Gassmann et al., 2022). The spatial distribution of this cluster was significantly different from the SHAM-MS responses, as it was observed over left parietal (Gassmann et al., 2022) instead of midline fronto-central regions, which is atypical for an unspecific EEG response to sensory input (Ilmoniemi and Kicic, 2010). A direct comparison of the N100 responses between the conditions showed that this parietal cluster was specifically elicited by cbTMS (Figure 23). One interpretation of this result was, that it may indicate an insufficiency of the SHAM-MS procedure and the method of simple arithmetic subtraction to completely resolve the issue of an overlap of EEG responses to cbTMS-associated sensory input with TEPs in this time-window (Gassmann et al., 2022), due to the issues discussed in the previous paragraph. An alternative interpretation of this finding was, that it might be a response specifically elicited by cbTMS (Gassmann et al., 2022). However, since the nature of interaction between TEPs and overlapping EEG responses to sensory input has still not been conclusively clarified - they may overlap in time (Gordon et al., 2021, Conde et al., 2019, Ahn and Frohlich, 2021, Biabani et al., 2019) or influence one another in more complex ways (Rocchi et al., 2021) – a specific attribution of these EEG potentials as a marker of cbTMS currently has to be rendered improper.

Whether the P80 response observed by Fong et al. (Fong et al., 2023) reflects a specific EEG response to cbTMS remains at question, as no electric field simulation was provided in this study to confirm that the electric field reached the cerebellar cortex with sufficient strength, and as there is a lack of adequate control conditions for sensory input and concomitant activation of proximal brain regions, such as the posterior-inferior occipital cortex. Since a double-cone coil was utilized by Fong et al. (Fong et al., 2023), the electric field distribution varied greatly from the figure-of-eight coil used in the current study to deliver cbTMS (see 2.1.2) (Gassmann et al., 2022). It could have reached unintended targets with sufficient electric field strength, as double-cone coils generate a field that reaches deeper and less focal in the brain tissue than figure-of-eight coils, and since unintended targets such as the posterior-inferior occipital cortex were already reached even with the comparatively small, focal figure-of-eight coil utilized in the current study (Figure 9) (Gassmann et al., 2022). Nonetheless, the P80 potential may be a specific EEG marker to delivering cbTMS with a double-cone coil and its associated electric field distribution over the cerebellar cortex, highlighting the importance of specifically targeting functional modules of the cerebellum in future investigations.

4.2.1.3 Late TEPs

Two late clusters were observed when delivering cbTMS with an upward induced current (Gassmann et al., 2022). Namely, a persistent positive cluster in electrodes over the right occipital cortex, lasting from 180 ms to 320 ms in experiment #1, and up to 480 ms in experiment #2, and a long-lasting negative cluster at the same time-window in electrodes over the left parietal cortex (Figure 22) (Gassmann et al., 2022). Because of overlapping with unspecific EEG responses and for the reasons discussed above (see 4.2.1.2), these clusters should be interpreted with caution and could currently not be attributed to be specifically evoked by cbTMS (Gassmann et al., 2022). Moreover, when delivering the occipital control condition, a long-lasting right occipital positive cluster in an overlapping time-window was observed, bearing resemblance to the positive late cluster when delivering cbTMS with an upward induced current (Figure 14) (Gassmann et al., 2022). This resemblance is also observed in the source analysis results (Figure 29, Figure 30) (Gassmann et al., 2022). An alternative interpretation of this finding would be that these clusters represent posterior muscle artefacts (Gassmann et al., 2022). But this is unlikely, as at the site of TMS, there were no posterior neck muscles in the occipital control condition, but the positive cluster was still observed (Gassmann et al., 2022). Instead, this response likely reflects concomitant activation of the posterior-inferior occipital cortex located in close proximity to the cerebellar target, as also indicated by the electric field simulation results (Figure 9) (Gassmann et al., 2022).

4.2.1.4 Occipital TEPs

The occipital control condition elicited a localized response in an early time-window from 20-45 ms post-TMS, followed by a late, long-lasting positive deflection in electrodes over the targeted right occipital cortex (Figure 14) (Gassmann et al., 2022). These clusters bore resemblance to the right occipital positive deflections observed when delivering cbTMS with an upward induced current and occurred in overlapping time-windows (Figure 22) (Gassmann et al., 2022). This localized EEG response (Gassmann et al., 2022) was largely reproducing previous studies with the same target over the occipital cortex (Garcia et al., 2011). Consequently, these positive deflections are most likely because of concomitant TMS to the occipital cortex, which occurred due to the high TMS intensities utilized to reach the cerebellar cortex with sufficient electric field strength (Gassmann et al., 2022). These observations, especially in combination with the findings of the electric field simulation (Figure 9) and source analysis results (Figure 29, Figure 30) (Gassmann et al., 2022), demonstrated the importance of accounting for the possible confounding factor of concomitant TMS to the occipital cortex in this exploratory study. Importantly, in contrast to cbTMS, TMS to the occipital cortex elicited no EEG responses in frontal brain regions (Gassmann et al., 2022).

4.2.1.5 Effect of current orientation on cbTMS

Delivering cbTMS with a downward induced current largely reproduced TEP results observed when delivering cbTMS with an upward induced current (Gassmann et al., 2022). The main difference was observed in the configuration of the cb-N45 and in a lack of right occipital positive clusters (Figure 18) (Gassmann et al., 2022). A possible explanation for the slightly different configuration of the cb-N45 would be that different neuronal populations were targeted by TMS because of the different directionality of the electric field. The lack of the localized right occipital clusters may be explained by the occipital cortex not being targeted effectively in this condition.

4.2.2 Modulation of the cb-P25 response in a post-stroke-patient with an asymmetry between left and right DTC

The cbTMS method was applied to one post-stroke patient (see 2.2.1) with an asymmetry in the DTC (see 3.2.2) and a delayed-onset hemichoreatic and hemiataxic syndrome (see 3.2.1) (Gassmann et al., 2023a). Reconstructing the DTC utilizing DTI tractography and an anatomical MRI, a pronounced asymmetry between left and right DTC was found (Figure 37), matching the observed clinical syndrome in the clinical assessment before measurements and in the medical history of the patient (see 2.2.1) (Gassmann et al., 2023a). This provided converging evidence for the degeneration of the left DTC (Gassmann et al., 2023a), as this tract has been described as being symmetrical in healthy subjects (Schulz et al., 2015).

Nonetheless, when assessing the brain lesion before our measurements in the T1-weighted MRI, 36 months post-stroke, it did not encompass the ventralis intermedius nucleus of the thalamus (Gassmann et al., 2023a). Instead, the lesion affected the thalamic pulvinar (Gassmann et al., 2023a). Connectional diaschisis could explain the structural impairment of the left DTC, as the thalamic pulvinar is connected to the contralateral cerebellum (Gassmann et al., 2023a). The delayed onset and progression of the clinical syndrome substantiates this interpretation further (Gassmann et al., 2023a). Initially, the clinical syndrome involved left-sided hemianesthesia and hemiparesis (Gassmann et al., 2023a). Over the course of several months, a delayed-onset hemichoreatic and hemiataxic syndrome developed and progressed (Gassmann et al., 2023a). Consequently, secondary neurodegeneration may be the underlying mechanism.

For the comparison of EEG responses to cbTMS to the right and left cerebellar hemisphere, only EEG responses observed before 60 ms post-cbTMS were considered as being specific to cbTMS due to the reasons enumerated above, and since no SHAM-MS was delivered to the patient (see 4.2.1.2) (Gassmann et al., 2023a). The decision to not apply a SHAM-MS was made to reduce the length of the experiment, since it could be shown that for the early cb-P25 and cb-N45 response, a subtraction of SHAM-MS was not necessary (see 4.2.1.1) (Gassmann et al., 2022).

The statistical comparison of EEG responses between cbTMS to the left and right cerebellar hemisphere yielded a significant difference with a large effect size (Cohen's d) in frontal electrodes located contralaterally to cbTMS (Figure 38D) (Gassmann et al., 2023a), resembling the cb-P25 observed in resting state experiments (Figure 22) (Gassmann et al., 2022). Otherwise, no significant differences were observed (Gassmann et al., 2023a).

When discussing the differences in EEG responses between left and right cbTMS, it was paramount to assess whether these differences may have been conceived by a difference in electric field strength or distribution being applied.

The simulated electric field generated by cbTMS indicated comparability in electric field strength and distribution between left and right cbTMS (Figure 38B) (Gassmann et al., 2023a). Moreover, the amplitudes of the fronto-central N100 component were comparable as well (Figure 38E-F) (Gassmann et al., 2023a). As the N100 EEG response has been described to be elicited by unspecific sensory input (Conde et al., 2019, Gordon et al., 2018, Gordon et al., 2021), and was observed as an unspecific EEG response to SHAM-MS in resting state as well (see 4.2.1.2) (Gassmann et al., 2022), this finding provided further evidence for comparable sensory input (Gassmann et al., 2023a). The CBI results provided indirect evidence for a sufficient electric field strength reaching the cerebellar cortex (Gassmann et al., 2023a). In conclusion, these findings were converging evidence that comparably effective cbTMS was delivered to either side.

Moreover, a possible difference in data analysis and processing as a possible confounding factor for the observed differences between left and right cbTMS had to be considered. This possible confounding factor was addressed by blinding the examiner to the origin of the datasets when processing the data (Gassmann et al., 2023a).

Consequently, the most salient interpretation for the observed absence of the cb-P25 response in this patient when delivering cbTMS to the left cerebellar hemisphere was the structural impairment of the DTC on one side (Gassmann et al., 2023a). In contrast, cbTMS to the structurally intact DTC reproduced the cb-P25 observed in resting state (Gassmann et al., 2023a).

4.2.3 cbTMS-specific oscillatory responses in EEG: high beta

In the following, the oscillatory responses to cbTMS and the control conditions in the respective frequency bands will be discussed for the resting state experiments (see 2.1.10.3) (Gassmann et al., 2022). As a main finding, the oscillatory response in the high beta band, located in contralateral electrodes over the prefrontal cortex remained specific to cbTMS (Gassmann et al., 2022). Due to the lack of a SHAM-MS condition when testing the cbTMS protocol in the post-stroke patient (see 2.2), no TFR were calculated for the patient (Gassmann et al., 2023a).

4.2.3.1 Theta band

Oscillatory responses in the theta band were observed in the conditions involving cbTMS in this study, irrespective of current directionality, and significantly different from SHAM-MS (Figure 20, Figure 25) (Gassmann et al., 2022). However, changes in the theta band were found after unspecific sensory stimuli in previous studies, irrespective of stimulus modality, and the power of induced theta increased with stimulation intensity (Michail et al., 2016). When inspecting the oscillatory response to SHAM-MS in this study, an early theta increase with a similar spatial distribution as in the REAL could be observed across conditions (Figures 15, 19, 24) (Gassmann et al., 2022). While an early theta cluster significantly different from SHAM-MS was still found in conditions involving cbTMS (Figure 20, Figure 25), this most likely represents a minor difference in sensory input, with it having been higher when delivering cbTMS, as this theta response was present across all SHAM-MS conditions (Figures 15, 19, 24) (Gassmann et al., 2022). Gordon et al. indicated that oscillatory responses in the theta band may be attributable to cortical responses to unspecific sensory input (Gordon et al., 2021). Still, some previous studies have attributed a theta response specifically to cbTMS (Du et al., 2018, Schutter and van Honk, 2006). In light of the observations in the current study, which involved a SHAM-MS providing sensory input more comparable to cbTMS, this interpretation was deemed erroneous (Gassmann et al., 2022). Observed changes in the theta band were not specifically evoked by cbTMS (Gassmann et al., 2022).

4.2.3.2 Gamma band

Shortly after the cbTMS pulse was delivered, significant increases in gamma power, low and high, were observed irrespective of current directionality (Figure 20, Figure 25) (Gassmann et al., 2022). Similar oscillatory responses in the gamma band were described and modulated in previous TMS-EEG studies

(Rosanova et al., 2009, Chung et al., 2015, Rogasch et al., 2015). A similar gamma increase was also observed when delivering the occipital control condition and the SHAM-MS in the current study (Figures 15, 19, 24) (Gassmann et al., 2022). Consequently, these increases in gamma power were interpreted to likely be an unspecific oscillatory cortical response to multimodal sensory input (Gassmann et al., 2022). Generally, caution is advised when interpreting oscillatory responses in the high frequency gamma band when delivering cbTMS, given the risk of contaminating the oscillatory response with cranial muscle activity, which is regularly elicited by the cbTMS pulse (Fernandez et al., 2021). Consequently, gamma responses could not be specifically attributed to cbTMS (Gassmann et al., 2022).

4.2.3.3 Alpha band

A late decrease in alpha power was observed when subtracting SHAM-MS from REAL ~300 ms post-cbTMS (Figure 19, Figure 24) (Gassmann et al., 2022). This oscillatory response has been observed in previous studies, being described as a response specific to TMS to the primary motor cortex and indicating an activation of tracts to the primary somatosensory cortex (Fecchio et al., 2017). Nonetheless, SHAM-MS elicited a decrease in alpha power in the current study (Figures 15, 19, 24) (Gassmann et al., 2022). Therefore, the decrease in alpha power could not be attributed to be specifically elicited by cbTMS (Gassmann et al., 2022).

4.2.3.4 Beta band

Oscillatory responses in the beta band were observed in the occipital control condition (Figure 16) (Gassmann et al., 2022). This high beta power increase was located at the site of TMS in the occipital control condition (Figure 16) (Gassmann et al., 2022). A similar right occipital increase in high beta power could be observed when delivering cbTMS of either directionality, likely indicating a localized oscillatory response due to concomitant TMS to the posterior-inferior occipital cortex (Figure, 20, Figure 25) (Gassmann et al., 2022). However, most notably, cbTMS of either directionality also elicited a specific increase in high beta power contralaterally to the site of cbTMS in electrodes over the prefrontal cortex (Figure 20, Figure 25) (Gassmann et al., 2022). This increase in high beta power has not been observed in control conditions and was reproducible across the two experiments in resting state (Figure 25) (Gassmann et al., 2022). Hence, this finding was interpreted as a direct and specific oscillatory response to TMS to the cerebellar cortex, which was projected through the DTC to prefrontal areas in the contralateral cerebral cortex (Gassmann et al., 2022). This suggests oscillatory coupling in the beta frequency range between the cerebellar cortex with contralateral prefrontal areas (Gassmann et al., 2022).

Oscillations in the beta band have been associated with sensorimotor function and motor control – during postural maintenance, cerebellar involvement and high beta power have been observed (Kilavik et al., 2013, Takakusaki, 2017, Ioffe et al., 2007). In networks between cerebellar and cerebral cortex, synchronization in the beta frequency band was described in a network between frontal, temporal and cerebellar regions when performing task involving the learning of motor rhythms (Edagawa and Kawasaki, 2017). Also, local beta oscillations in the cerebellar cortex were previously observed and interpreted to have been elicited by activity of Golgi and granule cells (De Zeeuw et al., 2008). As these local oscillations were associated with communication between cerebral cortex and cerebellar cortex during active movements and sensorimotor processing (De Zeeuw et al., 2008), these previous observations provide further substantiation for the idea that cerebral and cerebellar cortex communicate in the beta frequency range.

Consequently, the early increase in high beta power in electrodes over the prefrontal cortex contralateral to the site of cbTMS represents a specific oscillatory response to cbTMS, and may indicate communication between cerebellar and cerebral cortex in the beta frequency range (Gassmann et al., 2022).

4.2.4 Electric field simulation

The results of the simulation of the electric field generated by cbTMS provided important additional information about the target of cbTMS. The investigation and interpretation of the true target in the cerebellar cortex in this study allowed for providing possible explanations for the specific responses to cbTMS that were observed (see 4.2.1, see 4.2.3) (Gassmann et al., 2022).

The electric field generated by cbTMS was broad, indicating comparability of neuronal populations being targeted across subjects (Gassmann et al., 2022). When inspecting the results of the electric field simulation, the peak in electric field strength when delivering cbTMS was observed over the right lateral cerebellar hemisphere, around Crura 1 and 2 (Figure 9) (Gassmann et al., 2022). Crura 1 and 2 have been found to be linked to fronto-parietal and dorsolateral prefrontal regions in the cerebral cortex (D'Angelo, 2018). This may explain why the cbTMS-specific responses (see 4.2.1, see 4.2.3) were located contralaterally and in electrodes over prefrontal and fronto-parietal areas (Gassmann et al., 2022). Also, a relevant part of the electric field was reaching inferior-posterior parts of the occipital cortex (Gassmann et al., 2022), which are topographically closely located to the cerebellar cortex (Figure 9). This was interpreted to demonstrate the necessity of applying an occipital control condition when aiming at identifying specific EEG markers of cbTMS (Gassmann et al., 2022).

The average peak electric field strength generated over the cerebellar cortex by cbTMS was higher than the average peak electric field strength over the primary motor cortex when delivering TMS at RMT intensity (Figure 9) (Gassmann et al., 2022). By definition, TMS at RMT intensity over the primary motor cortex is capable of depolarizing neurons and eliciting an MEP (Rossini et al., 2015). This provided evidence that the electric field generated by cbTMS over the cerebellar cortex was strong enough to depolarize neuronal populations (Gassmann et al., 2022). However, no minimum electric field strength to depolarize neurons in the cerebellar cortex has yet been defined.

4.3 Outlook

Probing cerebellar-to-cerebrum functional connectivity *in vivo* with cbTMS-EEG can enhance our understanding of cerebellar neurophysiology and consequently, cerebellar disorders.

By applying adequate control conditions and confirming effective cbTMS, specific EEG markers of cbTMS could be identified – the cb-P25 and cb-N45 potentials and a contralateral increase in high beta power (Gassmann et al., 2022). These findings may be tested further to eventually serve as biomarkers to probe the structural integrity of the DTC.

While broad targeting of the cerebellar cortex may have the benefit of comparatively simple clinical adaption, the targeting of the cerebellar cortex with the state-of-the-art anatomical surface target across studies remains suboptimal. The true target in the cerebellar cortex may vary as a result, due to differences in coil geometry depending on the coil utilized to deliver cbTMS and individual anatomical differences. EEG responses to cbTMS may vary across studies as a result, as the distribution and strength of the electric field generated in the cerebellar cortex is varying when different TMS coils are utilized. A solution to this challenge could be online electric field estimation, performed simultaneously with neuronavigation-targeted TMS. This method has been applied in the cerebral cortex (Sollmann et al., 2021). Unfortunately, commercial systems to apply this method in the cerebellar cortex are not yet available (Sollmann et al., 2021). Once developed, this method could enable to accurately assess distribution and strength of the electric field being delivered over the functional modules of the cerebellar cortex, reducing variability.

Another future application of cbTMS-EEG would be to test the influence of behavioral tasks on the EEG response to cbTMS - leveraging the high temporal resolution of EEG, and the possibility to interfere with ongoing processes in the cerebellar cortex via TMS.

Moreover, pharmaco-cbTMS-EEG could be applied to test whether the observed EEG responses reflect excitation or inhibition. This method has been performed with TMS-EEG to the primary motor cortex, where it was demonstrated that antiglutamatergic (Belardinelli et al., 2021) and GABAAergic drugs (Premoli et al., 2014) contribute in regulating the N45 amplitude.

Testing the identified EEG markers in a post-stroke patient with a delayed-onset hemiataxic and hemichoreatic syndrome and an asymmetry of the DTC provided a starting point for clinical trials. Future research is needed, testing the method in clinical populations. Future studies may test the observed EEG markers in patients with neurodegenerative diseases, for example, in patients with spinocerebellar ataxias, or in patients with a structural impairment of the DTC, for example, stroke patients.

4.4 Conclusion

In this study, modelling of the generated electric field of cbTMS and the assessment of CBI provided converging evidence for effective cbTMS (Gassmann et al., 2022). By applying novel control conditions, it was possible to identify specific EEG responses to cbTMS in resting state (Gassmann et al., 2022). Namely, the cb-P25, the cb-N45 and a contralateral prefrontal increase in high beta oscillatory power were identified (Gassmann et al., 2022). These responses proved reproducible across two resting state experiments (Gassmann et al., 2022).

Anatomical considerations (see 4.2.1.1) lead to the interpretation, that cb-P25 and cb-N45 reflect an activation of the cerebellar cortex with subsequent probing of the DTC (Gassmann et al., 2022). The observed increase in high beta power was interpreted to reflect a response to cbTMS being projected through the DTC to the contralateral prefrontal cortex – possibly indicating oscillatory coupling of these regions in the beta band (Gassmann et al., 2022).

Additionally to resting state experiments, these EEG responses specific to cbTMS were tested in one post-stroke patient with a delayed-onset hemiataxic and hemichoreatic clinical syndrome and an asymmetry of the DTC (Gassmann et al., 2023a). When applying cbTMS-EEG to this patient, cb-P25 was reproduced on the intact side, while it was absent on the structurally impaired side (Gassmann et al., 2023a). This clinical case provided a starting point for future studies aiming to probe the structural integrity of cerebellum-to-cerebrum connectivity via cbTMS.

In summary, the identified specific EEG responses may eventually be utilized as biomarkers for the structural integrity of the DTC.

5 Summary

Cerebellum-to-cerebrum functional connectivity can indirectly be assessed with transcranial magnetic stimulation (TMS) combined with electromyography by applying the cerebellar brain inhibition (CBI) procedure, measuring a suppression of motor evoked potential (MEP) amplitude in hand muscles. Consequently, this output is limited to the primary motor cortex and, depending on cortical excitability, MEP amplitudes show high variability. As TMS combined with electroencephalography (EEG) could address these limitations, feasibility studies were conducted recently. Several challenges have so far precluded the identification of EEG markers elicited by cerebellar TMS (cbTMS) - a lack of control conditions for sensory-evoked EEG potentials and concomitant occipital cortex stimulation. Hence, the objective of the present study was the identification of specific EEG responses to cbTMS.

46 healthy volunteers completed two resting state experiments. To confirm cbTMS was effectively delivered to the cerebellar cortex, CBI was assessed individually to determine cbTMS intensity. A model of the cbTMS coil was created utilizing radiography of the coil and individual magnetic resonance imaging (MRI) scans from 8 randomly selected participants to simulate the electric field generated by cbTMS. Control conditions adapted for cbTMS were applied. By performing cluster-based permutation t-statistics, specific EEG responses could be identified - the cb-P25 and cb-N45. EEG responses were projected into the source space. By performing time-frequency analysis, a specific increase in left prefrontal high beta power was observed. The method was applied in a post-stroke patient with delayed-onset hemiataxia. An MRI scan and diffusion tensor imaging tractography were acquired, demonstrating an asymmetry between left and right dentato-thalamo-cortical tract (DTC). cb-P25 was absent on the structurally impaired side and reproduced on the intact side.

Applying a novel method, specific EEG responses to cbTMS could be identified. These responses were interpreted to reflect effective connectivity between cerebellum and cerebral cortex mediated by the DTC. The cbTMS-EEG technique could test pathology of the DTC, as demonstrated in one patient with neurodegeneration of the DTC on one side.

5.1 Zusammenfassung

Mittels cerebellärer inhibierender Konditionierung (eng. cerebellar brain inhibition, CBI) ist eine indirekte Messung funktioneller Konnektivität zwischen cerebellärem und cerebralem Kortex möglich. Dabei wird eine Amplitudenminderung der motorisch-evozierten Potentiale (MEP) in Handmuskeln gemessen. Folglich kann nur die Auswirkung cerebellärer Konditionierung auf den primären Motorkortex erfasst werden. Darüber hinaus sind MEP-Amplituden hochvariabel, abhängig von der kortikalen Erregbarkeit und der dynamischen Hirnaktivität zum Zeitpunkt der transkraniellen Magnetstimulation (TMS). Diese Limitationen könnten mittels einer Kombination der cerebellären TMS (cbTMS) mit Elektroenzephalographie (EEG) adressiert werden, weswegen kürzlich Studien zur Realisierbarkeit von cbTMS-EEG veröffentlicht wurden. Das Fehlen spezifischer Kontrollkonditionen – für eine zeitliche Überlappung mit sensorisch-evozierten Potenzialen (SEP) und einer möglichen Begleitstimulation des Okzipitalkortex – verhindern die Identifikation spezifischer EEG-Marker. Dementsprechend war das Ziel der durchgeführten Studie die Identifikation cbTMS-spezifischer EEG-Marker.

46 gesunde Freiwillige durchliefen zwei Experimente im Ruhezustand (eng. resting state). Um die korrekte Stimulatorleistung zur Generierung eines adäquaten elektrischen Feldes im cerebellären Kortex zu ermitteln, wurde für jeden Probanden die CBI ermittelt. Außerdem wurde eine Simulation des generierten elektrischen Feldes der verwendeten Spule erstellt, auf Basis eines konventionellen Röntgens der Spule und 8 Schädel-Magnetresonanztomographien (cMRT) zufällig ausgewählter Probanden. Die spezifischen Kontrollkonditionen wurden durchgeführt. Die statistische Auswertung mittels clusterbasierter Permutationsverfahren ergab spezifische EEG-Marker der cbTMS – das cb-P25 und cb-N45. Die EEG-Signale wurden in ein Voxelmodell des menschlichen Gehirns projiziert. Eine Zeit-Frequenz-Analyse (engl. time-frequency analysis, TFR) wurde durchgeführt, in welcher eine spezifische Erhöhung der links-präfrontalen beta-Oszillationen beobachtet wurde.

Anschließend wurde die Methode an einem Patienten erprobt, der 36 Monate zuvor einen Apoplex erlitten hatte und eine verzögert eingetretene Hemiataxie zeigte. Ein cMRT und eine Diffusions-Tensor-Bildgebung (DTI) mit Traktographie wurden durchgeführt, in welcher eine Asymmetrie zwischen rechtem und linkem dentato-thalamo-kortikalem Trakt (DTC) gezeigt werden konnte. cb-P25 war nur auf der intakten Seite reproduzierbar.

Mittels einer neuartigen Methode konnten spezifisch durch cbTMS evozierte EEG-Marker identifiziert werden. Diese wurden als Marker der effektiven Konnektivität zwischen Cerebellum und Cerebrum mittels des DTC interpretiert. Die Methode der cbTMS-EEG könnte als Test auf Pathologien des DTC angewandt werden – wie durch ihre Anwendung an einem Patienten mit Neurodegeneration des DTC auf einer Seite gezeigt werden konnte.

Ort/Datum Unterschrift Doktorand (Lukas Gaßmann)

Ort/Datum Unterschrift Betreuer (Prof. Dr. Ulf Ziemann)

6 Literature

AHN, S. & FROHLICH, F. 2021. Pinging the brain with transcranial magnetic stimulation reveals cortical reactivity in time and space. *Brain Stimul,* 14**,** 304-315.

BELARDINELLI, P., BIABANI, M., BLUMBERGER, D. M., BORTOLETTO, M., CASAROTTO, S., DAVID, O., DESIDERI, D., ETKIN, A., FERRARELLI, F., FITZGERALD, P. B., FORNITO, A., GORDON, P. C., GOSSERIES, O., HARQUEL, S., JULKUNEN, P., KELLER, C. J., KIMISKIDIS, V. K., LIOUMIS, P., MINIUSSI, C., ROSANOVA, M., ROSSI, S., SARASSO, S., WU, W., ZRENNER, C., DASKALAKIS, Z. J., ROGASCH, N. C., MASSIMINI, M., ZIEMANN, U. & ILMONIEMI, R. J. 2019. Reproducibility in TMS-EEG studies: A call for data sharing, standard procedures and effective experimental control. *Brain Stimul,* 12**,** 787-790.

BELARDINELLI, P., KONIG, F., LIANG, C., PREMOLI, I., DESIDERI, D., MULLER-DAHLHAUS, F., GORDON, P. C., ZIPSER, C., ZRENNER, C. & ZIEMANN, U. 2021. TMS-EEG signatures of glutamatergic neurotransmission in human cortex. *Sci Rep,* 11**,** 8159.

BIABANI, M., FORNITO, A., MUTANEN, T. P., MORROW, J. & ROGASCH, N. C. 2019. Characterizing and minimizing the contribution of sensory inputs to TMS-evoked potentials. *Brain Stimul,* 12**,** 1537-1552.

BONFERRONI, C. E. 1936. Teoria statistica delle classi e calcolo delle probabilità*,* Seeber, Florence.

BUCKNER, R. L., KRIENEN, F. M., CASTELLANOS, A., DIAZ, J. C. & YEO, B. T. 2011. The organization of the human cerebellum estimated by intrinsic functional connectivity. *J Neurophysiol,* 106**,** 2322-2345.

CAN, M. K., LAAKSO, I., NIEMINEN, J. O., MURAKAMI, T. & UGAWA, Y. 2019. Coil model comparison for cerebellar transcranial magnetic stimulation. *Biomedical Physics & Engineering Express,* 5, 015020.

CHUNG, S. W., ROGASCH, N. C., HOY, K. E. & FITZGERALD, P. B. 2015. Measuring Brain Stimulation Induced Changes in Cortical Properties Using TMS-EEG. *Brain Stimul,* 8**,** 1010-1020.

CLOWER, D. M., DUM, R. P. & STRICK, P. L. 2005. Basal ganglia and cerebellar inputs to 'AIP'. *Cereb Cortex,* 15**,** 913-920.

CONDE, V., TOMASEVIC, L., AKOPIAN, I., STANEK, K., SATURNINO, G. B., THIELSCHER, A., BERGMANN, T. O. & SIEBNER, H. R. 2019. The non-transcranial TMS-evoked potential is an inherent source of ambiguity in TMS-EEG studies. *Neuroimage,* 185**,** 300-312.

CURY, R. G., FRANCA, C., REIS BARBOSA, E., JACOBSEN TEIXEIRA, M. & CIAMPI DE ANDRADE, D. 2020. Little Brain, Big Expectations. *Brain Sci,* 10, 944.

D'ANGELO, E. 2018. Chapter 6: Physiology of the cerebellum. *Handbook of Clinical Neurology Series,* 154**,** 85-108, Elsevier, Amsterdam.

D'ANGELO, E. & CASALI, S. 2012. Seeking a unified framework for cerebellar function and dysfunction: from circuit operations to cognition. *Front Neural Circuits,* 6**,** 116.

DE GENNARO, L., CRISTIANI, R., BERTINI, M., CURCIO, G., FERRARA, M., FRATELLO, F., ROMEI, V. & ROSSINI, P. M. 2004. Handedness is mainly associated with an asymmetry of corticospinal excitability and not of transcallosal inhibition. *Clin Neurophysiol,* 115**,** 1305-1312.

DE ZEEUW, C. I., HOEBEEK, F. E. & SCHONEWILLE, M. 2008. Causes and consequences of oscillations in the cerebellar cortex. *Neuron,* 58**,** 655-658.

DU, X., CHOA, F. S., SUMMERFELT, A., ROWLAND, L. M., CHIAPPELLI, J., KOCHUNOV, P. & HONG, L. E. 2017. N100 as a generic cortical electrophysiological marker based on decomposition of TMS-evoked potentials across five anatomic locations. *Exp Brain Res,* 235**,** 69-81.

DU, X., ROWLAND, L. M., SUMMERFELT, A., CHOA, F. S., WITTENBERG, G. F., WISNER, K., WIJTENBURG, A., CHIAPPELLI, J., KOCHUNOV, P. & HONG, L. E. 2018. Cerebellar-Stimulation Evoked Prefrontal Electrical Synchrony Is Modulated by GABA. *Cerebellum,* 17**,** 550-563.

DUM, R. P. & STRICK, P. L. 2003. An unfolded map of the cerebellar dentate nucleus and its projections to the cerebral cortex. *J Neurophysiol,* 89**,** 634-639.

DWORKIN, R. H., TURK, D. C., WYRWICH, K. W., BEATON, D., CLEELAND, C. S., FARRAR, J. T., HAYTHORNTHWAITE, J. A., JENSEN, M. P., KERNS, R. D., ADER, D. N., BRANDENBURG, N., BURKE, L. B., CELLA, D., CHANDLER, J., COWAN, P., DIMITROVA, R., DIONNE, R., HERTZ, S., JADAD, A. R., KATZ, N. P., KEHLET, H., KRAMER, L. D., MANNING, D. C., MCCORMICK, C., MCDERMOTT, M. P., MCQUAY, H. J., PATEL, S., PORTER, L., QUESSY, S., RAPPAPORT, B. A., RAUSCHKOLB, C., REVICKI, D. A., ROTHMAN, M., SCHMADER, K. E., STACEY, B. R., STAUFFER, J. W., VON STEIN, T., WHITE, R. E., WITTER, J. & ZAVISIC, S. 2008. Interpreting the clinical importance of treatment outcomes in chronic pain clinical trials: IMMPACT recommendations. *J Pain,* 9**,** 105-121.

EDAGAWA, K. & KAWASAKI, M. 2017. Beta phase synchronization in the frontal-temporal-cerebellar network during auditory-to-motor rhythm learning. *Sci Rep,* 7**,** 42721.

ESSER, S. K., HUBER, R., MASSIMINI, M., PETERSON, M. J., FERRARELLI, F. & TONONI, G. 2006. A direct demonstration of cortical LTP in humans: a combined TMS/EEG study. *Brain Res Bull,* 69**,** 86-94.

FABER, J., GIORDANO, I., JIANG, X., KINDLER, C., SPOTTKE, A., ACOSTA-CABRONERO, J., NESTOR, P. J., MACHTS, J., DÜZEL, E., VIELHABER, S., SPECK, O., DUDESEK, A., KAMM, C., SCHEEF, L. & KLOCKGETHER, T. 2020. Prominent White Matter Involvement in Multiple System Atrophy of Cerebellar Type. *Mov Disord,* 35**,** 816-824.

FECCHIO, M., PIGORINI, A., COMANDUCCI, A., SARASSO, S., CASAROTTO, S., PREMOLI, I., DERCHI, C. C., MAZZA, A., RUSSO, S., RESTA, F., FERRARELLI, F., MARIOTTI, M., ZIEMANN, U., MASSIMINI, M. & ROSANOVA, M. 2017. The spectral features of EEG responses to transcranial magnetic stimulation of the primary motor cortex depend on the amplitude of the motor evoked potentials. *PLoS One,* 12**,** e0184910.

FERNANDEZ, L., BIABANI, M., DO, M., OPIE, G. M., HILL, A. T., BARHAM, M. P., TEO, W. P., BYRNE, L. K., ROGASCH, N. C. & ENTICOTT, P. G. 2021. Assessing cerebellar-cortical connectivity using concurrent TMS-EEG: a feasibility study. *J Neurophysiol,* 125**,** 1768-1787.

FERNANDEZ, L., MAJOR, B. P., TEO, W. P., BYRNE, L. K. & ENTICOTT, P. G. 2018. Assessing cerebellar brain inhibition (CBI) via transcranial magnetic stimulation (TMS): A systematic review. *Neurosci Biobehav Rev,* 86**,** 176-206.

FONG, P. Y., SPAMPINATO, D., MICHELL, K., MANCUSO, M., BROWN, K., IBANEZ, J., SANTO, A. D., LATORRE, A., BHATIA, K., ROTHWELL, J. C. & ROCCHI, L. 2023. EEG responses induced by cerebellar TMS at rest and during visuomotor adaptation. *Neuroimage,* 275**,** 120188.

FRANCA, C., DE ANDRADE, D. C., SILVA, V., GALHARDONI, R., BARBOSA, E. R., TEIXEIRA, M. J. & CURY, R. G. 2020. Effects of cerebellar transcranial magnetic stimulation on ataxias: A randomized trial. *Parkinsonism Relat Disord,* 80**,** 1-6.

GARCIA, J. O., GROSSMAN, E. D. & SRINIVASAN, R. 2011. Evoked potentials in large-scale cortical networks elicited by TMS of the visual cortex. *J Neurophysiol,* 106**,** 1734-1746.

GASSMANN, L., GORDON, P. C. & ZIEMANN, U. 2022. Assessing effective connectivity of the cerebellum with cerebral cortex using TMS-EEG. *Brain Stimul*.

GASSMANN, L., GORDON, P. C., ROY, O., KAUT, O., HOMBERG, V. & ZIEMANN, U. 2023a. Cerebellar TMS-EEG in a chronic stroke patient with connectional diaschisis of the dentato-thalamo-cortical tract. *Clin Neurophysiol,* 152**,** 68-70.

GASSMANN, L., GORDON, P. C. & ZIEMANN, U. 2023b. Reflecting the causes of variability of EEG responses elicited by cerebellar TMS. *Neuroimage,* 281**,** 120368.

GORDON, P. C., DESIDERI, D., BELARDINELLI, P., ZRENNER, C. & ZIEMANN, U. 2018. Comparison of cortical EEG responses to realistic sham versus real TMS of human motor cortex. *Brain Stimul,* 11**,** 1322-1330.

GORDON, P. C., JOVELLAR, D. B., SONG, Y., ZRENNER, C., BELARDINELLI, P., SIEBNER, H. R. & ZIEMANN, U. 2021. Recording brain responses to TMS of primary motor cortex by EEG - utility of an optimized sham procedure. *Neuroimage,* 245**,** 118708.

GROPPA, S., OLIVIERO, A., EISEN, A., QUARTARONE, A., COHEN, L. G., MALL, V., KAELIN-LANG, A., MIMA, T., ROSSI, S., THICKBROOM, G. W., ROSSINI, P. M., ZIEMANN, U., VALLS-SOLE, J. & SIEBNER, H. R. 2012. A practical guide to diagnostic transcranial magnetic stimulation: report of an IFCN committee. *Clin Neurophysiol,* 123**,** 858-882.

HAMALAINEN, M. S. & ILMONIEMI, R. J. 1994. Interpreting magnetic fields of the brain: minimum norm estimates. *Med Biol Eng Comput,* 32**,** 35-42.

HARDWICK, R. M., LESAGE, E. & MIALL, R. C. 2014. Cerebellar transcranial magnetic stimulation: the role of coil geometry and tissue depth. *Brain Stimul,* 7**,** 643-649.

ILMONIEMI, R. J. & KICIC, D. 2010. Methodology for combined TMS and EEG. *Brain Topogr,* 22**,** 233-48.

ILMONIEMI, R. J., RUOHONEN, J. & KARHU, J. 1999. Transcranial magnetic stimulation--a new tool for functional imaging of the brain. *Crit Rev Biomed Eng,* 27**,** 241-284.

ILMONIEMI, R. J., VIRTANEN, J., RUOHONEN, J., KARHU, J., ARONEN, H. J., NAATANEN, R. & KATILA, T. 1997. Neuronal responses to magnetic stimulation reveal cortical reactivity and connectivity. *Neuroreport,* 8**,** 3537-3540.

IOFFE, M. E., CHERNIKOVA, L. A. & USTINOVA, K. I. 2007. Role of cerebellum in learning postural tasks. *Cerebellum,* 6**,** 87-94.

JONES, D. K., KNÖSCHE, T. R. & TURNER, R. 2013. White matter integrity, fiber count, and other fallacies: the do's and don'ts of diffusion MRI. *Neuroimage,* 73**,** 239-254.

KAARRE, O., KALLIONIEMI, E., KONONEN, M., TOLMUNEN, T., KEKKONEN, V., KIVIMAKI, P., HEIKKINEN, N., FERRERI, F., LAUKKANEN, E. & MAATTA, S. 2018. Heavy alcohol use in adolescence is associated with altered cortical activity: a combined TMS-EEG study. *Addict Biol,* 23**,** 268-280.

KELLY, R. M. & STRICK, P. L. 2003. Cerebellar loops with motor cortex and prefrontal cortex of a nonhuman primate. *J Neurosci,* 23**,** 8432-8444.

KILAVIK, B. E., ZAEPFFEL, M., BROVELLI, A., MACKAY, W. A. & RIEHLE, A. 2013. The ups and downs of beta oscillations in sensorimotor cortex. *Exp Neurol,* 245**,** 15-26.

KOMSSI, S., KAHKONEN, S. & ILMONIEMI, R. J. 2004. The effect of stimulus intensity on brain responses evoked by transcranial magnetic stimulation. *Hum Brain Mapp,* 21**,** 154-164.

LEHMANN, D. & SKRANDIES, W. 1980. Reference-free identification of components of checkerboard-evoked multichannel potential fields. *Electroencephalogr Clin Neurophysiol,* 48**,** 609-621.

LIOUMIS, P., KICIC, D., SAVOLAINEN, P., MAKELA, J. P. & KAHKONEN, S. 2009. Reproducibility of TMS-Evoked EEG responses. *Hum Brain Mapp,* 30**,** 1387-1396.

LY, J. Q. M., GAGGIONI, G., CHELLAPPA, S. L., PAPACHILLEOS, S., BRZOZOWSKI, A., BORSU, C., ROSANOVA, M., SARASSO, S., MIDDLETON, B., LUXEN, A., ARCHER, S. N., PHILLIPS, C., DIJK, D. J., MAQUET, P., MASSIMINI, M. & VANDEWALLE, G. 2016. Circadian regulation of human cortical excitability. *Nat Commun,* 7**,** 11828.

MARIS, E. & OOSTENVELD, R. 2007. Nonparametric statistical testing of EEG- and MEG-data. *J Neurosci Methods,* 164**,** 177-190.

MASSIMINI, M., FERRARELLI, F., HUBER, R., ESSER, S. K., SINGH, H. & TONONI, G. 2005. Breakdown of cortical effective connectivity during sleep. *Science,* 309**,** 2228-2232.

MATHWORKS 2017. MATLAB version 9.3.0.948333 (R2017b) Update 9. Natick, Massachusetts, United States: The MathWorks Inc.

MICHAIL, G., DRESEL, C., WITKOVSKY, V., STANKEWITZ, A. & SCHULZ, E. 2016. Neuronal Oscillations in Various Frequency Bands Differ between Pain and Touch. *Front Hum Neurosci,* 10**,** 182.

NIELSEN, J. D., MADSEN, K. H., PUONTI, O., SIEBNER, H. R., BAUER, C., MADSEN, C. G., SATURNINO, G. B. & THIELSCHER, A. 2018. Automatic skull segmentation from MR images for realistic volume conductor models of the head: Assessment of the state-of-the-art. *Neuroimage,* 174**,** 587-598.

O'REILLY, J. X., BECKMANN, C. F., TOMASSINI, V., RAMNANI, N. & JOHANSEN-BERG, H. 2010. Distinct and overlapping functional zones in the cerebellum defined by resting state functional connectivity. *Cereb Cortex,* 20**,** 953-965.

OLDFIELD, R. C. 1971. The assessment and analysis of handedness: the Edinburgh inventory. *Neuropsychologia,* 9**,** 97-113.

OOSTENVELD, R., FRIES, P., MARIS, E. & SCHOFFELEN, J. M. 2011. FieldTrip: Open source software for advanced analysis of MEG, EEG, and invasive electrophysiological data. *Comput Intell Neurosci,* 2011**,** 156869.

ORTH, M., AMANN, B., RATNARAJ, N., PATSALOS, P. N. & ROTHWELL, J. C. 2005. Caffeine has no effect on measures of cortical excitability. *Clin Neurophysiol,* 116**,** 308-314.

PALESI, F., DE RINALDIS, A., CASTELLAZZI, G., CALAMANTE, F., MUHLERT, N., CHARD, D., TOURNIER, J. D., MAGENES, G., D'ANGELO, E. & GANDINI WHEELER-KINGSHOTT, C. A. M. 2017. Contralateral cortico-ponto-cerebellar pathways reconstruction in humans in vivo: implications for reciprocal cerebro-cerebellar structural connectivity in motor and non-motor areas. *Sci Rep,* 7**,** 12841.

PALESI, F., TOURNIER, J. D., CALAMANTE, F., MUHLERT, N., CASTELLAZZI, G., CHARD, D., D'ANGELO, E. & WHEELER-KINGSHOTT, C. A. 2015. Contralateral cerebello-thalamo-cortical pathways with prominent involvement of associative areas in humans in vivo. *Brain Struct Funct,* 220**,** 3369-3384.

PARKER, K. L., NARAYANAN, N. S. & ANDREASEN, N. C. 2014. The therapeutic potential of the cerebellum in schizophrenia. *Front Syst Neurosci,* 8**,** 163.

PELLICCIARI, M. C., VENIERO, D. & MINIUSSI, C. 2017. Characterizing the Cortical Oscillatory Response to TMS Pulse. *Front Cell Neurosci,* 11**,** 38.

PREMOLI, I., CASTELLANOS, N., RIVOLTA, D., BELARDINELLI, P., BAJO, R., ZIPSER, C., ESPENHAHN, S., HEIDEGGER, T., MULLER-DAHLHAUS, F. & ZIEMANN, U. 2014. TMS-EEG signatures of GABAergic neurotransmission in the human cortex. *J Neurosci,* 34**,** 5603-12.

ROCCHI, L., DI SANTO, A., BROWN, K., IBANEZ, J., CASULA, E., RAWJI, V., DI LAZZARO, V., KOCH, G. & ROTHWELL, J. 2021. Disentangling EEG responses to TMS due to cortical and peripheral activations. *Brain Stimul,* 14**,** 4-18.

ROCCHI, L., SPAMPINATO, D. A., PEZZOPANE, V., ORTH, M., BISIACCHI, P. S., ROTHWELL, J. C. & CASULA, E. P. 2023. Cerebellar noninvasive neuromodulation influences the reactivity of the contralateral primary motor cortex and surrounding areas: a TMS-EMG-EEG study. *Cerebellum,* 22**,** 319-331.

ROGASCH, N. C., DASKALAKIS, Z. J. & FITZGERALD, P. B. 2015. Cortical inhibition of distinct mechanisms in the dorsolateral prefrontal cortex is related to working memory performance: a TMS-EEG study. *Cortex,* 64**,** 68-77.

ROGASCH, N. C., SULLIVAN, C., THOMSON, R. H., ROSE, N. S., BAILEY, N. W., FITZGERALD, P. B., FARZAN, F. & HERNANDEZ-PAVON, J. C. 2017. Analysing concurrent transcranial magnetic stimulation and electroencephalographic data: A review and introduction to the open-source TESA software. *Neuroimage,* 147**,** 934-951.

ROGASCH, N. C., THOMSON, R. H., FARZAN, F., FITZGIBBON, B. M., BAILEY, N. W., HERNANDEZ-PAVON, J. C., DASKALAKIS, Z. J. & FITZGERALD, P. B. 2014. Removing artefacts from TMS-EEG recordings using independent component analysis: importance for assessing prefrontal and motor cortex network properties. *Neuroimage,* 101**,** 425-439.

ROSANOVA, M., CASALI, A., BELLINA, V., RESTA, F., MARIOTTI, M. & MASSIMINI, M. 2009. Natural frequencies of human corticothalamic circuits. *J Neurosci,* 29**,** 7679-7685.

ROSS, J. M., SARKAR, M. & KELLER, C. J. 2022. Experimental suppression of transcranial magnetic stimulation-electroencephalography sensory potentials. *Hum Brain Mapp,* 43**,** 5141-5153.

ROSSI, S., ANTAL, A., BESTMANN, S., BIKSON, M., BREWER, C., BROCKMOLLER, J., CARPENTER, L. L., CINCOTTA, M., CHEN, R., DASKALAKIS, J. D., DI LAZZARO, V., FOX, M. D., GEORGE, M. S., GILBERT, D., KIMISKIDIS, V. K., KOCH, G., ILMONIEMI, R. J., PASCAL LEFAUCHEUR, J., LEOCANI, L., LISANBY, S. H., MINIUSSI, C., PADBERG, F., PASCUAL-LEONE, A., PAULUS, W., PETERCHEV, A. V., QUARTARONE, A., ROTENBERG, A., ROTHWELL, J., ROSSINI, P. M., SANTARNECCHI, E., SHAFI, M. M., SIEBNER, H. R., UGAWA, Y., WASSERMANN, E. M., ZANGEN, A., ZIEMANN, U., HALLETT, M. & BASIS OF THIS ARTICLE BEGAN WITH A CONSENSUS STATEMENT FROM THE IFCN WORKSHOP ON "PRESENT, F. O. T. M. S. S. E. G. S. O. U. T. A. 2021. Safety and recommendations for TMS use in healthy subjects and patient populations, with updates on training, ethical and regulatory issues: Expert Guidelines. *Clin Neurophysiol,* 132**,** 269-306.

ROSSINI, P. M., BURKE, D., CHEN, R., COHEN, L. G., DASKALAKIS, Z., DI IORIO, R., DI LAZZARO, V., FERRERI, F., FITZGERALD, P. B., GEORGE, M. S., HALLETT, M., LEFAUCHEUR, J. P., LANGGUTH, B., MATSUMOTO, H., MINIUSSI, C., NITSCHE, M. A., PASCUAL-LEONE, A., PAULUS, W., ROSSI, S., ROTHWELL, J. C., SIEBNER, H. R., UGAWA, Y., WALSH, V. & ZIEMANN, U. 2015. Non-invasive electrical and magnetic stimulation of the brain, spinal cord, roots and peripheral nerves: Basic principles and procedures for routine clinical and research application. An updated report from an I.F.C.N. Committee. *Clin Neurophysiol,* 126**,** 1071-1107.

SCHILBERG, L., TEN OEVER, S., SCHUHMANN, T. & SACK, A. T. 2021. Phase and power modulations on the amplitude of TMS-induced motor evoked potentials. *PLoS One,* 16**,** e0255815.

SCHMAHMANN, J. D. 2019. The cerebellum and cognition. *Neurosci Lett,* 688**,** 62-75.

SCHMITZ-HUBSCH, T., DU MONTCEL, S. T., BALIKO, L., BERCIANO, J., BOESCH, S., DEPONDT, C., GIUNTI, P., GLOBAS, C., INFANTE, J., KANG, J. S., KREMER, B., MARIOTTI, C., MELEGH, B., PANDOLFO, M., RAKOWICZ, M., RIBAI, P., ROLA, R., SCHOLS, L., SZYMANSKI, S., VAN DE WARRENBURG, B. P., DURR, A., KLOCKGETHER, T. & FANCELLU, R. 2006. Scale for the assessment and rating of ataxia: development of a new clinical scale. *Neurology,* 66**,** 1717-1720.

SCHULZ, R., WESSEL, M. J., ZIMERMAN, M., TIMMERMANN, J. E., GERLOFF, C. & HUMMEL, F. C. 2015. White Matter Integrity of Specific Dentato-Thalamo-Cortical Pathways is Associated with Learning Gains in Precise Movement Timing. *Cereb Cortex,* 25**,** 1707-1714.

SCHUTTER, D. J. & VAN HONK, J. 2006. An electrophysiological link between the cerebellum, cognition and emotion: frontal theta EEG activity to single-pulse cerebellar TMS. *Neuroimage,* 33**,** 1227-1231.

SOLLMANN, N., KRIEG, S. M., SAISANEN, L. & JULKUNEN, P. 2021. Mapping of Motor Function with Neuronavigated Transcranial Magnetic Stimulation: A Review on Clinical Application in Brain Tumors and Methods for Ensuring Feasible Accuracy. *Brain Sci,* 11**,** 897.

SPAMPINATO, D., IBANEZ, J., SPANOUDAKIS, M., HAMMOND, P. & ROTHWELL, J. C. 2020. Cerebellar transcranial magnetic stimulation: The role of coil type from distinct manufacturers. *Brain Stimul,* 13**,** 153-156.

STENROOS, M. & NUMMENMAA, A. 2016. Incorporating and Compensating Cerebrospinal Fluid in Surface-Based Forward Models of Magneto- and Electroencephalography. *PLoS One,* 11**,** e0159595.

STOODLEY, C. J. & SCHMAHMANN, J. D. 2010. Evidence for topographic organization in the cerebellum of motor control versus cognitive and affective processing. *Cortex,* 46**,** 831-844.

TAKAKUSAKI, K. 2017. Functional Neuroanatomy for Posture and Gait Control. *J Mov Disord,* 10**,** 1-17.

TER BRAACK, E. M., DE VOS, C. C. & VAN PUTTEN, M. J. 2015. Masking the Auditory Evoked Potential in TMS-EEG: A Comparison of Various Methods. *Brain Topogr,* 28**,** 520-528.

THIELSCHER, A., ANTUNES, A. & SATURNINO, G. B. 2015. Field modeling for transcranial magnetic stimulation: A useful tool to understand the physiological effects of TMS? *37th Annual International Conference of the IEEE Engineering in Medicine and Biology Society (EMBC)*, Milan, Italy*,* 2015**,** 222-225.

THIELSCHER, A. & KAMMER, T. 2004. Electric field properties of two commercial figure-8 coils in TMS: calculation of focality and efficiency. *Clin Neurophysiol,* 115**,** 1697-1708.

UGAWA, Y., UESAKA, Y., TERAO, Y., HANAJIMA, R. & KANAZAWA, I. 1995. Magnetic stimulation over the cerebellum in humans. *Ann Neurol,* 37**,** 703-713.

VOOGD, J. 2003. The human cerebellum. *J Chem Neuroanat,* 26**,** 243-252.

WEISE, K., NUMSSEN, O., THIELSCHER, A., HARTWIGSEN, G. & KNOSCHE, T. R. 2020. A novel approach to localize cortical TMS effects. *Neuroimage,* 209**,** 116486.

YEH, F. C. 2020. Shape analysis of the human association pathways. *Neuroimage,* 223**,** 117329.

YEH, F. C., PANESAR, S., FERNANDES, D., MEOLA, A., YOSHINO, M., FERNANDEZ-MIRANDA, J. C., VETTEL, J. M. & VERSTYNEN, T. 2018. Population-averaged atlas of the macroscale human structural connectome and its network topology. *Neuroimage,* 178**,** 57-68.

YEH, F. C., VERSTYNEN, T. D., WANG, Y., FERNANDEZ-MIRANDA, J. C. & TSENG, W. Y. 2013. Deterministic diffusion fiber tracking improved by quantitative anisotropy. *PLoS One,* 8**,** e80713.

YEH, F. C., WEDEEN, V. J. & TSENG, W. Y. 2010. Generalized q-sampling imaging. *IEEE Trans Med Imaging,* 29**,** 1626-1635.

ZIEMANN, U., REIS, J., SCHWENKREIS, P., ROSANOVA, M., STRAFELLA, A., BADAWY, R. & MULLER-DAHLHAUS, F. 2015. TMS and drugs revisited 2014. *Clin Neurophysiol,* 126**,** 1847-1868.

ZIJLMANS, J. C. 2011. Vascular chorea in adults and children. *Handb Clin Neurol,* 100**,** 261-270.

7 Erklärungen zum Eigenanteil

Die Arbeit wurde am Hertie-Institut für klinische Hirnforschung und in der Universitätsklinik für Neurologie in der Abteilung Neurologie mit Schwerpunkt neurovaskuläre Erkrankungen unter der Betreuung von Herrn Prof. Dr. Ulf Ziemann durchgeführt.

Die Konzeption der Studie erfolgte in Zusammenarbeit mit Herrn Prof. Dr. Ziemann und Herrn Dr. Pedro Caldana Gordon. Die Erhebung der Daten erfolgte eigenständig durch mich nach kurzer Einarbeitung im Rahmen eines Pilotversuches durch Herrn Dr. Pedro Caldana Gordon. Die Auswertung der erhobenen Daten, inklusive der statistischen Auswertung, sowie die Literaturrecherche erfolgten eigenständig und unter Verwendung selbst geschriebener MATLAB-Codes durch mich, unter Supervision durch Herrn Prof. Dr. Ulf Ziemann und Herrn Dr. Pedro Caldana Gordon. Die für dieses Manuskript erstellten Grafiken wurden durch mich unter Verwendung selbst geschriebener MATLAB-Codes erstellt, bei den in Figure 5 gezeigten 3D-Modellierungen eines Kopfes mit Spulenpositionen unterstützte David Emanuel Vetter anfänglich bei der Modellerstellung in Blender®. Das Spulenmodell für die Simulation des elektrischen Feldes in SimNIBS® wurde in Kooperation mit Prof. Axel Thielscher von SimNIBS® erstellt, die Simulationen selbst wurden durch mich durchgeführt.

Die Konzeption der Erweiterung der Studie durch einen klinischen Fall erfolgte in Zusammenarbeit von Herrn Prof. Dr. Ulf Ziemann, Herrn Dr. Pedro Caldana Gordon und mir. Die MRT-Aufnahmen des klinischen Falls erstellte Herr Dr. Pedro Caldana Gordon. Die DTI-Traktographie-Analyse und Analyse der MRT-Daten des klinischen Falls wurde durch Herrn Olivier Roy durchgeführt. Die restliche Datenerhebung und Auswertung der klinischen Daten und EEG-Daten und die Untersuchung des Patienten erfolgten durch mich. Die Überweisung des Patienten erfolgte durch Herrn Prof. Dr. Volker Hömberg und Herrn Priv.-Doz. Dr. Oliver Kaut.

Bezüglich aller der aus Teilen der Dissertationsschrift erfolgten Publikationen (s. 8) habe ich die ungeteilte Erstautorenschaft inne.

Ich versichere, das Manuskript selbständig verfasst zu haben und keine weiteren als die von mir angegebenen Quellen verwendet zu haben.

Tübingen, den

____

Lukas Gaßmann

8 Publications

Parts of the dissertation have been published in the following research articles:

8.1 Original research article

Assessing effective connectivity of the cerebellum with cerebral cortex using TMS-EEG

Lukas Gassmann, Pedro Caldana Gordon, Ulf Ziemann

Brain Stimulation, Volume 15, Issue 6, 2022, Pages 1354-1369, ISSN 1935-861X, DOI: https://doi.org/10.1016/j.brs.2022.09.013.

8.2 Letter-to-the-editor

Cerebellar TMS-EEG in a chronic stroke patient with connectional diaschisis of the dentato-thalamo-cortical tract

Lukas Gassmann, Pedro Caldana Gordon, Olivier Roy, Oliver Kaut, Volker Hömberg, Ulf Ziemann

Clinical Neurophysiology, Volume 152, 2023, Pages 68-70, ISSN 1388-2457, DOI: https://doi.org/10.1016/j.clinph.2023.05.009.

8.3 Commentary

Reflecting the causes of variability of EEG responses elicited by cerebellar TMS

Lukas Gassmann, Pedro Caldana Gordon, Ulf Ziemann

NeuroImage, Volume 281, 2023, 120368, ISSN 1053-8119, DOI: https://doi.org/10.1016/j.neuroimage.2023.120368.

8.4 Poster abstracts

P 58 EEG responses from direct cerebellar activation with Transcranial Magnetic Stimulation

Lukas Gaßmann, Pedro Caldana Gordon, Ulf Ziemann

Clinical Neurophysiology, Volume 137, 2022, Page e48, ISSN 1388-2457, DOI: https://doi.org/10.1016/j.clinph.2022.01.089

P 2.010 Cerebrocortical signatures of cerebellar transcranial magnetic stimulation

Lukas Gaßmann, Pedro Caldana Gordon, Ulf Ziemann

Brain Stimulation, Volume 14, 2021, Page 1631, ISSN 1935-861X, DOI: https://doi.org/10.1016/j.brs.2021.10.139

9 Danksagung

Meiner ganzen Familie für ihren Rückhalt.

Besonderer Dank gebührt:

Horst Walter Meier

Eva Maria Meier

Beate, Michael & Helena Gaßmann

Barbara, Karl-Heinz, Robin & Jasmin Geiger

Meinen Mentoren für ihre Geduld und Unterstützung.

Besonderer Dank gebührt:

Prof. Dr. Ulf Ziemann

Prof. Dr. Thomas Dresbach

Außerdem:

Alina Schmidt

Meiner Heimat Deutschland, die mir mit ihren Institutionen, Universitäten und Stiftungen ermöglicht, Arzt zu werden.